T2R2 東京科学大学 リサーチリポジトリ
Science Tokyo Research Repository

論文 / 著書情報
Article / Book Information

題目(和文)	磁気流体力学シミュレーションを用いた原始惑星系円盤の乱流・熱構造の理解
Title(English)	Understanding the turbulent and thermal structure of protoplanetary disks with magnetohydrodynamic simulations
著者(和文)	森昇志
Author(English)	Shoji Mori
出典(和文)	学位:博士(理学), 学位授与機関:東京工業大学, 報告番号:甲第11059号, 授与年月日:2019年3月26日, 学位の種別:課程博士, 審査員:奥住 聡,井田 茂,綱川 秀夫,中本 泰史,野村 英子,廣瀬 重信
Citation(English)	Degree:Doctor (Science), Conferring organization: Tokyo Institute of Technology, Report number:甲第11059号, Conferred date:2019/3/26, Degree Type:Course doctor, Examiner:,,,,,
学位種別(和文)	博士論文
Type(English)	Doctoral Thesis

Powered by T2R2 (Science Tokyo Research Repository)

Doctoral Thesis

Understanding the turbulent and thermal structure of protoplanetary disks with magnetohydrodynamic simulations

Shoji Mori

Okuzumi Laboratory
Department of Earth and Planetary Sciences
Tokyo Institute of Technology

February 22, 2019

Abstract

Studies on protoplanetary disks are essential for understanding the formation process of planets. The disk structure is largely affected by magnetic fields. Therefore, clarifying the influence of the magnetic field on the disk structure allows us to construct the planet formation theory in realistic protoplanetary disks. Especially, turbulence strength is an important parameter because it causes the disk accretion and heats the disk gas. The thermal structure is essential for understanding the planet formation process and verifying the formation theory by comparing with observations. In this thesis, we have investigated the role of magnetohydrodynamics on the turbulent and thermal structures of protoplanetary disks with numerical magnetohydrodynamic (MHD) simulations.

This thesis consists of four chapters. In Chapter 1, we introduce the general introduction for the previous studies on planet formation and protoplanetary disks. Furthermore, we focus on the effect of magnetic fields on the structures of protoplanetary disks. The disk turbulence is thought to be generated by a magnetorotational instability (MRI). The MRI turbulence largely depends on the ionization fraction which determines the strength of nonideal magnetohydrodynamic (MHD) effects. Because the protoplanetary disks are the low-ionized environment, the understanding of the ionization state and the resulting nonideal MHD effects is important. Therefore, understanding the ionization fraction is necessary to properly understand turbulent strength and for further discussion for the thermal structure. The purpose of this thesis is to understand MRI strength by focusing on the ionization state and to elucidate thermal structure in the magnetized disks.

In Chapter 2, we have investigated the turbulence strength taking into account electron heating by MRI-induced electric fields. The heating decreases the ionization fraction of the gas because the electrons heated by the electric fields quickly stick to dust grains. This effect on the evolution of magnetorotational instability has been neglected. The electron heating is expected to decrease the ionization fraction and enhance the non-ideal MHD effects. We perform three-dimensional MHD simulations including change of the ionization fraction by the electron heating, and investigate the turbulence strength. We confirm that the electron heating suppresses the MRI turbulence. Also, we have found a clear correlation between the magnetic stress and its current density. We propose a formula that successfully predicts the magnetic stress suppressed by the effect of electron heating.

In Chapter 3, we have focused on the thermal structure of protoplanetary disks in the laminar disks. The suppression of magnetic turbulence makes a significant difference from the conventional turbulence-driven accretion disks. When the turbulence is sufficiently weak, the magnetic fields threading the disk remove the angular momentum and energy as magnetohydrodynamic wind, and thereby drives the disk accretion. The energetics of this wind-driven accretion disks can be largely different from the conventional model, but this has not been investigated well. In this Chapter, considering these recent works, we investigate the temperature structure in the wind-driven accretion disk with nonideal MHD simulations. Our simulations have confirmed that the suppression of turbulence around midplane leads to release the heat at disk surface, which is efficiently removed by radiative cooling. As a result, the disk is much colder than the conventional model. Also, removal of accretion energy by disk wind reduce the total energy which used for heating. Therefore, we have concluded that the accretion heating is much inefficient than the conventional model.

In Chapter 4, we summarize the renewed structure of the protoplanetary disks. We also discuss the evolution of the snow line and review the Earth formation process which explains Earth's low-water content on the basis of knowledge of our MHD simulation. The inefficient accretion heating suggests the necessity for the Earth to complete its formation in the early phase of the disk evolution ($\lesssim 0.4$ Myr). To understand rocky planet formation consistent with the water content requires other heating mechanisms (e.g., hydrodynamic turbulence) and/or formation mechanism that Jupiter can form earlier

Contents

1 General Introduction **1**

1.1 Observations 1

1.2 Overview of Planet Formation and Protoplanetary Disks 4

1.2.1 Classical Model of Protoplanetary Disk Structures 4

1.2.2 Evolution and Structure of Protoplanetary Disks 5

1.2.3 Disk Evolution 5

Structure of Surface Density 7

Structure of Temperature 8

1.2.4 Planet Formation 10

Classical Scenario 10

Remaining Problems: Rocky Planet Formation 11

1.3 Role of MHD in Protoplanetary Disks 13

1.3.1 Fundamentals of MHD 13

1.3.2 Magnetorotational Instability 16

Ideal MHD 16

Non-Ideal MHD 17

Plasma Heating by MRI-Induced Electric Fields 19

1.3.3 MHD Disk Wind 22

1.4 Purpose of This Research 23

1.5 Guide of This Thesis 24

2 Effects of Electron Heating on the Magnetorotational Instability 25

2.1 Introduction 26

2.2 Method 29

2.2.1 Numerical Method 29

2.2.2 Simulation Settings 32

2.2.3 Initial Conditions 35

2.3 Simulation Results 37

2.3.1 The Fiducial Case 37

2.4 Derivation of Current–Stress Relation 47

2.5 Summary and Discussion 50

3 Temperature Profile of the Inner Regions of Protoplanetary Disks 55

3.1 Introduction 56

3.2 Methods and Model 59

3.2.1 Numerical Method 59

3.2.2 Simulation Setup 62

3.2.3 Simulation Parameters 64

3.2.4 Energy Equations 64

Dissipation Profiles 65

Temperature Profiles 66

3.3 Fiducial Run 69

3.3.1 Gas Dynamics and Dissipation 69

The Case of $B_z > 0$ 70

The Case of $B_z < 0$ 72

3.3.2 Temperature Profiles 73

No irradiation 73

With irradiation 75
3.4 Parameter Exploration 77
3.4.1 Dependence on Radial Distance 83
3.5 Discussion 84
3.5.1 Geometry of Magnetic Field 84
3.5.2 Dependence on the Prior Temperature 85
3.5.3 Impacts of Inefficient Accretion Heating on Planet Formation . . 86
3.5.4 On Plasma Heating by Strong Electric Fields 88
3.5.5 Difference from Previous Study 88
3.6 Summary and Conclusion 89
3.7 Appendix A: Temperature Structure of
Reflection-Asymmetric Dissipation Profile in Disks 90
3.8 Appendix B: Conservation of Mechanical Energy in the Simulations . . . 98

4 Discussion and Summary **101**
4.1 Expected Structures of Protoplanetary Disks 101
4.1.1 Expected Turbulent Structure 101
Electron Heating with Non-Ideal MHD Effects 102
4.1.2 Expected Thermal Structure 104
Modeling of Thermal Structure 104
Disk Structure around Thermally-Ionized Region 107
Shadow due to Innermost Region 108
4.2 Time Evolution of Background Magnetic Fields 109
4.3 Implication for Planetesimal Formation in Electron-Heating Zones 110
4.4 Implication for Snowline Problem 111
4.4.1 Introduction 112
4.4.2 Evolution of Snowline 113

4.4.3 Other Effects on Snowline 116
Hydrodynamic Turbulence 116
FU Ori Bursts 118
Gravitational Instability 119
Summary 119
4.4.4 Constraints for Earth Formation 120
In Situ Formation 120
Outward migration 123
4.5 Summary and Conclusion 124

Chapter 1

General Introduction

In this chapter, we introduce the conventional picture of planet formation theory and protoplanetary disks. We review studies on magnetorotational instability in protoplanetary disks.

1.1 Observations

How the Earth formed is a big old question for a long time. Since the Earth formation occurred only once in the past, we cannot directly experiment or observe this event. However, we can explore the most plausible Earth formation process by theoretically constructing planet formation scenarios which explain the current observational features on the solar system. Revealing the Earth formation provides us with the initial condition for the evolution of the surface environment, interior, and life of the Earth.

To see the other planets outside the solar system gives us a hint to comprehensively understand the planet formation process. So far, many exoplanet explorations have been conducted since Mayor & Queloz have discovered the first exoplanet around a main sequence star. At February 22, 2019, 3848 exoplanets including candidates have been found (https://exoplanetarchive.ipac.caltech.edu/). Figure 1.1 shows exoplanets of

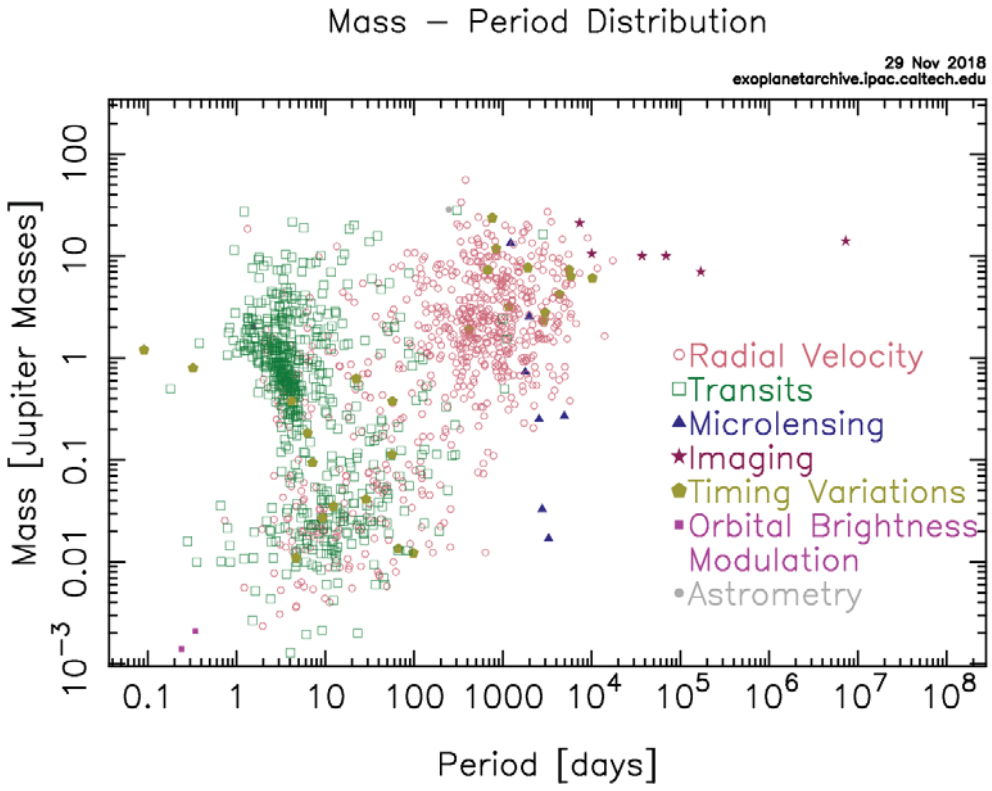

Figure 1.1 Mass – period distribution of confirmed exoplanets at 29th November 2018, cited from https://exoplanetarchive.ipac.caltech.edu/. The mass and the period are normalized by the Jupiter and a day, respectively. Symbols show the observational methods. Credit: Courtesy NASA / JPL-Caltech.

which existence are confirmed until now in the mass–period diagram. The finding exoplanets tell us the presence of the diversity in exoplanets. For example, the exoplanet which is first discovered is a Jupiter-like planet (mass $\gtrsim 0.1$ Jupiter mass). However, the planet is very close to the central star and is expected to be significant hot due to the irradiation from the star. Such planets are classified as "hot Jupiters". Also, hot Neptunes are Neptune-like planets (mass $\lesssim 0.1$ Jupiter mass) but orbiting close to the central star. Super-Earths are planets which consist mainly of rock but has too larger mass than the Earth. The discovery of the diversity brings us into another question, how is the diversity made? To answer these questions, the general planet formation theory which explains the formation process for all exoplanets (including the Earth) is required.

For revealing the planet formation, it is necessary to understand the environment where planets form. Planets form in protoplanetary disks which is a rotating disk around a newly formed star. The disk contains gas and dust, and the dust grains grow into a planet. To know the structures of protoplanetary disks is a key to reveal planet formation.

So far, many disk observations have been carried out to study the disk properties and find evidence of the forming planets since the 1980s, with spectral energy distribution (e.g., Elsasser & Staude, 1978; Haisch et al., 2001; Luhman et al., 2010) and direct imaging (e.g., Fukagawa et al., 2006; Andrews et al., 2011; Muto et al., 2012; van der Marel et al., 2013; Grady et al., 2013). Recently, the Atacama Large Millimeter Array (ALMA) is observing many PPDs with its significant angular resolution (e.g., ALMA Partnership et al., 2015; Isella et al., 2016). Interestingly, ALMA has shown us various well-resolved features which may be created by planets: gap (e.g., ALMA Partnership et al., 2015; Isella et al., 2016), spiral arms (Pérez et al., 2016), and vortexes (van der Marel et al., 2013; Kraus et al., 2017). Planets gravitationally interacting PPDs wake density waves, which are like spiral arms (e.g., Ogilvie & Lubow, 2002). Planets scattering surrounding gas cave a gap in PPDs (e.g., Lin & Papaloizou, 1986). These findings highlight that the protoplanetary disks are more complex and require more sophisticated disk model which can be compared to the observations.

Although the disk observations have been revealed many figures of protoplanetary disks and are getting improved, there are still many restrictions. One is a time restriction. Since the disk lifetime is extremely longer than a human timescale, the disk observations show just snapshots of a protoplanetary disk, do not tell a continuous story of the protoplanetary disk. Also, the observed evolutionary phase is biased toward the main evolutionary stage. For the spatial resolution, though it is getting improved, sub-AU scales have not been resolved yet. Furthermore, because the disk interior is typically high density, light from the region is absorbed in the region again, and does not reach us.

To understand the physical properties of the protoplanetary disks the theoretical works predicting the disk structure construct a picture of protoplanetary disks and fills in gaps between disk observations and finding planets. In the subsequent section, we briefly overview the protoplanetary disks and conventional planet formation theories.

1.2 Overview of Planet Formation and Protoplanetary Disks

1.2.1 Classical Model of Protoplanetary Disk Structures

The most widely-used disk model is a minimum mass solar nebula (Hayashi, 1981). The concept of this model is that the dust surface density is given so that it reproduces the mass distribution of the planets in the Solar system. He noted that in the hot inner region of the primordial solar nebula the water exists as a vapor, while in the outer cold region, water exists as solid. The water in solid increases the dust surface density. The dust surface density $\Sigma_{\rm d}$ at a distance r from the star is given by

$$\Sigma_{\rm d} = 7.1\eta_{\rm ice}\left(\frac{r}{1\,{\rm AU}}\right)^{-3/2}\ {\rm g\ cm^{-2}}\,, \tag{1.1}$$

where $\eta_{\rm ice}$ express the increases of dust mass by the ice and was assumed to be 4.2. Assuming the disk to be the solar composition (they used a silicate-to-gas ratio of 0.0043), they gave the gas surface density Σ from the dust surface density,

$$\Sigma_{\rm g} = 1700\left(\frac{r}{1\,{\rm AU}}\right)^{-3/2}\ {\rm g\ cm^{-2}}\,. \tag{1.2}$$

Although the detailed dust compositions was updated after the paper, the gas surface density profile is commonly used as a fiducial disk model.

Where water exists as a solid is determined by the temperature profile. The temperature distribution determines the phase of water (gas or solid). The boundary between the two regions is called a water snow line. In their model, the temperature is given by assuming the optically thin disk. The temperature profile is given by the energy balance between the energy flux from stellar radiation and the cooling by black body radiation. The temperature profile is (Hayashi, 1981),

$$T = 280\left(\frac{r}{1\,\mathrm{AU}}\right)^{-1/2}\left(\frac{L}{L_\odot}\right)\,\mathrm{K}\,, \tag{1.3}$$

where L and $L_\odot$ are the luminosity of the central star and the Sun, respectively. The phase chase of water occurs at around 170 K in typical protoplanetary disks. In this temperature profile, the snow line is located at 2.7 AU. The rocky planets in the solar system exist interior to 2.7 AU.

The minimum solar nebula model is based on the current Solar system. However, since so far many exoplanetary systems to be very different from the solar system have been found, this model would not be valid for other systems. Also, this model does not take into account how such a disk forms. In the next subsection, we see the formation and evolution of protoplanetary disks from star formation.

1.2.2 Evolution and Structure of Protoplanetary Disks

1.2.3 Disk Evolution

Protoplanetary disks are remnants of star formation. First, a high-density region (molecular cloud core) in a molecular cloud (mainly H_2) gravitationally collapses, which is the start of the star formation. The collapse starts from inside to outside of the cloud core and then first forms a protostar (Shu, 1977). The gas having an angular momentum collapses

into a radius on a rotating plane, forming a protoplanetary disk. Though most of the mass of the molecular cloud falls into the protostar, only 1% of cloud mass remains the disk. The gravitational collapse phase continues over ~ 0.1 Myr.

During gas falling into the disk, the disk gas accretes to the star. The disk accretion continues to ~ 3 Myr[1] after the collapse (e.g., Haisch et al., 2001).

This accretion process determines the disk structure. Gas falling to the disks eventually accretes to the star by removal or transport of the angular momentum. The most standard accretion model is a viscous-driven accretion disk (Shakura & Sunyaev, 1973). In the model, a viscosity transfers the disk angular momentum to gas in the outer region. As a result, most of disk gas loses the angular momentum and thereby accrete to the star. If we express the viscosity (the unit is length $\times$ velocity) as a parameter normalized by typical disk parameter, we can express the viscosity ν as

$$\nu = \alpha c_s H \,, \tag{1.4}$$

where c_s is the sound speed, H is the scale height of the gas pressure, and α is a dimensionless parameter expressing the strength of the viscosity. In this reason, this model is called the α model. This expression allows us to take into account the angular momentum transport without specifying detail physics of the transport mechanism.

[1]This disk lifetime is estimated from the observation investigating the disk frequencies in various star clusters. If we assume the star formation started simultaneously in a star cluster, the observation provides the relation between disk frequency and time after the collapse. Fitting the observation data, we obtain the depletion timescale of the protoplanetary disks.

Structure of Surface Density

If we assume steady disk evolution, we obtain a relation between the viscosity and the resulting mass accretion rate $\dot{M}$ (Lynden-Bell & Pringle, 1974),

$$\dot{M} = 3\pi\Sigma\nu\,, \tag{1.5}$$

where Σ is the gas surface density[2]. Using this equation, the gas surface density is related to the α parameter,

$$\begin{aligned}\Sigma &= \frac{\dot{M}}{3\pi\alpha c_s H} \\ &= 134\left(\frac{\dot{M}}{10^{-8}\mathrm{M}_\odot/\mathrm{yr}}\right)\left(\frac{\alpha}{0.01}\right)^{-1}\left(\frac{T}{280\,\mathrm{K}}\right)^{-1}\left(\frac{M_*}{M_\odot}\right)^{1/2}\left(\frac{r}{1\,\mathrm{AU}}\right)^{-3/2}\ \mathrm{g\ cm^{-2}}\,.\end{aligned} \tag{1.6}$$

The mass accretion rate at a radius is determined by that of the outer disk region, and thereby is a given parameter. Thus, when a mass accretion rate is given, the surface density is large when α is small. This is due to the stagnation of gas accretion. The surface density is important because it is the basic quantities determining the mass scale at a location of the disk.

Although the α value is important parameter that controls the surface density, the realistic range of α is still unknown. So far, many studies tackled this question. The α value is determined by Reynolds and Maxwell stress. According to previous studies with (magneto-)hydrodynamics simulations, the typical range seems to be 10^{-4}–10^{-2}. This huge uncertainty also gives an uncertainty in the disk structures and planet formation theory.

[2]The gas surface density is the integrated value of the gas density to the direction perpendicular to the disk plane (we usually call it as a vertical direction).

Structure of Temperature

The temperature structure also changes in the evolutionary stage. Even though in the optically thin limit the temperature is given by Equation (1.3), in the optically thick disk the temperature profile is different. When the disk is optically thick, the disk receives the stellar irradiation on the disk surface. The incident flux is reduced by the grazing angle of incoming irradiation, and therefore the resulting disk temperature is smaller than in the optically thin limit (Chiang & Goldreich, 1997),

$$\begin{aligned} T_{\rm irr} &= 156.82 \left(f_L f_{\rm in}^{-1} f_{\rm p} f_{\rm angle}\right)^{2/7} \left(\frac{r}{1\,{\rm AU}}\right)^{-3/7} \left(\frac{L_*}{L_\odot}\right)^{2/7} \left(\frac{M_*}{M_\odot}\right)^{-1/7} \ {\rm K} \\ &= 110 \left(\frac{r}{1\,{\rm AU}}\right)^{-3/7} \left(\frac{L_*}{L_\odot}\right)^{2/7} \left(\frac{M_*}{M_\odot}\right)^{-1/7} \ {\rm K}\,. \end{aligned} \tag{1.7}$$

where and M_* and L_* is the stellar mass and luminosity, respectively. For calculating, we here use the following assumption. The ratio f_L of the incoming flux to $L_*/4\pi r^2$ is 0.5 because the half area of the star is hidden by the innermost region. The half of energy is transferred to the disk interior, $f_{\rm in} = 0.5$. The ratio $f_{\rm p}$ of the photosphere scale height to H is 4. The ratio $f_{\rm angle}$ of the grazing angle to the aspect ratio H/r is 2/7 calculated by using $r^{-3/7}$.

Furthermore, in an accretion disk, the release of the gravitational energy can be an additional heat source. Given a mass accretion rate $\dot{M}$, the energy is approximately given by

$$\dot{E}_{\rm acc} = \frac{3GM\dot{M}}{4\pi r}\,. \tag{1.8}$$

The heated gas is cooled by the black body radiation from the upper and lower disk surface. The cooling rate of the surface temperature $T_{\rm surf}$ is $2\sigma_{\rm SB}T_{\rm surf}^4$, where $\sigma_{\rm SB}$ is the Stefan-Boltzman constant. The temperature at the disk surface is given by, (Shakura &

Sunyaev, 1973),

$$T_{\rm surf} = \left(\frac{3GM\dot{M}}{8\pi\sigma_{\rm SB}r^3}\right)^{1/4} = 85\left(\frac{\dot{M}}{10^{-8}{\rm M}_\odot/{\rm yr}}\right)^{1/4}\left(\frac{M_*}{M_\odot}\right)\left(\frac{r}{1\ {\rm AU}}\right)^{-3/4}\ {\rm K}\,. \tag{1.9}$$

One might consider that the accretion heating is unimportant for the disk temperature since the temperature given in Equation (1.9) smaller than that by irradiation. However, when the accretion energy releases in the disk interior, the heat accumulates the disk because the radiation cooling is slow in the optically thick region.

Here we consider the uniform turbulence leading to constant α value. If we assume that the turbulence drives the disk accretion and the energy dissipation occurs simultaneously and locally, the heating rate is proportional to the gas density (Shakura & Sunyaev, 1973). Therefore, the accretion heating by the turbulent viscosity, which is called viscous heating, significantly increases the disk temperature, in particular when the accretion rate is high. The temperature profile is given by

$$T_{\rm vis} = 326\left(\frac{\dot{M}}{10^{-8}{\rm M}_\odot/{\rm yr}}\right)^{2/5}\left(\frac{M}{M_\odot}\right)^{3/10}\left(\frac{\kappa}{5\ {\rm g\ cm^{-2}}}\right)^{1/5}\left(\frac{\alpha}{10^{-2}}\right)^{-1/5}\left(\frac{r}{1\ {\rm AU}}\right)^{-9/10}\ {\rm K}\,, \tag{1.10}$$

where κ is the Rosseland mean opacity.

How much propagating of heat is delayed is determined by the opacity, which measures the absorbing cross-section per unit mass. In protoplanetary disks, the main opacity source is dust. Light randomly propagates through the medium, as it is absorbed by and reemitted from the grains repeatedly. Even though the opacity is an essential parameter for the heat accumulation, the opacity largely varies due to the dust growth. Thus, the opacity has large uncertainty.

1.2.4 Planet Formation

Classical Scenario

During disk evolution, planet formation proceeds. The first step of planet formation is growing phase of dust grains into planetesimals (size $\sim$ 1 km), which are hypothetical objects in planet formation. The planetesimals is thought to aggregate into planets. There are two plausible ways for the planetesimal formation: coagulation by sticking and gravitational collapse of dust. For the coagulation model, the dust grains repeatedly collide with and stick to each other in protoplanetary disks. By this process, the micron-sized dust particles grow up into planetesimals.

The next step is the growth of planetesimals into protoplanets. The planetesimals gravitationally interact with each other. The planetesimals grow in a runaway fashion as the gravitational focusing increases with the growth, and thereby become a protoplanet (mass $\sim 0.1\ M_\oplus$). The protoplanet excites the eccentricities of surrounding planetesimals, which weakens the gravitational focusing between the protoplanets and planetesimals, and the runway growth stops (Kokubo & Ida, 1996, 1998; Kokubo et al., 2000). After the disk disperses owing to accretion into the central star, a system of the protoplanets becomes dynamically unstable. Their orbital crossing causes giant impacts, and finally Earth-sized planets form. For planet formation for gas planets (e.g., Jupiter and Saturn), when the protoplanet mass exceeds a critical mass before disk dissipation, the protoplanet absorbs the disk gas and thereby become gas planets.

This scenario seems to explain the formation of the solar system. However, the classic scenario has many difficulties. One of the difficulties is the "meter size barrier". When the size of dust grains is small ($\lesssim$1 mm), their motion couples with gas motion well. After the grains grow into meter-sized particles (pebbles[3]), they decouple from gas and

[3]Such particles decoupling from gas is often called pebbles, even though the size can be over a meter.

feel a headwind ($\sim$ 50 m/s). The headwind removes the pebbles' angular momentum, and hence the pebbles radially drift. The drift timescale is of the order of 10^2 years (Adachi et al., 1976; Weidenschilling, 1977). Thus, the most solid particles fall into the central star before they grow up into planetesimals. Moreover, the radial drift increases the relative velocity. This causes the fragmentation and bouncing of the grains, which are experimented with laboratory experiments (Blum & Wurm, 2000; Güttler et al., 2010; Zsom et al., 2010, see a review of Blum & Wurm (2008)) and numerical simulations (Dominik & Tielens, 1997; Wada et al., 2007, 2008, 2009, 2011, 2013).

The planet formation by gravitational collapse is recognized as a way to circumvent the meter size barrier (Safronov, 1969; Goldreich & Ward, 1973; Johansen et al., 2009). If the disk turbulence absent, the dust particles settle on the midplane and form a dust layer. When the dust density exceeds a threshold, the self-gravitational instability of the dust layer occurs, and eventually planetesimals forms. However, when there is turbulence in the disk, dust is stirred up and hindered to form the dust layer (Weidenschilling & Cuzzi, 1993). Thus, from the dust coagulation model, in order to build a successful planet formation model, the strength of the disk turbulence should be investigated.

Remaining Problems: Rocky Planet Formation

We here stress the problems of rocky planet formation in the classic planet formation theory. Rocky planets are planets consisting mainly of silicate, which include Mercury, Venus, Earth, and Mars in the Solar system. Also, Earth-like exoplanets have been discovered (e.g. Dressing et al., 2015; Gillon et al., 2017), and they are estimated to be composed of rock from the bulk density (e.g., Grimm et al., 2018; Dorn et al., 2018). Although rocky planets exist universally in planetary systems, its formation process is still uncertain.

This is just a definition.

Given the solar system composition (Lodders, 2003), the dust of the protoplanetary disks consists mainly of ice and rock. The rocky planets are probably formed from the coagulation of rocky dust inside the water snow line. The sticking efficiency depends on the chemical composition of the grain surface (Johnson et al., 1971; Johnson, 1987; Chokshi et al., 1993). Icy aggregates can grow by coagulation when the relative velocity is less than 50 m/s (Dominik & Tielens, 1997; Wada et al., 2009). However, the rocky aggregates cannot grow with the relative velocity larger than 5 m/s (Chokshi et al., 1993; Dominik & Tielens, 1997; Wada et al., 2007, 2008, 2009). Because the typical maximum-relative-velocity of meter-sized particles is also around 50 m/s even in the laminar disk (Adachi et al., 1976; Weidenschilling, 1977; Nakagawa et al., 1986), the collision of rocky particles leads to fragment. This is fragmentation barrier which is a severe problem.

Furthermore, the region where water exists as vapor depends on disk evolution, when the temperature is determined by the accretion heating. The time and space where the rocky planetesimal formation is possible are limited. For example, the Earth is characterized by its low water content. The current mass of the Earth's ocean is only 0.022 wt% of the Earth mass (e.g., Charette & Smith, 2010). Even if we consider the water in the core, the water content is about 1.6 wt% at most (Nomura et al., 2014).

In the early phase of the disk evolution, the accretion rate decreases and thereby the temperature also decreases with time (Davis, 2005; Garaud & Lin, 2007; Oka et al., 2011). After the accretion heating becomes less efficient than the irradiation heating, the irradiation heating determines the position of snow line, which is around 0.5 AU for sun-like star (Equation (1.7)) This process means that the snow line passes the current earth's orbit (r = 1 AU) sooner or later at some stage of the disk evolution. If icy dust (the water content of $\sim$ 50%) would accrete onto the proto-Earth, then the Earth would have obtained much more abundant water then the current ocean mass (Sato et al., 2016). Once a large amount of water is supplied to the Earth, evaporating the water from the Earth is difficult (Genda

& Abe, 2005; Machida & Abe, 2010). Therefore, it is surprising that the Earth's water content is suppressed into an exquisite amount of water that makes the ocean and at the same time allows the presence of land.

1.3 Role of MHD in Protoplanetary Disks

Although there are many studies on planet formation, it is still a mystery. This suggests that the disk model should be more sophisticated. One of the most important effects is the effects of magnetic fields on the disk structures. The dynamics of magnetic fluid (magnetohydrodynamics, MHD) is essential for understanding the structures of the protoplanetary disks. The magnetic field can cause turbulence and also controls the disk evolution. Here, we mention of the role of the magnetic field in protoplanetary disks.

1.3.1 Fundamentals of MHD

Here, we describe the fundamentals of MHD. MHD deals with gas motion in magnetic fields by taking account of force from magnetic fluids. In magnetic fields, the neutral particles are exerted by collisional force from ionized particles. Since motion of the ionized particles is governed by the Lorentz force, we can say that the neutral fluid receives force from the magnetic field. Conversely, the motion of neutral gas also affects the magnetic field by the electric field by current of ionized particles.

MHD is based on assumption that the electric neutrality holds in a fluid parcel. In addition, MHD approximation assumes that displacement current is neglected. Hereafter, we use these assumptions.

The Lorentz force exerting a fluid in MHD is

$$\frac{1}{c}\boldsymbol{J}\times\boldsymbol{B} = \frac{1}{4\pi}\left((\nabla\times\boldsymbol{B})\times\boldsymbol{B}\right), \tag{1.11}$$

$$= \frac{1}{4\pi}\left(\boldsymbol{B}\cdot\nabla\right)\boldsymbol{B} - \nabla\left(\frac{B^2}{8\pi}\right), \tag{1.12}$$

where we have used the neutrality of fluid for the derivation. The first term express a tension force by magnetic fields (magnetic tension) and the second is a magnetic-pressure-gradient force. The importance of the magnetic force [4] to the pressure represents a ratio of gas pressure to magnetic pressure (called plasma beta β),

$$\beta = \frac{8\pi P}{B^2}\,. \tag{1.13}$$

Another important quantity is the propagation speed on the magnetic forces. The speed is known as Alfvén velocity,

$$v_A = \frac{B_0}{\sqrt{4\pi\rho}}\,. \tag{1.14}$$

The evolution of a magnetic field is solved by the Maxwell-Faraday equation,

$$\frac{\partial\boldsymbol{B}}{\partial t} = -c\nabla\times\boldsymbol{E}\,, \tag{1.15}$$

with the other Maxwell equations,

$$\boldsymbol{\nabla}\cdot\boldsymbol{E} = 0, \tag{1.16}$$

$$\boldsymbol{\nabla}\cdot\boldsymbol{B} = 0, \tag{1.17}$$

$$4\pi\boldsymbol{J} = c\nabla\times\boldsymbol{B}. \tag{1.18}$$

where we have dropped the displacement current in Equation (1.18) by assuming non-

[4] Strictly speaking, the value expresses the unimportance of the magnetic force to the gas pressure.

relativistic fluid. The relation between an electric field and current density, which is called "the Ohm's law", in a comoving frame (which moves with fluid) is written as

$$\boldsymbol{J}' = \sigma_{\rm c}\boldsymbol{E}' \tag{1.19}$$

where we express an electric conductivity as $\sigma_{\rm c}$ and values in the comoving frame with the superscript " $'$ ". Under the Lorentz transformation in $u \ll c$, $\boldsymbol{E}'$ and $\boldsymbol{J}'$ are related with $\boldsymbol{E}$ and $\boldsymbol{J}$ as

$$\boldsymbol{E}' = \boldsymbol{E} + \frac{1}{c}\boldsymbol{u} \times \boldsymbol{B}\ , \tag{1.20}$$

$$\boldsymbol{J}' = \boldsymbol{J}\ , \tag{1.21}$$

where we have dropped the second order of u/c. Using Equations (1.15), (1.19), (1.20), and (1.21), we obtain the induction equation,

$$\frac{\partial \boldsymbol{B}}{\partial t} = -c\nabla \times \left(\frac{\boldsymbol{J}}{\sigma_{\rm c}} - \frac{1}{c}\boldsymbol{u} \times \boldsymbol{B} \right). \tag{1.22}$$

When we consider a limit of infinite electric conductivity, $\sigma_{\rm c} \to \infty$, the term of $J/\sigma_{\rm c}$ can be neglected. The assumption is called as ideal MHD approximation, or the case where the assumption is valid is called ideal MHD. In ideal MHD, the induction equation is

$$\frac{\partial \boldsymbol{B}}{\partial t} = \nabla \times (\boldsymbol{u} \times \boldsymbol{B}). \tag{1.23}$$

1.3.2 Magnetorotational Instability

Ideal MHD

Magnetorotational instability (MRI) is an instability which takes place in differentially rotating disks with sufficient sufficient ionization fraction. The MRI is thought to be the most plausible mechanism of generating turbulence. The turbulent viscosity is important because it drives mass accretion in protoplanetary disks. The MRI is first discovered in the context of general accretion disks by Velikhov (1959), and is rediscovered in the context of protoplanetary disks by Balbus & Hawley (1991).

The magnetic fields lead to Maxwell stress, an accretion stress which is caused by the magnetic tension. Maxwell stress of vigorous MRI turbulence provides an effective disk viscosity that allows the disk lifetime consistent with disk observations (Hawley et al., 1995; Fromang & Nelson, 2006; Simon et al., 2009; Flock et al., 2011). In the fully developed MRI turbulence, the kinetic energy of the turbulence is also enough high to prevent dust settling (Carballido et al., 2005) and disrupt particles by collisions (Carballido et al., 2010).

The early studies on MRI used ideal MHD, which is a limit of sufficiently ionized gas. In the limit, ionized gas couples with magnetic fields. The motion of the ionized gas is governed by magnetic tension force and magnetic pressure gradient.

The physics of MRI is explained by a system that two particles are connected by a weak spring in a horizontal plane (see Figure 16 in Balbus & Hawley (1998)). The particles describe gas particles and the spring describes the magnetic tension force. The tension force by the spring transport the angular momentum from the inner particle to the outer particle. The inner gas parcel move inwards due to lose of the angular momentum, while conversely the outer gas parcel moves outward. If the spring is sufficiently weak, the ra-

dial deviation of the parcels appears. Since the disk is differentially rotating, the inner gas relatively moves in the azimuth direction, and thereby the spring is stretched in the azimuthal direction. As the tension increases, the transport of angular momentum increases. This process amplifying magnetic fields is the physics of MRI.

Balbus & Hawley (1998) shows a simulation result of nonlinear MRI growth in the local simulation box in Figure 18. After perturbations of the vertical magnetic field is given at the beginning, angular momentum is transported via the vertical magnetic field, and thereby MRI grows. Furthermore, when the magnetic field is sufficiently stretched, the antiparallel magnetic field causes magnetic reconnections, which convert the magnetic energy into kinetic energy. After that, MRI starts to grow again and continually increases the kinetic and magnetic energy. In this way, MRI creates magnetic turbulence with complex magnetic fields.

One of the features of MRI is the point that MRI grows even in a weak magnetic field and amplify the magnetic field by itself In addition, the growth timescale is order of the Kepler time. This is significantly fast compared to the timescales of disk evolution. For these reasons, MRI have been studied as a mechanism generating turbulence of the disk.

Non-Ideal MHD

In the MRI in protoplanetary disks, that the protoplanetary disks is weakly ionized is important. Since most region of the protoplanetary disks is colder for thermal ionization, which ionize the neutral gas particles by the thermal motion of particles ($T \sim 800$K). Thermal ionization is relevant only close to the central star (Umebayashi, 1983). the dominant part of the disks is ionized only by high-energy sources such as galactic cosmic rays (Umebayashi & Nakano, 1981), stellar X-rays (Glassgold et al., 1997), and far

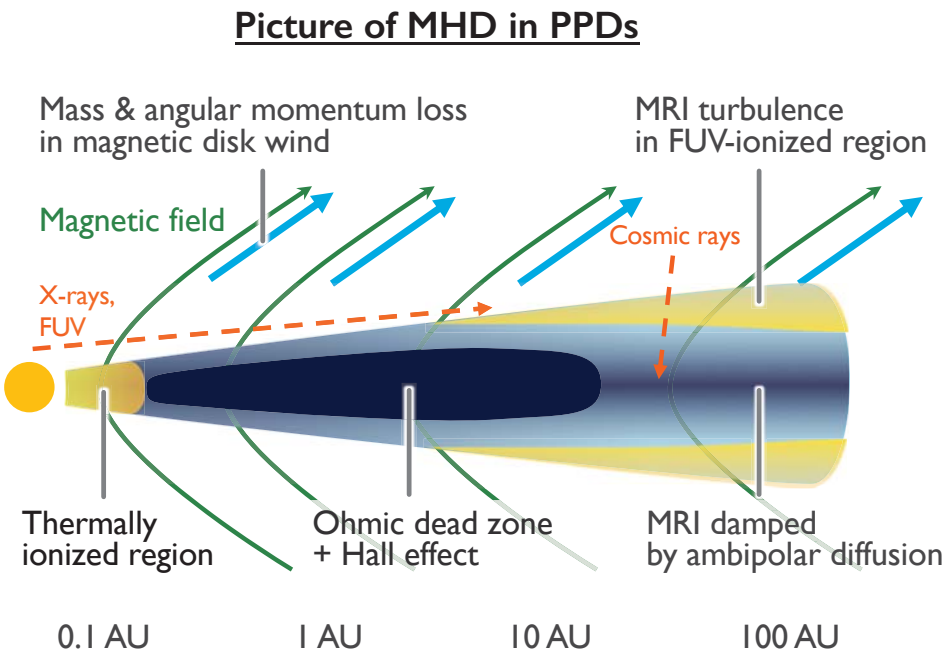

Figure 1.2 Schematic illustration of the predicted structure of poorly ionized protoplanetary disks threaded by weak magnetic fields. Basically, the interior of protoplanetary disks is not well ionized, except for the inner thermally ionized region and outer surface FUV ionized region. In the weakly ionized region, the nonideal MHD effects (Ohmic diffusion, Hall effect, and ambipolar diffusion) is important for the behavior of magnetic fields. The ohmic diffusion suppresses MRI typically at high-density regions, and the ambipolar diffusion at low-density region. In the intermediate-density region, the Hall effect amplify or decay magnetic fields. Magnetic fields threading the protoplanetary disks transport disk angular momentum to disk wind, which drives disk accretion and depletes gas surface density. This figure is based on Simon et al. (2015).

ultraviolet rays (Perez-Becker & Chiang, 2011). Deep inside the disks, the ionization fraction is significantly low because these ionizing radiations are attenuated and because recombination proceeds fast.

When gas is not sufficiently ionized, the neutral gas decouples from the magnetic field. The decoupling of the magnetic fluid cause non-ideal MHD effects: Ohmic diffusion, ambipolar diffusion, and Hall effect. The features of the nonideal MHD effects is as follows. The Ohmic diffusion is caused by the decoupling of magnetic fields from electrons and ions, which tend to occur in high-density regions due to high collisional frequency. The

ambipolar diffusion is due to decoupling of gas from ionized particles, which tend to occur in low-density regions due to less collisional frequency. The both diffuse magnetic fields. The Hall effect occurs when the electrons decouple from gas particle and the ions decouples from the magnetic fields, in the intermediate-density region. In the situation, if there is current, since the current moves electrons and ions in opposite direction, the current decouples the gas and magnetic fields. The Ohmic and ambipolar diffusion dissipates energy, which is called Joule dissipation or Joule heating. On the other hand, the Hall effect does not.

Figure 1.2 shows the structure of MHD effects in protoplanetary disks shown in (Simon et al., 2015). The low ionization fraction gives rise to fast Ohmic dissipation that stabilizes the MRI (Sano & Miyama, 1999). Such a region is called the "Ohmic dead zone" (Gammie, 1996; Sano et al., 2000). The MRI is also suppressed by ambipolar diffusion near the surface of the disks (Desch, 2004; Bai & Stone, 2011; Dzyurkevich et al., 2013). The Hall effect can either stabilize or destabilize the MRI depending on the orientation of the magnetic field relative to the disk rotation axis (Wardle, 1999; Wardle & Salmeron, 2012; Bai, 2014).

Plasma Heating by MRI-Induced Electric Fields

All the previous studies of MRI had neglected the ionization process caused by MRI itself until Inutsuka & Sano (2005) investigated the possibility of ionization by electric fields in MRI turbulence with a simple estimation. They found heating of electron by electric fields in MRI turbulence (upper panel of Figure 1.3), which is called the "electron heating". The heating mechanism is the following. The vigorous MRI turbulence generates strong electric fields associated with the growth of magnetic fields. Plasma particles are accelerated by the strong electric fields and are scattered isotropically by collisions with neutral gas particles, leading to the increase of their thermal velocity. In particular, electrons are more

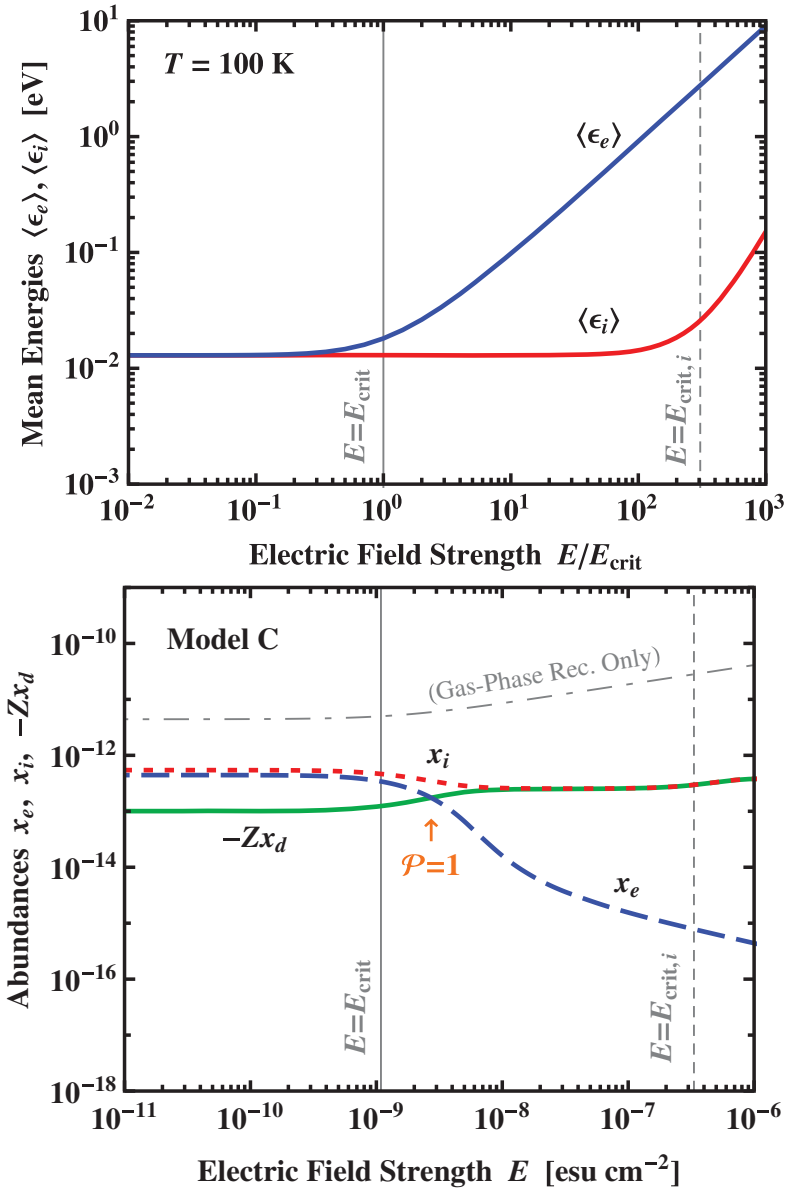

Figure 1.3 Plasma heating by strong electric field (upper panel) and change of the ionization fraction due to the plasma heating (lower panel), which are shown in Okuzumi & Inutsuka (2015). In the upper panel, mean kinetic energies of electrons and ions as a function of the electric field strength. The electric field strength is normalized by a critical electric field strength which electron heating sets in. In the lower panel, ion abundance x_i (dotted curve), electron abundance x_e (dashed curve), and grain charge abundance $-Zx_d$ (solid curve) as a function of the electric field strength. The ionization reaction is solved with a parameter set, model C in Okuzumi & Inutsuka (2015).

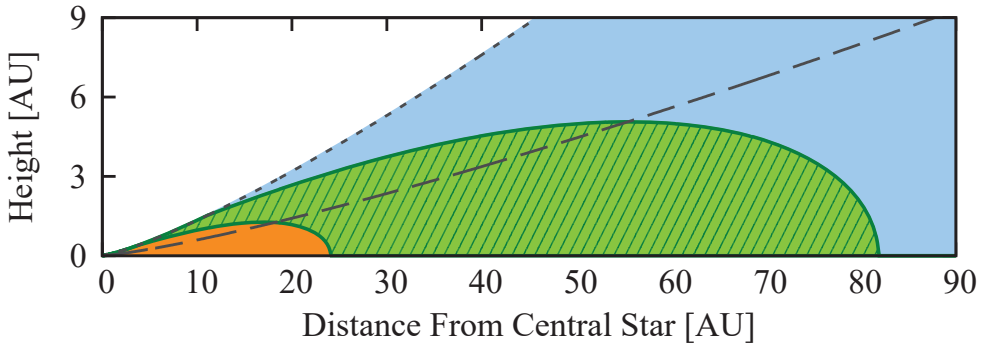

Figure 1.4 Electron-heating zone (grean), ohmic dead zone (orange), and MRI-active region (blue) in the cross section of a protoplanetary disk, which are shown in Mori & Okuzumi (2016). The minimum solar nebula is used as the disk model.

easily heated compared to ions because light particles are easily scattered. Therefore, the sufficiently developed electric fields of MRI turbulence increase electron temperature in a weakly ionized gas. The heated electrons can become sufficiently high temperature for collisional ionization, which is known as a phenomenon of electron discharge. If this process works, MRI turbulence sustains (Muranushi et al., 2012).

However, the estimation does not consider the balance between ionization and recombination. Okuzumi & Inutsuka (2015, henceforth OI15) investigated ionization balance varying electric field strength. They found the reduction of ionization fraction by heated electrons sticking to dust grains before the collisional ionization occurs (lower panel of Figure 1.3). The heated electrons frequently collide with and stick to dust grains. As a result, the electron heating decreases the ionization fraction. They also suggested that a region where MRI is suppressed enlarges in the dusty disk.

Our previous work (Mori & Okuzumi, 2016, henceforce MO16) investigated where the electron heating takes place and, moreover, might suppress MRI. We found the electron heating occurs in large regions of protoplanetary disks, which is called “e-heating zone” (Figure 1.4). Especially, because the region locates outside the dead zones, electron heating would effectively enlarge dead zones. Also, we estimated the strength of magnetic

turbulence in e-heating zones with a simple scaling relation between the Maxwell stress and current density. In the e-heating zone, the current density was suggested to be much less than that in fully developed MRI turbulence. Thus, the previous concluded that electron heating would suppress the MRI turbulence. However, the existence of the scaling relation is unclear because many previous studies have not focused on the relation of current density to the Maxwell stress. Moreover, the estimation has assumed a current density where MRI is saturated. Thus, actually, the possibility of suppressing MRI by electron heating has been debatable.

1.3.3 MHD Disk Wind

We here briefly introduce the disk wind by magnetic fields. MHD disk wind is a mechanism to flow out gas from the disks, and also removes the angular momentum and energy from the disk. Blandford & Payne (1982) found the mechanism that accelerates gas with the centrifugal force. The mechanism is often explained by an analogy of a bead (gas parcel) on a wire (magnetic field) shown in Figure 2 in Spruit (1996). Here, we consider a magnetic field line which threads the disk and rotates with the disk rotation. If the magnetic field is strong and gas pressure is weak, the field line rigidly rotates and has the same angular velocity with a foot point, which is the place where the field threads the disk. The gas which is forced to rotate rapidly gets the angular momentum through the field. As a result, the gas is accelerated outward. When the poloidal field is weak, the magnetic field no longer rotates in the rigid body. The velocity approaches the Kepler rotation speed at the place. In that case, the gas is pushed out by the magnetic field pressure strongly wound in the toroidal direction.

Previous MHD simulations including the vertical stratification showed the MHD disk wind is launched in the simulation box (Suzuki & Inutsuka, 2009; Bai & Stone, 2013).

Interestingly, even when the Ohmic and ambipolar diffusion is included, the disk wind flows out in totally laminar disks (Bai & Stone, 2013). Since the turbulence drives the disk accretion in the conventional model, this suggests that the accretion mechanisms is determined by the disk wind, rather than the turbulent viscosity. This new picture of disk accretion is called a wind-driven accretion. This model also suggests that the disk accretion and turbulence are not necessary to be related to each other. It impacts the modeling of protoplanetary disks and constructing the planet formation theory.

1.4 Purpose of This Research

For understanding planet formation, it is necessary to understand the protoplanetary disk deeply and to elucidate its structure. Especially, understanding how much and where turbulence occurs is important for the planetary formation process. Furthermore, the turbulent energy dissipation also affects the temperature structure. The disk temperature is quite important because it determines the position of the water snow line which constraints the rocky planet formation. Purpose of this thesis is to understand MRI strength by focusing on the ionization state and to elucidate thermal structure in the magnetized disks. This reserch allows us to understand the structure of protoplanetary disks comprehensively.

To begin with, we further focus on the change in ionization fraction due to electron heating. Our previous study found that electron heating can occur in the outer region. To understand the turbulence structure, we here investigate the magnetic stress and turbulence strength in the presence of electron heating by performing MHD simulations.

Furthermore, we focus on the thermal structure in the laminar region inside. In the laminar region, since turbulent energy dissipation does not occur, a heating profile can be largely different from that of the conventional model. Besides, energy outflow due to disk wind

will affect the gas temperature. We perform MHD simulation with non-ideal MHD effects to understand the thermal structure of the disk.

1.5 Guide of This Thesis

The structure of this thesis is as follows. In Chapter 2, we present the effect of electron heating on the MRI. This section is based on Mori et al. (2017). Here, we show the magnetic turbulence can be suppressed when the strength of electron heating is high. We also investigate the parameter dependence of the Maxwell stress suppressed by electron heating. As a result, we show an analytic formula of the stress in the presence of the electron heating. In Chapter 3, we investigate the thermal structure in the laminar disks with MHD simulations. This chapter is based on Mori, Bai, and Okuzumi, submitted. As a result, we show that accretion heating is much inefficient. We also investigate for various parameters to model the temperature determined by accretion heating. In Chapter 4, we summarize the renewed understanding of the structure of protoplanetary disks. Also, we estimate the migration of snow line with basis on our simulation results, and discuss how the Earth would sustain its water content low. We stress that even if the Earth form in the early phase of the disk evolution, it is difficult to prevent the accretion of water to the Earth. After this chapter, we summarize this thesis and present the conclusion. We also present the remaining problems and future works. Note that through this thesis, we newly define every variables and abbreviation in each chapter for clarity.

Chapter 2

Effects of Electron Heating on the Magnetorotational Instability

Based on Mori, Muranushi, Okuzumi, & Inutsuka (2017), *"Electron Heating and Saturation of Self-regulating Magnetorotational Instability in Protoplanetary Disks"*, DOI: 10.3847/1538-4357/aa8e42.

Abstract

Magnetorotational instability (MRI) has a potential to generate the vigorous turbulence in protoplanetary disks, although its turbulence strength and accretion stress remains debatable because of the uncertainty of MRI with low ionization fraction. We focus on the heating of electrons by strong electric fields which amplifies nonideal magnetohydrodynamic effects. The heated electrons frequently collide with and stick to dust grains, which in turn decreases the ionization fraction and is expected to weaken the turbulent motion driven by MRI. In order to quantitatively investigate the nonlinear evolution of MRI including the electron heating, we perform magnetohydrodynamical simulation with the unstratified shearing box. We introduce a simple analytic resistivity model depending on the current density by mimicking resistivity given by the calculation of ionization. Our simulation confirms that the electron heating suppresses magnetic turbulence when the electron heating occurs with low current density. We find a clear correlation between magnetic stress and its current density, which means that the magnetic stress is proportional to the squared current density. When the turbulent motion is completely suppressed, laminar accretion flow is caused by ordered magnetic field. We give an analytical description of the laminar state by using a solution of linear perturbation equations with resistivity. We also propose

a formula that successfully predicts the accretion stress in the presence of the electron heating.

2.1 Introduction

Magnetorotational instability (MRI) has a potential to generate vigorous turbulence in protoplanetary disks. The turbulent viscosity made by the MRI can explain the accretion rate suggested by observation (e.g., Hawley et al., 1995; Flock et al., 2011). That is why MRI has been expected to be a mechanism generating disk turbulence in most research of the protoplanetary disks. Previous studies have been investigated how MRI turbulence in the disks significantly affects the planetesimal formation. For examples, the vigorous MRI turbulence causes diffusion of the dust condensed region (Carballido et al., 2005; Fromang & Papaloizou, 2006; Fromang & Nelson, 2009; Turner et al., 2010; Zhu et al., 2015) and the collisional fragmentation of grains (Carballido et al., 2010). The disk turbulence is important for both of the disk evolution and planetesimal formation.

However, MRI growth and generation of vigorous magnetic turbulence need the disk to be sufficiently ionized. Decoupling between the gas and magnetic fields due to the low ionization fraction causes the nonideal magnetohydrodynamic (MHD) effects, such as ohmic dissipation, Hall effect, and ambipolar diffusion. The nonideal MHD effects can stabilize MRI (e.g., Fleming et al., 2000; Sano & Stone, 2002b; Bai & Stone, 2011; Bai, 2013; Kunz & Lesur, 2013; Simon et al., 2015). The nonideal MHD effects strongly depend on the ionization fraction. Therefore, it is essential to understand ionization state in the disk to determine the efficiency of MRI and the strength of the resulting turbulence.

Although the theoretical estimate of the turbulence strength in a disk still have large uncertainties, recent disk observations found indirect evidence of the turbulence strength. The disk around HL Tau, which is thought to be typical protoplanetary disks surrounding

T Tauri stars, is observed by ALMA observatory, and then the significantly detailed figure is unveiled with the high spatial resolution (ALMA Partnership et al., 2015). The disk has many axisymmetric rings and gaps approximately within 100 AU from the star. Pinte et al. (2016) reproduced the similar observational image with the radiative transfer simulation and obtained the dust and gas properties. According to the paper, such a clear gap requires for the dust disk to be geometrically thin, which means the weak turbulence as Shakura-Sunyaev alpha parameter $\alpha \lesssim$ a few 10^{-4} (Shakura & Sunyaev, 1973). Moreover, Flaherty et al. (2015) and Flaherty et al. (2017) observed a disk around A-type star, HD163296, and obtained the spectral map that limits on non-thermal gas velocity dispersion which is mainly due to turbulent motion. Flaherty et al. (2017) constrained that the velocity dispersion is less than ~ 0.04 times the sound speed which corresponds to $\alpha \lesssim 10^{-3}$ around midplane. The value is one order of magnitude less than typical α value of fully developed MRI turbulence $\alpha \sim 10^{-2}$. The direct imaging observation of HD163296 by Isella et al. (2016) which observed multiple gaps also suggested weak turbulence from gap width and depth relation, assuming presence of planet in the gaps. These disk observations show a new problem of how such weak turbulence is formed.

In this Chapter, we investigate the effect of electron heating on the MRI. The electron heating is one of the consequences of resistive MHD and has a potential to suppress MRI via changing ionization balance. MRI generates not only magnetic fields but also electric fields in the comoving frame of the gas. The electric fields induced by the MRI heat charged particles, in particular electrons, in the gas due to collision with gas particles (Inutsuka & Sano, 2005). The heated electrons are efficiently removed from the gas phase because they frequently collide with and stick to dust grains (Okuzumi & Inutsuka, 2015, hereafter OI15). Therefore, the electron heating causes a decrease in the ionization fraction, which amplifies the nonideal MHD effects suppressing MRI. Since the electron heating takes place after MRI sufficiently grows, the nonideal MHD effects amplified by

the electron heating can change the picture of MRI behavior even in sufficiently ionized region. Our previous study (Mori & Okuzumi, 2016, hereafter MO16) investigated the region in protoplanetary disks where the electron heating influences MRI. We showed that this suppression mechanism becomes important even in outer regions of protoplanetary disks that retain abundant small dust grains. Since the MRI growth leads to suppress the MRI by itself in the presence of electron heating, the saturated turbulent motion would be weaker than the one of fully developed MRI turbulence. MO16 also estimated the accretion stress of magnetic turbulence by using a scaling relation between the magnetic stress and the current density, and suppose that the accretion stress suppressed by the electron heating can be reduced by more than an order of magnitude.

How much the electron heating suppress MRI is still unclear, although the possibility of occurrence of electron heating in the disks has been investigated. The estimation of turbulence strength in MO16 is based on the scaling relation that has not been verified. In order to confirm the effectiveness for electron heating to suppress magnetic turbulence, accretion stress in the presence of the electron heating should be investigated quantitatively.

Our goal in this work is to quantify the effect of the electron heating on MRI with a numerical simulation. We perform MHD simulations where the suppression of the electric resistivity due to electron heating is modeled by a simple analytic function. Furthermore, we propose a formula that reproduces the Maxwell stress obtained from the simulation, which can be used to take into account the effect of the electron heating on the disk evolution. As a first step, we neglect ambipolar diffusion and the Hall effect, focusing on how the Ohmic resistivity increasing with the electric field strength affects the saturated state of MRI. In addition, although strong electric fields do not only heat electrons but also ions, we also neglect the ion heating which requires much higher electric field strength than electron heating (OI15).

The plan of this Chapter is as follows. In Section 2.2, we present the numerical setup and procedure in our simulations. In Section 2.3, we then show some results and present the interpretations. In Section 2.4, we analytically derive a relation between current density and Maxwell stress. In Section 2.5, we summarize this Chapter and discuss implications for dust diffusion in protoplanetary disks.

2.2 Method

2.2.1 Numerical Method

We perform MHD simulations with a unstratified local shearing box, using Athena, an open source MHD code which uses Godunov's scheme (Stone et al., 2008; Stone & Gardiner, 2010). We adopt a local reference frame (x, y, z) corotating with the Keplerian flow at a fiducial distance r_0 from the central star. The coordinates x, y, and z refer to the radial, azimuthal, and vertical distances from the corotation point, respectively. Neglecting curvature and vertical gravity, the MHD equations in this local coordinate system can be written as

$$\frac{\partial \rho}{\partial t} + \nabla \cdot (\rho \boldsymbol{v}) = 0 \,, \tag{2.1}$$

$$\frac{\partial \boldsymbol{v}}{\partial t} + (\boldsymbol{v} \cdot \nabla)\, \boldsymbol{v} = -2\boldsymbol{\Omega} \times \boldsymbol{v} + 3\Omega^2 \boldsymbol{x} - \frac{1}{\rho}\nabla\left(P + \frac{B^2}{8\pi}\right) + \frac{1}{4\pi\rho}(\boldsymbol{B} \cdot \nabla \boldsymbol{B}) \,, \tag{2.2}$$

$$\frac{\partial \boldsymbol{B}}{\partial t} = -c\nabla \times \boldsymbol{E} \,, \tag{2.3}$$

where $\boldsymbol{v}$ is the gas velocity, ρ is the gas density, P is the gas pressure, Ω is the angular velocity at radius r_0, $\boldsymbol{B}$ is the magnetic field, $\boldsymbol{E}$ is the electric field, and c is the speed of light. In this Chapter, we assume isothermal fluid and use the isothermal equation of state

for an ideal gas,

$$P = c_s^2 \rho \,, \tag{2.4}$$

where c_s is the sound speed of isothermal gas and constant. The electric field $\boldsymbol{E}$ in this reference frame is related to the electric field $\boldsymbol{E}'$ in the comoving frame of the gas,

$$\boldsymbol{E} = \boldsymbol{E}' - \frac{1}{c}\boldsymbol{v} \times \boldsymbol{B} \,, \tag{2.5}$$

by the Lorentz transformation in the limit of small velocity. To close the system of equations, we employ the Ohm's law,

$$\boldsymbol{J} = \frac{c^2}{4\pi\eta(E')}\boldsymbol{E}' \,, \tag{2.6}$$

where $\boldsymbol{J} = (c/4\pi)\nabla \times \boldsymbol{B}$ is the current density. In this study, we assume that the electric resistivity η depends on the amplitude of the electric field strength, $E' = |\boldsymbol{E}'|$, which is the case when electron heating changes the ionization fraction.

The dependence of η on E' was investigated in (OI15). OI15 calculated the ionization fraction from the ionization equilibrium including two important effects of plasma heating, i.e., the amplification of plasma adsorption onto dust grains and impact ionization by energetic plasma. The amplification of plasma adsorption decreases plasma abundance, while the impact ionization increases plasma abundance. They showed that the amplification of plasma adsorption occurs at lower E' than impact ionization. In this work, we focus only on the amplification of plasma adsorption amplified by the electron heating and neglect impact ionization.

In this Chapter, we use an analytical resistivity model that mimics the behavior of η as a function of E' due to the electron adsorption which is based on OI15. Figure 2.1 shows

a schematic picture of our resistivity model. Effective electric resistivity is determined by the smaller of the electron and ion resistivity. The horizontal gray lines show electron and ion resistivity in the case without electron heating. The critical electric field strength $E_{\rm EH}$ shows the threshold of electric field strength where electron heating occurs. For $E' > E_{\rm EH}$, the resistivity increases with increase of E' due to dust adsorption of heated electrons. When E' is so small that electron heating does not work, i.e. $E' \ll E_{\rm EH}$, electron resistivity is much smaller than ion resistivity. In the case, the effective resistivity is equal to electron resistivity without electron heating which is constant. On the other hand, the electron resistivity in $E' > E_{\rm EH}$ increases with increases of E' because electron abundance decreases due to electron heating. In this case, the effective resistivity also increases. At $E' \gg E_{\rm EH}$, electron resistivity is larger than ion resistivity, and therefore the effective resistivity is determined by ion resistivity and constant.

In this work, we focus only on the resistivity increasing by the electron heating but does not address an instability of electric fields caused by negative differential resistance, $dJ/dE < 0$ (see Section 6.1 in OI15). In this work, the gradient of η to E' is modified to be shallower than the resistivity given in OI15. In order to satisfy $dJ/dE = 1/(d(\eta J)/dJ) > 0$, the power-law index of η to J is taken to be larger than -1.

Imitating the J–E' relation of OI15 including electron heating, we give the simple analytical resistivity model where the resistivity increases with an increase of E' or J. In Figure 2.2, we show a schematic diagram of J–E' relation including our resistivity model. The resistivity η is written as

$$\eta = \begin{cases} \eta_0 \,, & J < J_{\rm EH} \,, \\ \eta_0 \left(\dfrac{J}{J_{\rm EH}} \right)^{1/\epsilon \, -1} \,, & J_{\rm EH} < J < 1000^{\epsilon/(1-\epsilon)} J_{\rm EH} \,, \\ 1000\eta_0 \,, & 1000^{\epsilon/(1-\epsilon)} J_{\rm EH} < J \,, \end{cases} \tag{2.7}$$

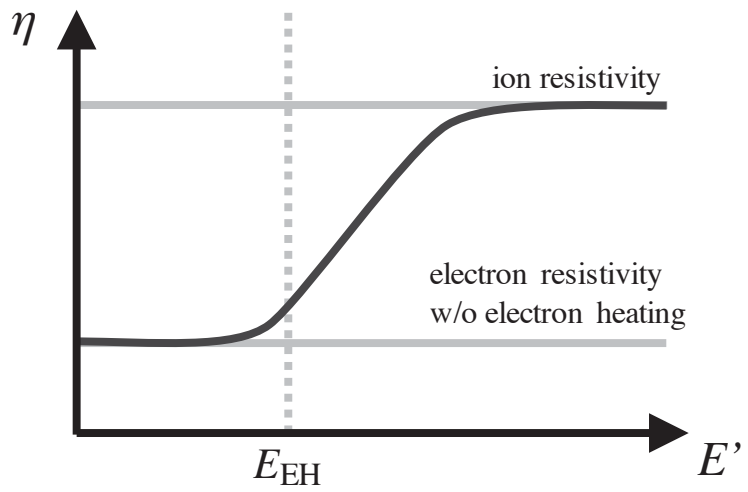

Figure 2.1 Schematic diagram of dependence of resistivity as a function of E' in OI15 that includes amplification of the dust adsorption by the electron heating. The dominant charge careers change from electrons to ions with increasing E' due to reduction of electron abundance by the electron heating.

where η_0 is the initial resistivity, ϵ is a constant value sufficiently less than unity, and $J_{\rm EH}$ is the current density at which the electron heating sets in. In this Chapter, we take ϵ to be 0.1, and $J_{\rm EH}$ to be the arbitrary parameter. Here, we assume that the ion resistivity is higher than the electron resistivity by a factor of 1000.

At $E_{\rm EH} < E' \lesssim 1000 E_{\rm EH}$, current density is approximately equal to $J_{\rm EH}$ in this model. Therefore, $J_{\rm EH}$ also approximately corresponds to the saturated current density. The difference between the saturated current density and $J_{\rm EH}$ is at most smaller than a factor of two.

2.2.2 Simulation Settings

We use a shearing box with a uniform shear flow with the background azimuthal velocity of $-1.5\Omega x$. The simulation box sizes in the radial, azimuthal, and vertical direction are H, $2\pi H$, and H, respectively, where H is the gas scale height, c_s/Ω. We impose the shearing

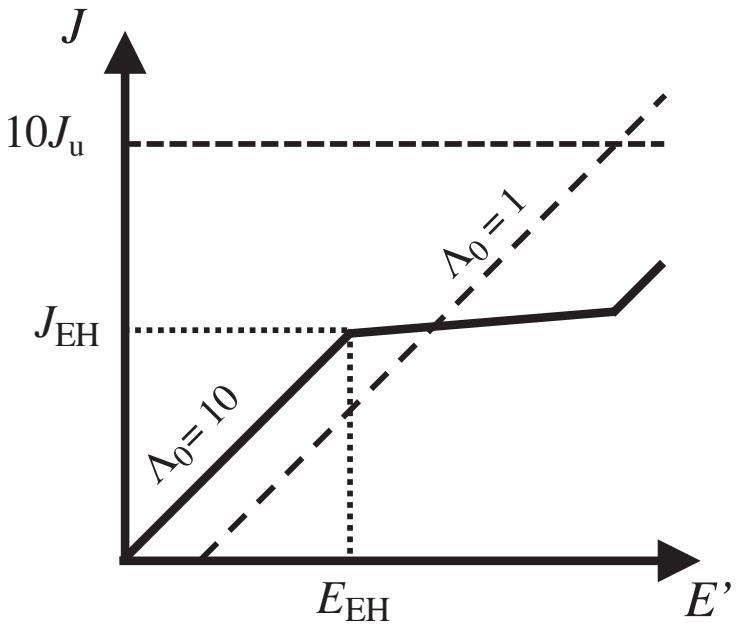

Figure 2.2 Schematic diagram of the simplified J–E' relation that we use in this Chapter. We take the initial Elsasser number to be $\Lambda_0 = 10$ in the fiducial model. $J_{\rm EH}$ is the current density at which electron heating sets in, and horizontal dashed line of $10J_{\rm u}$ approximately corresponds to the current density of fully developed MRI turbulence (Muranushi et al., 2012), which means the maximum current density. The simulations are performed with varying different values of $J_{\rm EH}$ below $10J_{\rm u}$.

periodic boundary condition for x and the periodic boundary condition for y and z.

We take the computational units of length, time, and density to be, respectively, H, Ω^{-1}, and the initial gas density ρ_0. Therefore, the unit of velocity is $c_{\rm s}$, and the unit of pressure is the initial gas pressure $P_0 = \rho_0 c_{\rm s}^2$. The unit of magnetic field strength is

$$B_{\rm u} = \sqrt{4\pi P_0}\,. \tag{2.8}$$

We take the unit of current density to be

$$J_{\rm u} = \frac{c}{4\pi}\frac{B_{\rm u}}{H}\,. \tag{2.9}$$

We nondimensionalize the Ohm's law $E = (4\pi\eta/c^2)J$ as $E/E_\mathrm{u} = (\eta/\eta_\mathrm{u})(J/J_\mathrm{u})$, where

$$E_\mathrm{u} = \frac{4\pi\eta_\mathrm{u} J_\mathrm{u}}{c^2} = \frac{c_\mathrm{s}}{c} B_\mathrm{u} \tag{2.10}$$

and

$$\eta_\mathrm{u} = H^2\Omega = Hc_\mathrm{s} \, . \tag{2.11}$$

The initial vertical magnetic field is uniform and its strength is

$$B_{z0} = \sqrt{2}\beta_0^{-1/2} B_\mathrm{u} \, , \tag{2.12}$$

where

$$\beta_0 = \frac{8\pi P_0}{B_{z0}^2} \tag{2.13}$$

is the initial plasma beta. We consider the situation where MRI would be fully active if electron heating were absent. The activity of MRI is determined by the Elsasser number (e.g., Sano & Miyama, 1999),

$$\Lambda_z = \frac{v_{\mathrm{A}z}^2}{\eta\Omega} \, , \tag{2.14}$$

where

$$v_{\mathrm{A}z} = \frac{B_z}{\sqrt{4\pi\rho}} \tag{2.15}$$

is the Alfvén velocity of the vertical magnetic field. MRI is fully active when $\Lambda_z \gg 1$, while the resistivity suppresses the most unstable MRI mode when $\Lambda_z \ll 1$. We choose the value of η_0 so that the Elsasser number in the initial state Λ_0 is equal to 10. Λ_0 is expressed as $\Lambda_0 = v_{\mathrm{A}0}^2/\eta_0\Omega$, where $v_{\mathrm{A}0}$ is the Alfvén velocity of initial state, $v_{\mathrm{A}0} = B_{z0}^2/\sqrt{4\pi\rho_0}$. For this value of Λ_0, the Elsasser number in the final saturated state also satisfies $\Lambda_z \gg 1$ as long as electron heating is neglected ($\eta = \eta_0$ for all E') because we generally have $v_{\mathrm{A}z} > v_{\mathrm{A}0}$. In order to investigate dependence on the critical current density J_EH, we take J_EH to

be less than $10J_{\rm u}$ which approximately corresponds to the maximum current density, at which current density is saturated in fully developed MRI turbulence (Muranushi et al., 2012). We give random perturbations of pressure δP and velocity $\delta \boldsymbol{v}$ whose the maximum amplitude are $\delta P/P_0 = 5 \times 10^{-5}$ and $|\delta \boldsymbol{v}|/c_{\rm s} = 2 \times 10^{-5}$, respectively. The amplitudes are taken to be so small that they never exceed the amplitudes of the perturbations left after electron heating suppresses MRI turbulence. We also take into account a small viscosity which is effective to damp initial perturbations.

The numerical resolution is taken to be 64, $64/\pi$, and 64 grids per H in the x, y, and z directions, respectively. In order to properly resolve the MRI turbulence, we take the vertical grid spacing Δz to be much smaller than the most unstable wavelength $\lambda_{\rm MRI}$ (Noble et al., 2010). In our fiducial model, $\lambda_{\rm MRI}/\Delta z \approx 20$–$120$ in the final state. In order to resolve MRI, $\lambda_{\rm MRI}/\Delta z \gtrsim 6$ is required (Sano et al., 2004). Our resolution satisfies this requirement. The Courant-Friedrichs-Lewy number of 0.4 is used.

2.2.3 Initial Conditions

We take $\beta_0 = 10^4$ and $\Lambda_0 = 10$ as the fiducial parameters. For this set of β_0 and Λ_0, we consider 10 different values of $J_{\rm EH}$: $J_{\rm EH}/J_{\rm u} = 1 \times 10^{-3}, 3 \times 10^{-3}, 1 \times 10^{-2}, 3 \times 10^{-2}, 1 \times 10^{-1}, 3 \times 10^{-1}, 1, 3, 10$ and ∞, where $J_{\rm EH}/J_{\rm u} = \infty$ corresponds to the case without electron heating. We also perform simulations with different values of β_0 and Λ_0 to see the dependence on these parameters. We take β_0 as $\beta_0 = 10^3, 10^4, 10^5$ and Λ_0 as $\Lambda_0 = 30, 10, 0.3$, with $J_{\rm EH} = 0.003, 0.03, 0.3, 3, \infty$ for each set of β_0 and Λ_0. We use these results for checking accuracy of the analytic $\alpha_{\rm M}$–$J_{\rm EH}$ relation presented in Section 2.4.

Table 2.1 Summary of results.

Label	$J_{\rm EH}$	β	Λ_0	$\left\langle\left\langle B^2\right\rangle\right\rangle/(8\pi P_0)$	$\alpha_{\rm M}$	$\alpha_{\rm R}$	$\langle\langle J\rangle\rangle/J_{\rm u}$
EH0001	0.001	10^4	10	1.00×10^{-4}	7.21×10^{-9}	9.00×10^{-11}	1.75×10^{-3}
EH0003	0.003	10^4	10	1.00×10^{-4}	6.49×10^{-8}	8.10×10^{-10}	5.25×10^{-3}
EH001	0.01	10^4	10	1.03×10^{-4}	7.21×10^{-7}	9.00×10^{-9}	1.75×10^{-2}
EH003	0.03	10^4	10	1.30×10^{-4}	6.49×10^{-6}	8.10×10^{-8}	5.25×10^{-2}
EH01	0.1	10^4	10	4.15×10^{-4}	6.47×10^{-5}	3.37×10^{-4}	1.71×10^{-1}
EH03	0.3	10^4	10	1.57×10^{-3}	3.08×10^{-4}	9.73×10^{-4}	4.62×10^{-1}
EH1	1	10^4	10	5.48×10^{-3}	1.53×10^{-3}	1.98×10^{-3}	1.39
EH3	3	10^4	10	1.17×10^{-2}	4.79×10^{-3}	2.95×10^{-3}	3.53
EH10	10	10^4	10	3.75×10^{-2}	1.69×10^{-2}	6.15×10^{-3}	8.23
noEH	∞	10^4	10	7.15×10^{-2}	3.15×10^{-2}	9.67×10^{-3}	1.25×10^{1}
B3-EH	0.003	10^3	10	1.00×10^{-3}	1.41×10^{-7}	1.37×10^{-8}	4.60×10^{-3}
B3-EH	0.03	10^3	10	1.02×10^{-3}	1.41×10^{-5}	1.37×10^{-6}	4.60×10^{-2}
B3-EH	0.3	10^3	10	2.15×10^{-3}	5.99×10^{-4}	3.34×10^{-4}	4.22×10^{-1}
B3-EH	3	10^3	10	4.41×10^{-2}	2.52×10^{-2}	1.08×10^{-2}	3.56
B3-noEH	∞	10^3	10	2.22×10^{-1}	1.09×10^{-1}	2.79×10^{-2}	1.55×10^{1}
B5-EH0003	0.003	10^5	10	1.04×10^{-5}	2.70×10^{-8}	4.27×10^{-11}	5.98×10^{-3}
B5-EH003	0.03	10^5	10	4.90×10^{-5}	2.69×10^{-6}	4.29×10^{-9}	5.97×10^{-2}
B5-EH03	0.3	10^5	10	1.66×10^{-3}	1.19×10^{-4}	2.91×10^{-4}	5.25×10^{-1}
B5-EH3	3	10^5	10	4.07×10^{-3}	1.66×10^{-3}	1.35×10^{-3}	3.49
B5-noEH	∞	10^5	10	2.56×10^{-2}	1.17×10^{-2}	4.09×10^{-3}	9.34
L1-EH0003	0.003	10^4	1	1.00×10^{-4}	3.89×10^{-8}	4.86×10^{-10}	4.07×10^{-3}
L1-EH003	0.03	10^4	1	1.18×10^{-4}	3.89×10^{-6}	4.86×10^{-8}	4.07×10^{-2}
L1-EH03	0.3	10^4	1	8.58×10^{-4}	1.64×10^{-4}	1.04×10^{-3}	3.50×10^{-1}
L1-EH3	3	10^4	1	1.08×10^{-2}	4.07×10^{-3}	3.16×10^{-3}	2.78
L1-noEH	∞	10^4	1	3.64×10^{-2}	1.67×10^{-2}	5.82×10^{-3}	8.20
L30-EH0003	0.003	10^4	30	1.00×10^{-4}	8.28×10^{-8}	1.03×10^{-9}	5.94×10^{-3}
L30-EH003	0.03	10^4	30	1.39×10^{-4}	8.28×10^{-6}	1.03×10^{-7}	5.94×10^{-2}
L30-EH03	0.3	10^4	30	1.84×10^{-3}	3.80×10^{-4}	1.32×10^{-3}	5.22×10^{-1}
L30-EH3	3	10^4	30	1.36×10^{-2}	5.68×10^{-3}	2.83×10^{-3}	3.93
L30-noEH	∞	10^4	30	7.28×10^{-2}	3.26×10^{-2}	1.01×10^{-2}	1.28×10^{1}

2.3 Simulation Results

Table 2.1 summarizes the parameter sets explored in this study. We express the volume-averaged quantities as $\langle ... \rangle$ and the time- and volume-averaged quantities as $\langle\langle ... \rangle\rangle$. The volume averages are calculated over the entire simulation box, and the time averages are calculated from 100 to 150 in units of the orbital period $2\pi/\Omega$. The range of time integration is taken so that the final saturated state dominates the average.

The most important quantity obtained from the simulations is the accretion stress, which controls the disk evolution. The accretion stress can be characterized in terms of the Shakura-Sunyaev alpha parameter α, which is defined as the time- and volume-averaged accretion stress divided by the time- and volume-averaged pressure, which is equal to P_0 for an isothermal gas,

$$\alpha = \alpha_{\rm R} + \alpha_{\rm M} = \frac{\left\langle\left\langle \rho v_x \delta v_y \right\rangle\right\rangle}{P_0} + \frac{\left\langle\left\langle -B_x B_y \right\rangle\right\rangle}{4\pi P_0}, \tag{2.16}$$

where we express $\left\langle\left\langle \rho v_x \delta v_y \right\rangle\right\rangle / P_0$ and $\left\langle\left\langle -B_x B_y \right\rangle\right\rangle / (4\pi P_0)$ as, respectively, $\alpha_{\rm R}$ and $\alpha_{\rm M}$.

2.3.1 The Fiducial Case

Figure 2.3 shows the saturated state ($t = 60$ orbits) observed in our fiducial simulations with $J_{\rm EH}/J_{\rm u} = 0.03$. The saturated state for the case without electron heating $J_{\rm EH}/J_{\rm u} = \infty$ is also shown for comparison. We also show the crosscuts of the saturated state on the x–z and y–z planes for $J_{\rm EH} = 0.03, 0.3, 3$, and ∞ in Figure 2.4 . We find that a laminar flow with an ordered magnetic field dominates the saturated state for $J_{\rm EH}/J_{\rm u} = 0.03$, whereas the turbulent magnetic fields are generated in the case without electron heating. Comparing these two case, we confirm that electron heating suppress turbulent motion that is characteristic of MRI. Moreover, the magnetic field strength $|\boldsymbol{B}|$ is also largely

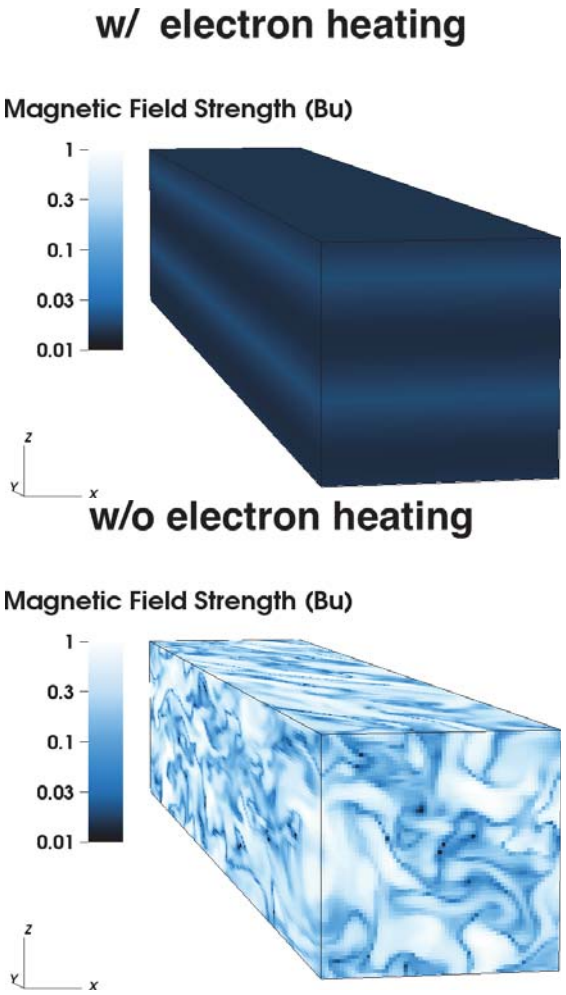

Figure 2.3 Snapshot of magnetic field strength $|\boldsymbol{B}|/B_{\mathrm{u}}$ at 60 orbits for $J_{\mathrm{EH}}/J_{\mathrm{u}} = 0.03$ (left) and for the case without electron heating $J_{\mathrm{EH}}/J_{\mathrm{u}} = \infty$ (right).

suppressed for the laminar case.

In Figure 2.4, we see that the azimuthal magnetic fields for $J_{\mathrm{EH}}/J_{\mathrm{u}} = 0.03$ are sinusoidal in the vertical direction, with a wavelength as large as the vertical box size. In the presence of electron heating, the perturbations on small scales stop growing due to the increased resistivity, while perturbations on larger scales grow. For this reason, the magnetic field inside the box tends to be dominated by the component whose wavelength is equal to the box size. We also see that small structure of magnetic fields appears with increasing J_{EH}. This too can be understood by the fact that the resistivity increased by the electron heating

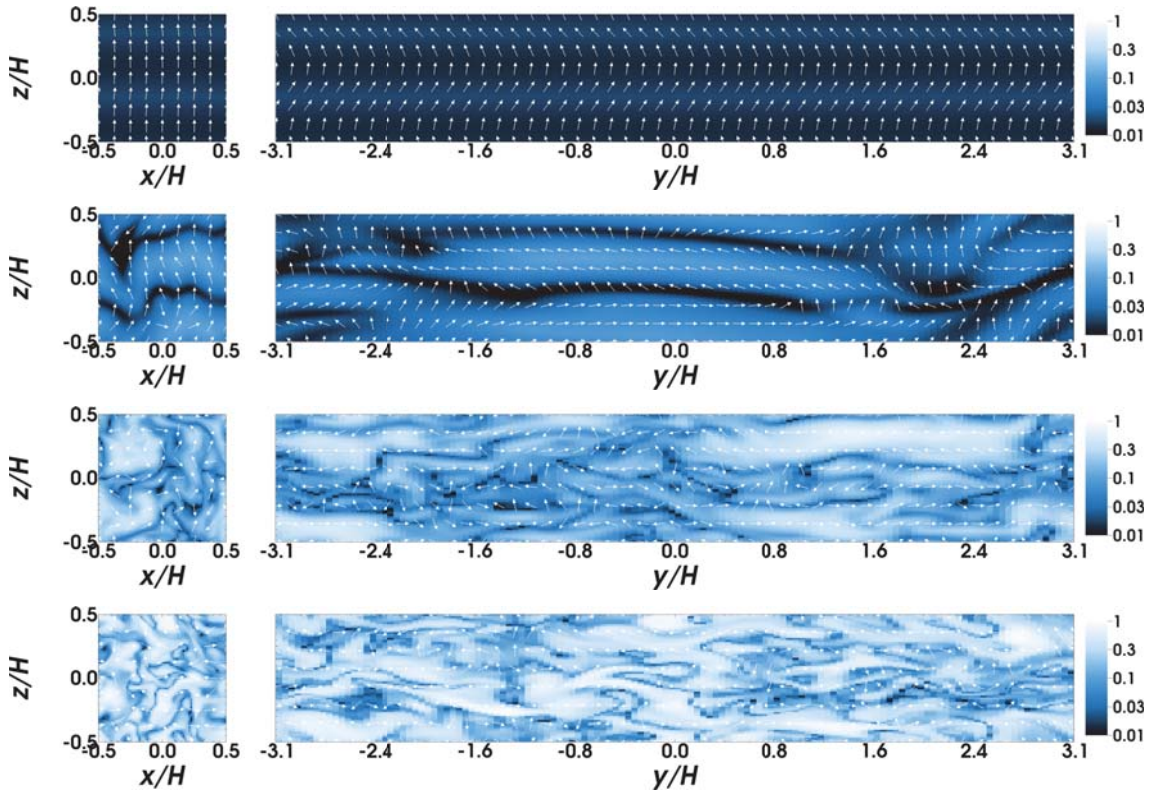

Figure 2.4 Slices in the x–z plane at $y = 0$ and in the y–z at $x = 0$ of the magnetic field strength $|\boldsymbol{B}|/B_{\rm u}$ (color) and direction of the magnetic field (arrows) at 60 orbits for $J_{\rm EH}/J_{\rm u} = 0.03$, 0.3, 3, and ∞, from top to bottom.

suppresses the perturbations on small scale.

In order to see that the resulting J and E' follow the given J–E' relation, in Figure 2.5, we show the evolutionary tracks of the volume-averaged current density $\langle J \rangle$ and electric field strength $\langle E' \rangle$ in the J–E' plane. The current densities initially grow along the line of $\Lambda_0 = 10$ and then branch off the line after they reach $J_{\rm EH}$. We confirm the resulting $\langle J \rangle$–$\langle E' \rangle$ tracks almost go along with J–E' relation we give. We also find that, in the absence of electron heating cases, $\langle J \rangle$ and $\langle E' \rangle$ are saturated near the line corresponding to $\Lambda_0 = 0.1$.

In Figure 2.6, we show the time evolution of the volume-averaged Maxwell stress for different values of $J_{\rm EH}$. MRI grows linearly in the first few orbits, and then the Maxwell

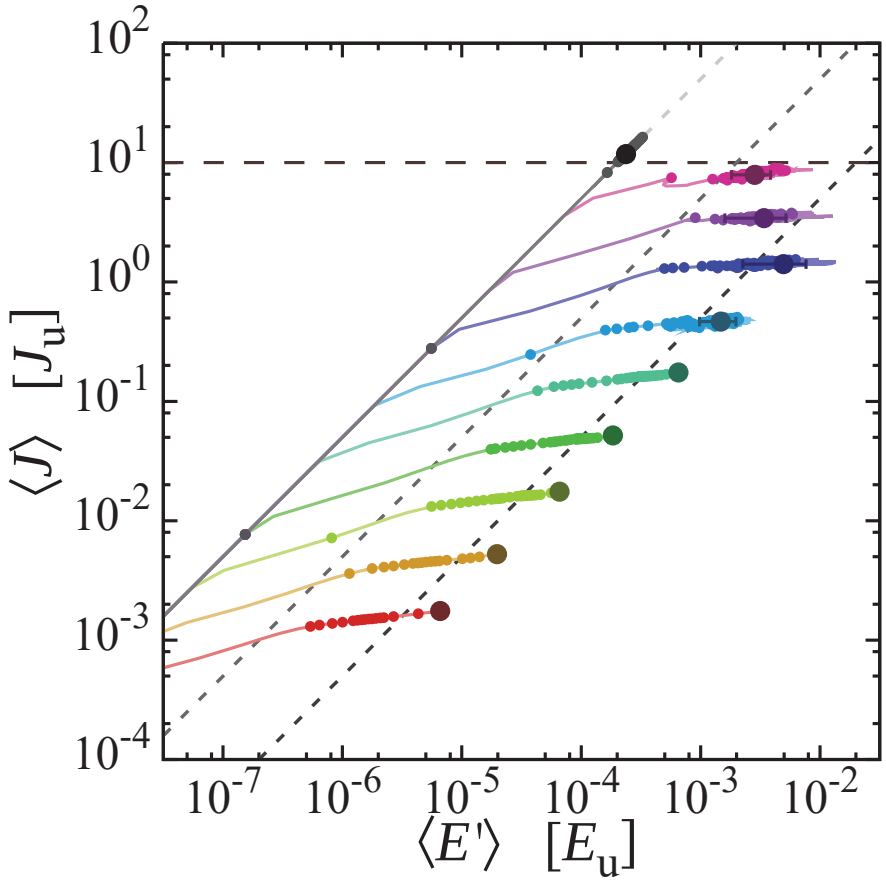

Figure 2.5 Evolution tracks of the volume-averaged electric field strength $\langle E' \rangle$ (x-axis) and current density $\langle J \rangle$ (y-axis) mapped in the J–E' plane. Curves of different colors correspond to runs of different values of $J_{\rm EH}$ (from bottom to top, $J_{\rm EH}/J_{\rm u} = 0.001, 0.003, 0.01, 0.03, 0.1, 0.3, 1, 3, 10$ and ∞). The dashed lines indicate the linear relations $\langle J \rangle = c^2/(4\pi\eta_0)\langle E' \rangle$, where $\eta_0 = v_{\rm Az0}^2/\Lambda_0\Omega$ (see the text after Equation (2.14)) with $\Lambda_0 = 10$ (light gray line), 1 (gray line), and 0.1 (dark gray line), respectively. The small circles are plotted at every one orbit to visualize the rates of change in $\langle J \rangle$ and $\langle E' \rangle$. The dark filled circles indicate the final saturated states. The horizontal dotted line is $J = 10J_{\rm u}$, which is the saturated current density in the fully developed MRI turbulence (Muranushi et al., 2012).

stress becomes saturated in $\sim$ 30 orbits. We find that the Maxwell stress in the saturated state decreases with decreasing $J_{\rm EH}$, which means that MRI is stabilized by electron heating. We also find that the Maxwell stress in the saturated state is fluctuating when $J_{\rm EH}/J_{\rm u} > 0.3$ and is highly stationary when $J_{\rm EH}/J_{\rm u} < 0.1$. This suggests that electron

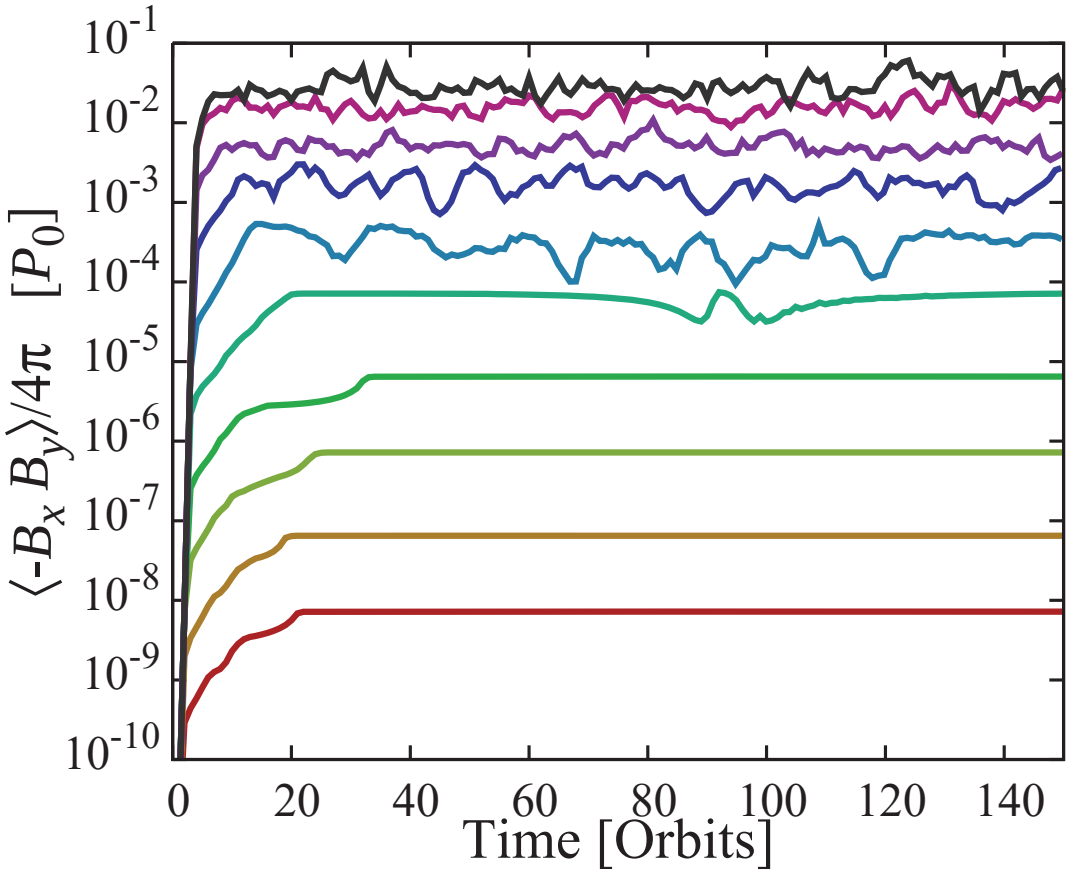

Figure 2.6 Time evolution of the volume-averaged Maxwell stress for different values of $J_{\rm EH}$ (from bottom to top, $J_{\rm EH}/J_{\rm u} = 0.001, 0.003, 0.01, 0.03, 0.1, 0.3, 1, 3, 10$ and ∞). The color scheme is the same as in Figure 2.5.

heating completely suppresses turbulent motion caused by MRI when $J_{\rm EH} < 0.1 J_{\rm u}$. We here define the threshold current density as

$$J_{\rm lam} = 0.1 J_{\rm u} \ . \tag{2.17}$$

At $J \lesssim J_{\rm lam}$, the saturated state is laminar.

Figure 2.7 displays $\alpha_{\rm M}$ as a function of $J_{\rm EH}$. We confirm a positive correlation between $\alpha_{\rm M}$ and $J_{\rm EH}$. By fitting a quadratic function to the data, we obtain the empirical formula

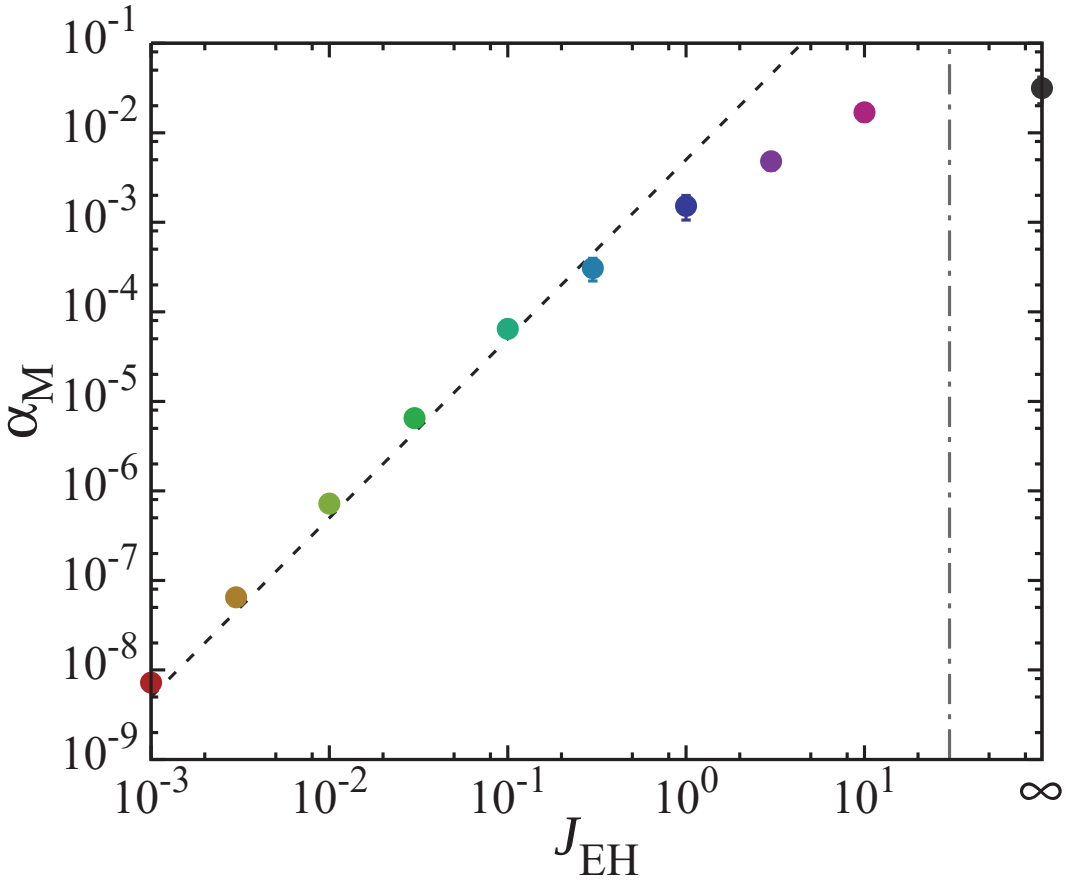

Figure 2.7 Time- and volume-averaged Maxwell stress α_M as a function of J_{EH} (colored dots). The color scheme is the same as in Figure 2.5. The dashed line shows a quadratic fit for low J_{EH}, $\alpha_M = 0.5(J_{EH}/10J_u)^2$.

of the relation,

$$\alpha_M = 0.5\left(\frac{J_{EH}}{10J_u}\right)^2 , \tag{2.18}$$

The dependence on current density, $\alpha_M \propto J^2$, is consistent with a scaling relation obtained by MO16 (Equation (40) in their paper), although the magnitude in their equation is 50 times smaller than obtained here. This empirical fit can be used when J_{EH} is less than J_{lam}.

According to previous studies (e.g., Sano & Stone, 2002b), Λ_z expresses the MRI activity. When the Elsasser number is much higher than unity, MRI can make vigorous magnetic

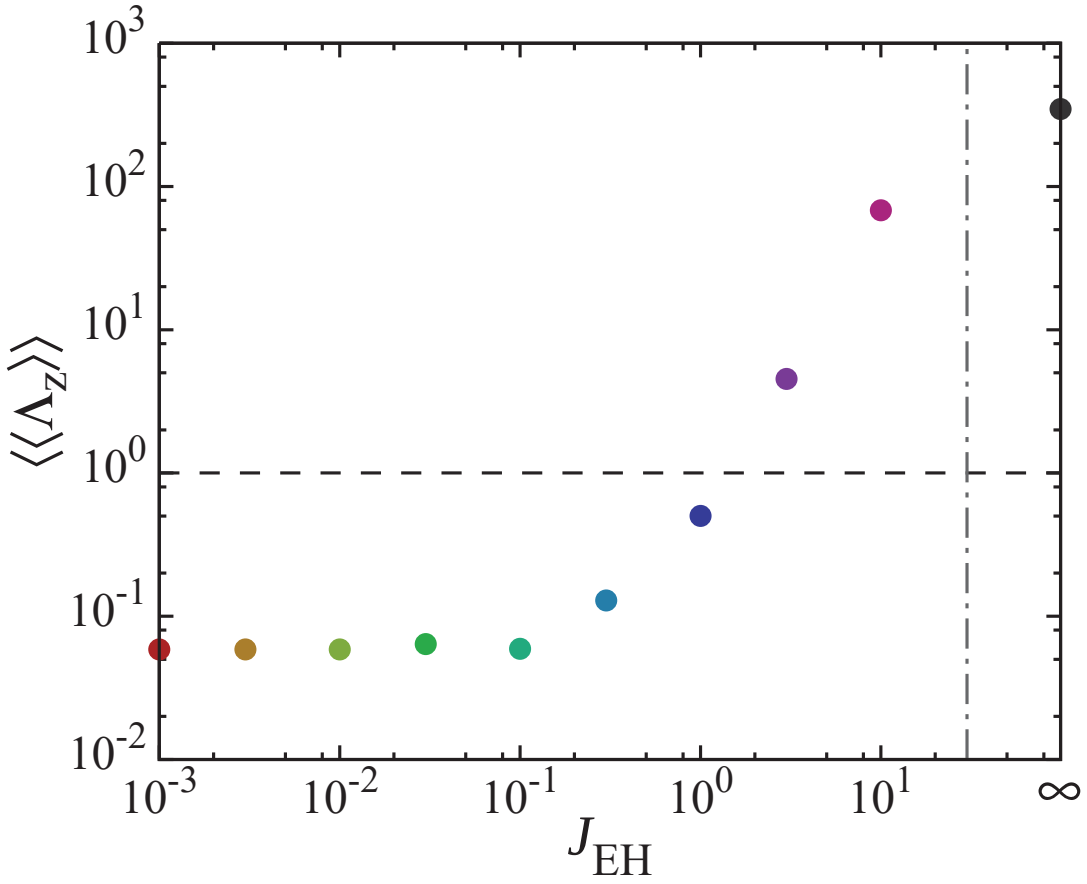

Figure 2.8 Time- and volume-averaged Elsasser number $\langle\langle\Lambda_z\rangle\rangle$ as a function of $J_{\rm EH}$. The dashed line shows $\Lambda = 1$. The color scheme is the same as in Figure 2.5.

turbulence. Figure 2.8 shows the volume- and time-averaged Elsasser number $\langle\langle\Lambda_z\rangle\rangle$ as a function of $J_{\rm EH}$. For $1 < J_{\rm EH}/J_{\rm u} < 10$, we see that although the Elsasser number is higher than unity , $\alpha_{\rm M}$ gradually decreases with decrease of $J_{\rm EH}$ as we see in Figure 2.7. Because the increased resistivity can suppress magnetic fields by the small scale turbulent motion which forms strong current density, the electron heating takes place when the MRI turbulence is generated. We also see that $\langle\langle\Lambda_z\rangle\rangle$ is constant at $J_{\rm EH} < J_{\rm lam}$. This is because η is also constant for $J_{\rm EH} < J_{\rm lam}$ as we see below.

To see why the MRI is quenched in the laminar saturated state, we show the time- and volume-averaged critical wavelength $\langle\langle\lambda_{\rm crit}\rangle\rangle$ in Figure 2.9. The critical wavelength $\lambda_{\rm crit}$

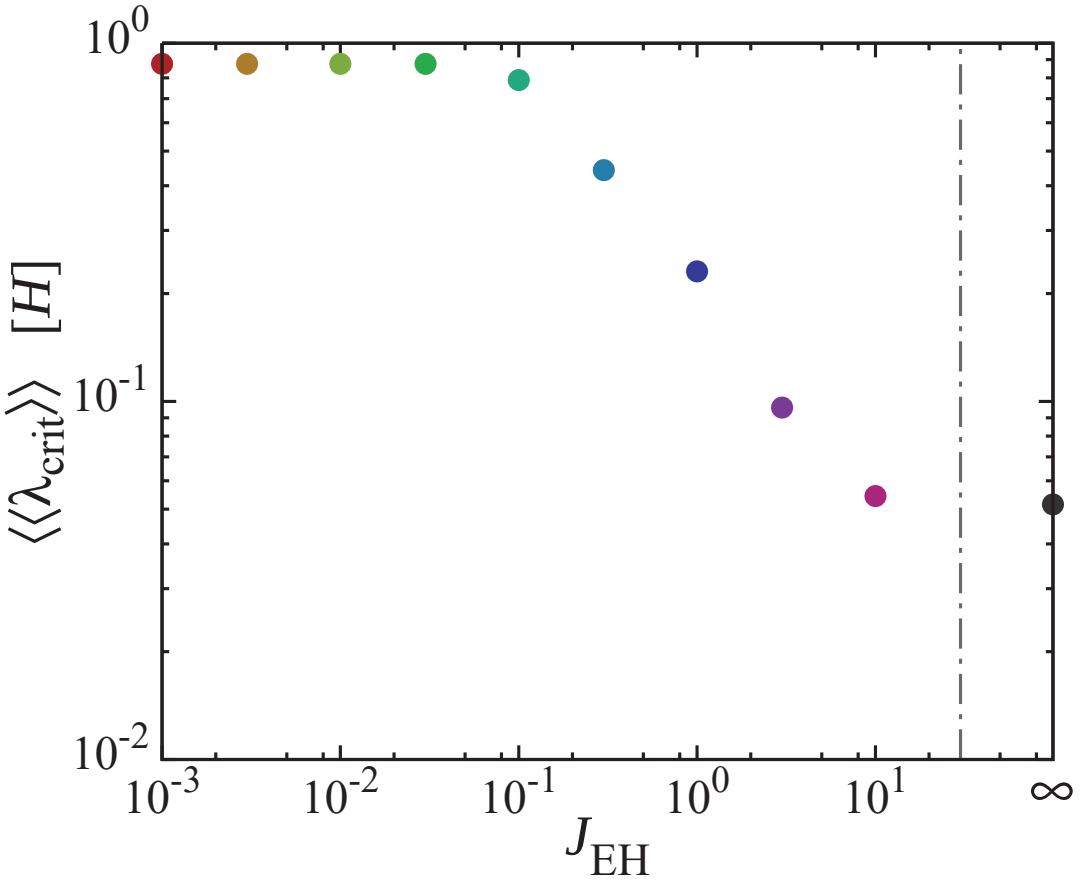

Figure 2.9 Time- and volume-averaged critical wavelength $\langle\langle\lambda_{\rm crit}\rangle\rangle$ as a function of $J_{\rm EH}$. The color scheme is the same as in Figure 2.5.

is the shortest wavelength in unstable MRI mode. This is obtained from the linearized equation system in Sano & Miyama (1999) by assuming growth rate of zero. The critical wavelength in both resistive and ideal MHD is written as

$$\lambda_{\rm crit} = 2\pi \frac{1}{\sqrt{3}} \frac{v_{\rm Az0}}{\Omega} \left(1 + \left(\frac{v_{\rm Az0}^2}{\eta\Omega} \right)^{-2} \right)^{1/2} , \tag{2.19}$$

where $v_{\rm Az0} = B_{z0}/\sqrt{4\pi\rho_0}$. We see that the resulting critical wavelength is approximately equal to simulation box size H for low $J_{\rm EH}$. The MRI growth increases η, which in turn increases the critical wavelength $\lambda_{\rm crit}$ when $\Lambda \lesssim 1$. For this reason, the shortest unstable

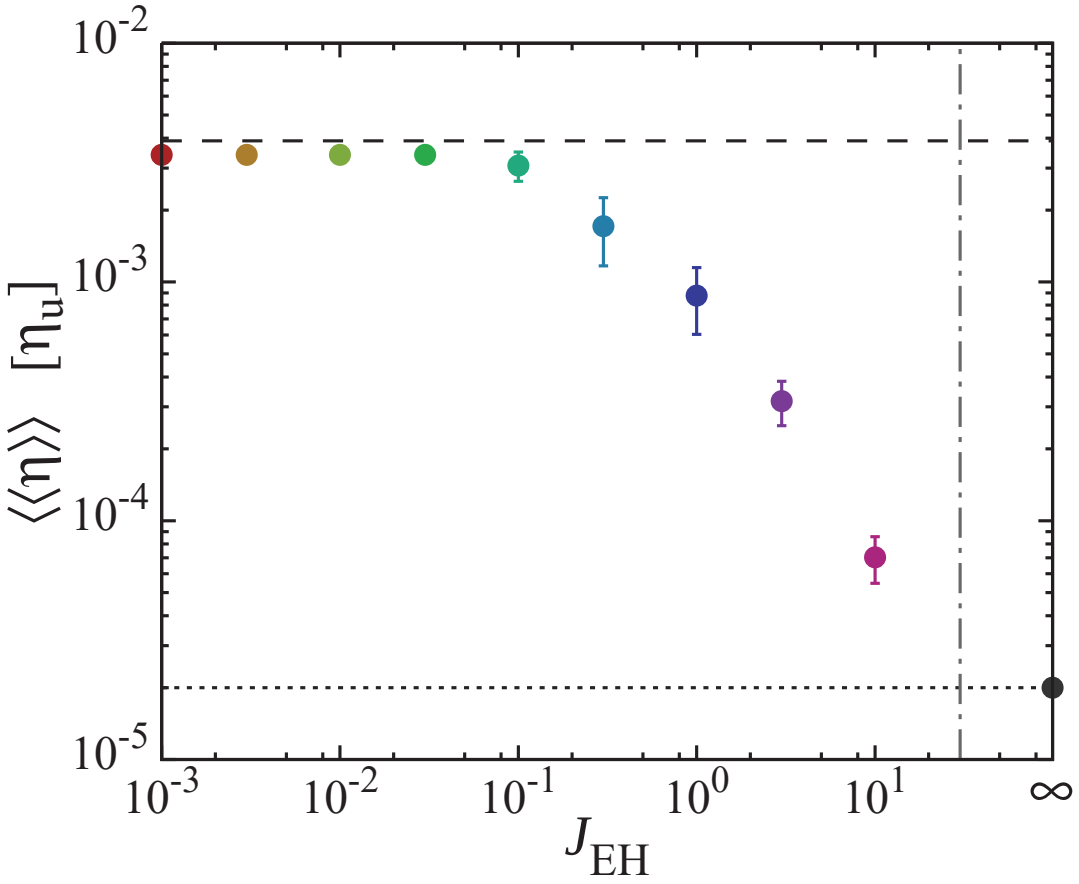

Figure 2.10 Time- and volume-averaged resistivity $\langle\langle\eta\rangle\rangle$ as a function of $J_{\rm EH}$. The dotted line shows the initial resistivity η_0 and the dashed line shows Equation (2.20). The color scheme is the same as in Figure 2.5.

wavelength increases until the wavelength reaches to the box size, and eventually all MRI unstable modes die away. Note that the final state of this simulation would depend on the vertical box size.

Figure 2.10 shows the time- and volume-averaged resistivity $\langle\langle\eta\rangle\rangle$ as a function of $J_{\rm EH}$. In all simulations but with $J_{\rm EH} = \infty$, the final resistivity is higher than the initial value η_0 (shown by the dotted line). We see that the saturated resistivity for low $J_{\rm EH}$ is independent

of $J_{\rm EH}$. This value is given by $\lambda_{\rm crit}(\eta) = H$ in the resistive MHD,

$$\frac{\eta_{\rm lam}}{\eta_{\rm u}} = \frac{2}{\sqrt{\beta_0 8\pi^2/3}} \approx 0.390 \times 10^{-2} \left(\frac{\beta_{z0}}{10^4}\right)^{-1/2} . \tag{2.20}$$

The resistivity cannot exceed this value because any higher resistivity would stabilize all unstable modes that can fit in the simulation box. The fact that $\langle\langle\eta\rangle\rangle$ reaches this critical value explains why the laminar saturated state is realized for $J_{\rm EH} < 0.1 J_{\rm u}$.

We see in Figure 2.6 that the saturated state for the low $J_{\rm EH}$ is steady. Although Figures 2.4 shows that the wavelength in the final state is equal to the vertical box size, the process to the saturated state has not been shown. How is the saturated laminar state determined? In the presence of electron heating, the resistivity also increases with the unstable mode growing. When the increased resistivity reaches the critical resistivity Equation (2.20), MRI is stabilized since the all unstable mode dies away. In this state, if perturbations of magnetic fields grow, then the resistivity is increased and in turn stabilizes the perturbations. On the other hand, if the perturbation is damped from the equilibrium state, then the resistivity becomes smaller and MRI grows again. In other word, the saturated laminar state is determined by the balance between the MRI growth by shear and decay by the increased resistivity. Therefore, the final state must settle into the stable equilibrium state

Lastly, in order to see turbulent activity, we plot the root mean square of the vertical velocity $\left\langle\left\langle v_z^2\right\rangle\right\rangle^{1/2}$ as a function of $J_{\rm EH}$ in Figure 2.11. In particular, the vertical velocity of gas is important for dynamics and spatial distribution of dust in protoplanetary disks. We see that the vertical velocity sharply drops at $J_{\rm EH} \lesssim J_{\rm lam}$, where the saturated state is laminar. Its implications for turbulent mixing of dust particles are discussed in Section 2.5.

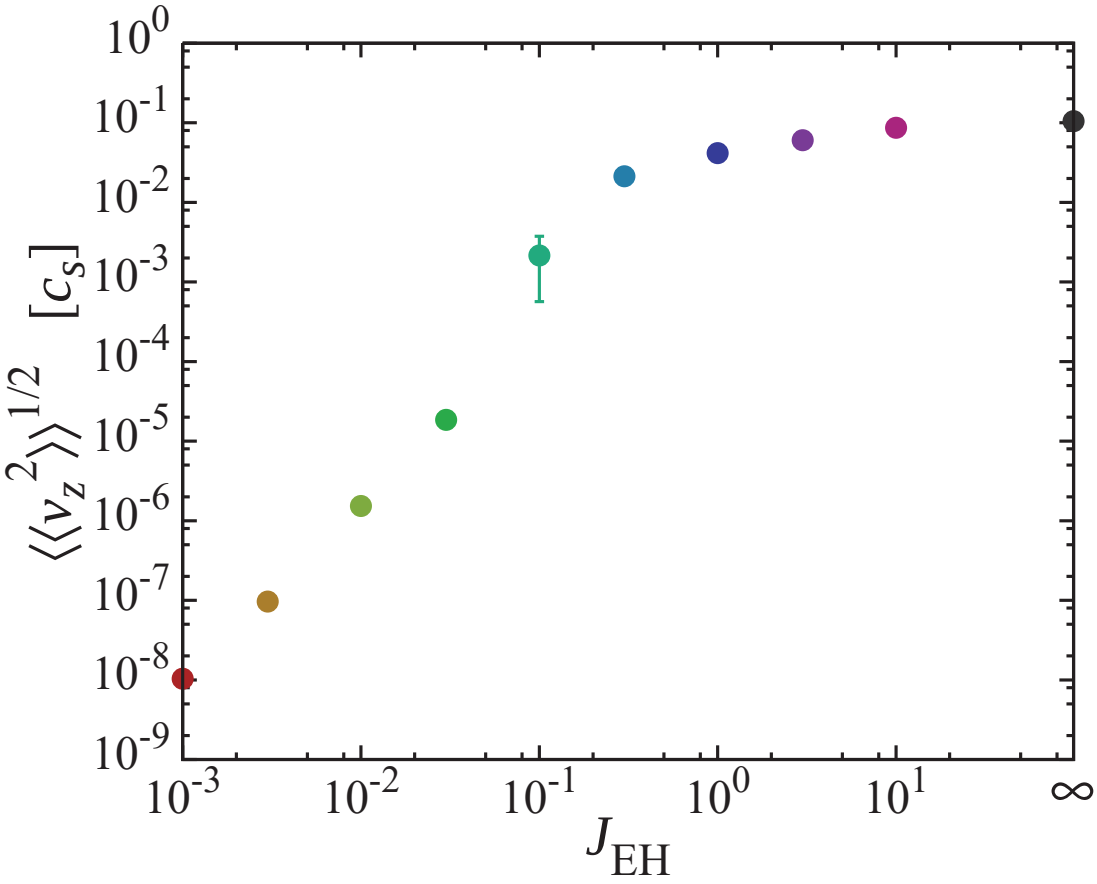

Figure 2.11 Time- and volume-averaged vertical velocity $\left\langle\left\langle v_z^2\right\rangle\right\rangle^{1/2}$ as a function of $J_{\rm EH}$. The color scheme is the same as in Figure 2.5.

2.4 Derivation of Current–Stress Relation

In this section, we derive a relation between $\alpha_{\rm M}$ and $J_{\rm EH}$ which reproduce our simulation results. Because $J_{\rm EH}$ can be calculated from disk parameters, this relation may provide a quantitative prediction for accretion stress without MHD simulations, when the saturated state is determined by the electron heating. For example, this relation would be useful for simplified modeling with disk evolution using α parameter based on MHD simulation with electron heating. We here neglect contribution of Reynolds stress to accretion stress. This is because Maxwell stress is generally larger than Reynolds stress according to Table 3. In addition, we regard the current density in the saturated state as $J_{\rm EH}$.

We first derive an analytical expression of the Maxwell stress in the laminar state, $\alpha_{\rm M,lam}$. To express $\alpha_{\rm M} = \left\langle\left\langle -B_x B_y \right\rangle\right\rangle / (4\pi P_0)$ as a function of $J_{\rm EH}$, we estimate $-B_x B_y / 4\pi P_0$ by using the Ampére's equation $\boldsymbol{J} = c/(4\pi)\nabla \times \boldsymbol{B}$. We take ∇ to be the typical wavenumber $\boldsymbol{k}$. We here consider the vertical sinusoidal wave as we see Figure 2.4, and therefore $\boldsymbol{k} = k_z \mathbf{e}_z$ is assumed. The x-direction component of the current density is described as $J_x \approx -ck_z B_y/4\pi$, and thereby B_y is written as

$$B_y \approx -\frac{4\pi}{ck_z} J_x \, . \tag{2.21}$$

According to Figure 2.9, the critical wavelength in the laminar case is the vertical box size, H. Thus, we here assume that the vertical wavenumber in the saturated state is

$$k_{z,\rm crit} = \frac{2\pi}{H} \, . \tag{2.22}$$

Using Equation (2.21) and Equation (2.22), we express $-B_x B_y / 4\pi P_0$ as

$$-\frac{B_x B_y}{4\pi P_0} \approx -\frac{100}{4\pi^2} \left(\frac{B_x}{B_y}\right) \left(\frac{J}{10 J_{\rm u}}\right)^2 \, , \tag{2.23}$$

where the current densities are normalized by typical current density of fully developed turbulence, $\approx 10 J_{\rm u}$, and we assume that $J_x \approx J$ because J_x dominates the total current density J.

The relationship between B_x and B_y is given from the linearized equation system, Equations (10) and (12) in Sano & Miyama (1999),

$$B_x = -\frac{2 v_{\rm Az0}^2}{\eta_{\rm lam} \Omega} B_y \, . \tag{2.24}$$

where $\eta_{\rm lam}$ is the resistivity in the laminar case, and we use the fact that the saturated state

is steady and resistivity is spatially uniform. Thus, we give B_x/B_y in the laminar state as

$$\frac{B_x}{B_y} = -\frac{4}{\beta_0}\frac{\eta_\mathrm{u}}{\eta_\mathrm{lam}} \,. \tag{2.25}$$

The saturated resistivity η_lam is given by Equation (2.20).

Using Equation (2.25) and Equation (2.20) to Equation (2.23) in the saturated state, we obtain $\alpha_\mathrm{M,lam}$ as

$$\alpha_\mathrm{M,lam} = 0.25\left(\frac{\beta_0}{10^4}\right)^{-1/2}\left(\frac{J_\mathrm{EH}}{10J_\mathrm{u}}\right)^2 \,, \tag{2.26}$$

where we assume J to be equal to J_EH. Equation (2.26) approximately equals to the fit in Figure 2.7. The difference of the coefficients between Equation (2.26) and the fit comes from the difference between the saturated current density and J_EH. Although Equation (2.26) approximately reproduces the Maxwell stress in the laminar state, it is not available for the turbulent state.

On the other hand, the fully developed turbulent state is empirically given from the data without electron heating. We find an empirical formula of $\alpha_\mathrm{M,turb}$ from Table 3,

$$\alpha_\mathrm{M,turb} \approx 0.036\left(\frac{\beta_0}{10^4}\right)^{-0.56} \,, \tag{2.27}$$

which can well reproduce α_M of the case without electron heating in calculations of this Chapter.

To well reproduce simulation results, we make a function which approaches $\alpha_\mathrm{M,\,turb}$ and $\alpha_\mathrm{M,\,lam}$ with high J_EH limit and low J_EH limit, respectively,

$$\alpha_\mathrm{M} = \left(\alpha_\mathrm{M,\,turb}^{-1/3} + \alpha_\mathrm{M,\,lam}^{-1/3}\right)^{-3} \,. \tag{2.28}$$

To verify this equation, we compare them to the results with different β_0 ($\beta_0 = 10^3, 10^4$, and 10^5) and Λ_0 ($\Lambda_0 = 30$, 10, and 1). Figure 2.12 shows α_M–J_EH relation, with varying β_0

and Λ_0, respectively. We see that Equation (2.28) well reproduce the resulting $\alpha_{\rm M}$.

We have to note that these results are based just on the simple analytic J–E' relation. In general, the saturated current density might not be equal to $J_{\rm EH}$. In that case, the saturated current density would be required to be modified instead of $J_{\rm EH}$. Moreover, the J–E' relation including the electron heating can be multivalued function of J (see Figure 4 in MO16). The electric fields may jump to the other blanch at $dJ/dE < 0$ because the electric field can vary with a much shorter timescale than the current density (see more details in OI15). In that situation, the current density may not converge on a value at the final state. This issue needs to be addressed in future calculations.

2.5 Summary and Discussion

We had investigated an effect of the electron heating on MRI, which has a potential to stabilize MRI (OI15). In this Chapter, we have performed the MHD simulation including the effect of damping a resistivity by the electron heating to numerically show the possibility and efficiency of the electron heating. We have clearly found that the electron heating suppresses the generation of the magnetic turbulence. In particular, when the electron heating effectively operates, the ordered magnetic fields make the laminar flow. The accretion stress caused by the magnetic fields is much less than the conventional turbulent stress of magnetic turbulence. We also find a clear relation between the Maxwell stress and current density. As the saturated current density is suppressed at lower and lower level by electron heating, the Maxwell stress becomes small. Additionally, we have shown the analytical expression of the laminar flow, which allows us to predict the Maxwell stress in the presence of electron heating.

The laminar flow formed by electron heating would have impacts on planetesimal formation. As we see in Figure 2.11, the vertical velocity dispersion drops when the electron

heating completely suppresses the turbulence. In the laminar flow, the turbulent diffusion in the vertical direction is no longer effective. Under the classical planetesimal formation theories, the dust sedimentation forms a dusty layer on midplane that might be gravitationally unstable (Safronov, 1972; Goldreich & Ward, 1973). The dust layer might cause the gravitational instability that forms planetesimals. This model has been focused in terms of avoiding the meter-size barrier. However, vigorous disk turbulence easily stirs up the dust layer and diffuses it. The dust layer with weak turbulence may also provide a possible place for secular gravitational instability that produces multiple ring-like structures and resulting planetesimals (Takahashi & Inutsuka, 2014, 2016; Tominaga et al., 2017). Therefore, weak disk turbulence may help the planetesimal formation. Such a dust sedimentation on midplane also help to cause the streaming instability which require high dust-to-gas mass ratio (Youdin & Goodman, 2005; Johansen & Youdin, 2007; Bai & Stone, 2010; Carrera et al., 2015). Therefore, efficient electron heating may help the formation of a dust layer and planetesimal formation. Moreover, such weak turbulent disk might explain observed disks suggested to be weak turbulence (e.g. Pinte et al., 2016; Flaherty et al., 2017).

In this Chapter, we neglect the stratified structure, non-Ohmic resistivities, and the negative slope in J–E' relation predicted by the ionization calculation. The stratified structure would affect the structure of magnetic field in the saturated state. The non-Ohmic resistivities such as Hall effect and ambipolar diffusion would affect the final structure (e.g., Bai & Stone, 2011; Kunz & Lesur, 2013; Lesur et al., 2014; Béthune et al., 2016; Bai, 2017), and therefore the importance of electron heating should be investigated with all resistivities. Moreover, the change of ionization balance by the electron heating would affect also the non-Ohmic resistivities. Although the simple analytic J–E' relation could not address how much the current density would be saturated in reality, this work have shown that current density is suppressed by electron heating and there is the relation be-

tween Maxwell stress and current density. We will address the saturated current density with the more detailed J–E' relation in future work.

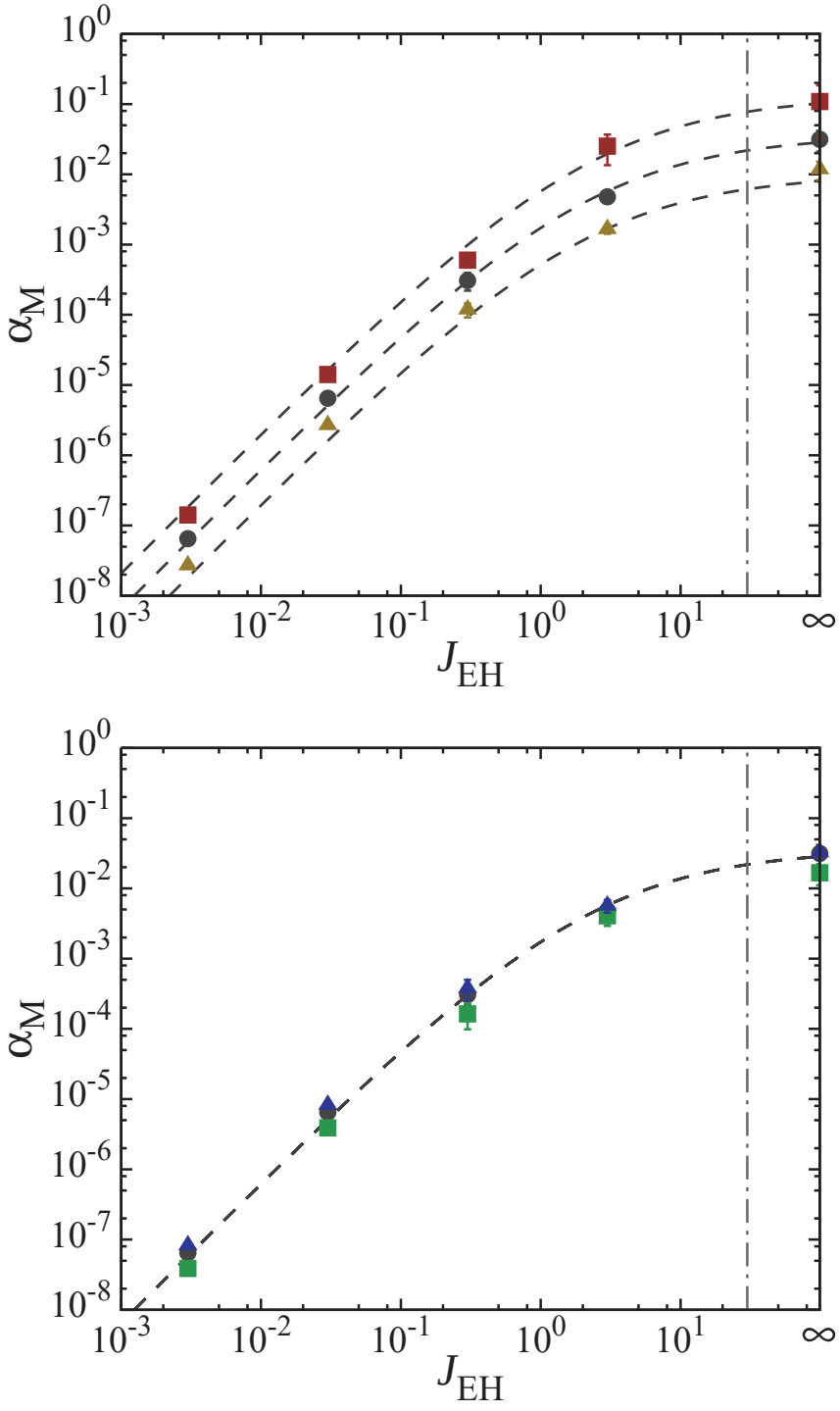

Figure 2.12 The α_M parameter as a function of J_{EH} with varying initial plasma beta β_0 (left panel) and initial Elsasser number Λ_0 (right panel). In left panel, we show results for calculations with $\beta_0 = 10^3$ (red squares), with $\beta_0 = 10^4$ (black circles), and with $\beta_0 = 10^5$ (yellow triangles). In right panel, we show results for calculations with $\Lambda_0 = 30$ (blue triangles), with $\Lambda_0 = 10$ (black circles), and with $\Lambda_0 = 1$ (green squares). The dashed lines is fit by Equation (2.28).

Chapter 3

Temperature Profile of the Inner Regions of Protoplanetary Disks

Based on Mori, Bai, & Okuzumi (2019), *"Temperature Structure in the Inner Regions of Protoplanetary Disks: Inefficient Accretion Heating Controlled by Nonideal Magnetohydrodynamics"*, DOI: 10.3847/1538-4357/ab0022.

Abstract

Gas temperature in protoplanetary disks (PPDs) is determined by a combination of irradiation heating and accretion heating, with the latter conventionally attributed to turbulent dissipation. However, recent studies have suggested that the inner disk (a few AU) is largely laminar with accretion primarily driven by magnetized disk winds, as a result of non-ideal magnetohydrodynamic (MHD) effects from weakly ionized gas, suggesting alternative heating mechanism by Joule dissipation. We perform local stratified MHD simulations including all three non-ideal MHD effects (Ohmic , Hall, and ambipolar diffusion), and investigate the role of Joule heating and the resulting disk vertical temperature profiles. We find that in the inner disk, as Ohmic and ambipolar diffusion strongly suppress electrical current around the midplane, Joule heating primarily occurs at several scale heights above the midplane, making midplane temperature much lower than that with the conventional viscous heating model. Including the Hall effect, Joule heating is enhanced/reduced when magnetic fields threading the disks are aligned/anti-aligned with the disk rotation, but is overall ineffective. Our results further suggest that the midplane temperature in inner PPDs is almost entirely determined by irradiation heating, unless viscous heating can trigger thermal ionization in the disk innermost region to self-sustain MRI turbulence.

3.1 Introduction

The temperature structure of protoplanetary disks is essential for understanding many processes of planet formation. Particularly relevant is dust composition. Outside the snow line where water condenses into ice, the dust is mainly composed of water ice and silicate (Lodders, 2003). The icy dust aggregates are more sticky (Wada et al., 2009) and are likely to directly grow to planetesimals via collisional sticking (Okuzumi et al., 2012; Kataoka et al., 2013), making the initial stage of planet formation proceed differently inside and outside of the snow line. Disk temperature structure is also important for understanding the water content of solar system bodies, since it directly reflects the water content of the accreted material, which is temperature sensitive. For instance, the Earth's ocean is only 0.023 wt% of the total Earth mass, whereas the water content of comets can be as high as 50 wt% (e.g., A'Hearn et al., 2011). Similar low water content (< 5 wt%) is inferred from the TRAPPIST-1 system (Grimm et al., 2018).

The disk temperature is determined mainly by two heating mechanisms: irradiation and accretion heating. Irradiation from the central star directly heats the surface and determines the bulk disk temperature (e.g., Kusaka et al., 1970; Chiang & Goldreich, 1997), and it generally results in a vertical temperature profile that peaks at disk surface. Accretion heating is conventionally considered to be due to viscous dissipation mediated by turbulence, a process that also drives disk accretion. It is commonly described by the Shakura-Sunyaev α-disk model (Shakura & Sunyaev, 1973), with effective viscosity ν expressed as

$$\nu = \alpha c_s H \,, \tag{3.1}$$

where c_s is the sound speed, $H = c_s/\Omega$ is the gas scale height (Ω is the Keplerian angular velocity), and the strength of viscosity/turbulence is characterized by the dimensionless parameter α. The heating rate and the viscously-driven accretion rate are then proportional

to α and density. With constant α, heating concentrates in the disk midplane, and makes disk temperature peak at the midplane. For typical PPD accretion rate of $\sim 10^{-8} M_\odot$ yr^{-1} and a conventional disk model (e.g., minimum-mass solar nebula; Weidenschilling, 1977; Hayashi, 1981), it can be found that viscous heating dominates only at sub-AU scale, beyond which the disk temperature is mainly determined by irradiation. With higher accretion rate in early phases of disk evolution, viscous heating likely dominates to larger distances, even up to a few 10s of AU during accretion outbursts (Cieza et al., 2016).

Turbulence in protoplanetary disks is thought to be generated mainly by the magnetorotational instability (MRI; Balbus & Hawley, 1991). It occurs when the magnetic field coupled with the ionized gas is stretched by shear and rotation, and can generate strong magnetic turbulence with $\alpha \sim 10^{-3}$–10^{-2} when the gas is well ionized (e.g., Hirose et al., 2006; Flaig et al., 2010). However, PPDs are extremely weakly ionized, and the coupling between gas and magnetic fields is substantially weakened by three non-ideal MHD effects, i.e. Ohmic diffusion, the Hall effect, and ambipolar diffusion (e.g., Wardle, 2007; Bai, 2011). Ohmic diffusion tends to dominate in regions where the gas density is high and the magnetic field is weak. Ambipolar diffusion tends to be important in low-density regions and relatively strong magnetic field. The Hall-dominated regime lies in between. In the inner disks, it turns out that Ohmic, Hall and ambipolar diffusion dominates in the midplane, intermediate and surface layers, respectively, and all these effects strongly affect the properties of the MRI (e.g., Jin, 1996; Wardle, 1999; Balbus & Terquem, 2001; Desch, 2004; Kunz & Balbus, 2004).

Combined with the ionization conditions in PPDs, it is well known that in the inner PPD, Ohmic resistivity stabilizes the MRI around the midplane (e.g., Gammie, 1996; Sano et al., 2000; Fleming & Stone, 2003; Dzyurkevich et al., 2013). Without including other non-ideal MHD effects, the vigorous MRI turbulence is present only in the surface layer, leading to the picture of layered accretion. The resulting vertical temperature profile was

investigated by Hirose & Turner (2011), who found lower midplane temperatures than viscous models with a constant α parameter. This is because the heating by turbulent dissipation peaks at disk surface and is lost more directly by radiation cooling instead of heating the midplane.

In the recent years, however, it has been realized that ambipolar diffusion can stabilize the MRI in the upper layer of inner PPDs (e.g., Bai & Stone, 2011; Gressel et al., 2015; Bai & Stone, 2013; Bai, 2013). With MRI fully suppressed, disk accretion and evolution is driven by magnetized disk wind (e.g., Bai, 2017). whereas the non-dissipative Hall effect has more subtle behaviors that depend on the polarity of the net vertical field threading the disk (e.g., Sano & Stone, 2002a,b; Kunz, 2008; Lesur et al., 2014; Bai, 2014, 2015; Tsukamoto et al., 2015; Simon et al., 2015; Bai & Stone, 2017; Bai, 2017).

In a largely laminar disk, accretion heating profile is then primarily determined by magnetic diffusivity instead of the turbulent viscosity. This heating mechanism is fundamentally different from viscous dissipation: there is no simple relation between heating rate and wind-driven accretion rate. The heating rate is merely related to the vertical profile of magnetic diffusivities and electric current. Therefore, detailed disk microphysics is essential to properly calculate the Joule heating rate. Furthermore, the presence of the Hall effect can amplify or reduce horizontal magnetic field depending on polarity (Lesur et al., 2014; Bai, 2014, 2015; Simon et al., 2015), and is expected to yield different temperature profiles.

In this Chapter, we study the rate of Joule heating in the inner PPDs by means of local non-ideal MHD simulations that incorporate all three non-ideal MHD effects, calculate the resulting vertical temperature profiles, and discuss their physical implications on planet formation. The plan of this Chapter is as follows. In Section 3.2, we describe our simulation setup and model parameters. In Section 3.3, we present the results of our simulations for a fiducial set of parameters, focusing on the energy dissipation and tem-

perature profiles. A parameter study is presented in Section 3.4, investigating when and how the accretion heating is inefficient. Limitations of our local simulations and implications on the planet formation are discussed in Section 3.5 before we summarize in Section 3.6.

3.2 Methods and Model

3.2.1 Numerical Method

We perform MHD simulations in a local shearing box (Goldreich & Lynden-Bell, 1965; Hawley et al., 1995) using Athena (Stone et al., 2008), an open source MHD code based on the Godunov method with constrained transport to preserve the divergence-free condition of magnetic fields. A shearing box is centered on a fixed radius R_0 and works in a frame that is corotating with its Kepler angular velocity Ω. By ignoring disk curvature, one employs cartesian coordinates (x, y, z) for the radial, azimuthal and vertical dimensions. The orbital advection scheme (Masset, 2000) described in Stone & Gardiner (2010) is used, where the velocity is decomposed into the background Kepler velocity $\boldsymbol{v}_{\rm K} = -(3/2)\Omega x\hat{\boldsymbol{y}}$ and deviation from it, $\boldsymbol{v}$. We take into account all three non-ideal MHD effects: Ohmic diffusion, the Hall effect, and ambipolar diffusion, which are characterized by diffusion coefficients $\eta_{\rm O}, \eta_{\rm H}$, and $\eta_{\rm A}$, respectively. We solve the following basic equations,

$$\frac{\partial \rho}{\partial t} + v_{\rm K}\frac{\partial \rho}{\partial y} + \nabla\cdot(\rho\boldsymbol{v}) = 0, \tag{3.2}$$

$$\frac{\partial \rho\boldsymbol{v}}{\partial t} + v_{\rm K}\frac{\partial \rho\boldsymbol{v}}{\partial y} + \nabla\cdot\left(\rho\boldsymbol{v}\boldsymbol{v} - \frac{\boldsymbol{B}\boldsymbol{B}}{4\pi} + \left(P + \frac{B^2}{8\pi}\right)\mathsf{I}\right) = 2\Omega\rho v_y\hat{\boldsymbol{x}} - \frac{1}{2}\Omega\rho v_x\hat{\boldsymbol{y}} - \rho\Omega^2\boldsymbol{z}, \tag{3.3}$$

$$\frac{\partial \boldsymbol{B}}{\partial t} = \nabla \times ((\boldsymbol{v}_{\rm K} + \boldsymbol{v}) \times \boldsymbol{B} - c\boldsymbol{E}'), \tag{3.4}$$

where ρ is the gas density, $\boldsymbol{B}$ is the magnetic field, I is the identity tensor, P is the gas pressure, c is the speed of light, and $\boldsymbol{E}'$ is the electric field as measured in the frame comoving with the neutral gas. The generalized Ohm's law relates $\boldsymbol{E}'$ to the current density $\boldsymbol{J} = (c/4\pi)\nabla \times \boldsymbol{B}$ as

$$\boldsymbol{E}' = \frac{4\pi}{c^2}(\eta_{\rm O}\boldsymbol{J} + \eta_{\rm H}\boldsymbol{J} \times \hat{\boldsymbol{B}} + \eta_{\rm A}\boldsymbol{J}_\perp), \tag{3.5}$$

where $\hat{\boldsymbol{B}}$ is the unit vector along the magnetic field and $\boldsymbol{J}_\perp = -(\boldsymbol{J} \times \hat{\boldsymbol{B}}) \times \hat{\boldsymbol{B}}$ is the current density perpendicular to the magnetic field. The sign of the vertical magnetic field is taken to be positive when its direction is the same as $\boldsymbol{\Omega}$, which is along $\boldsymbol{z}$. Note that the disk is vertically stratified by including vertical gravity $\propto -\Omega^2 z$. An isothermal equation of state is adopted, with $P = \rho c_s^2$ and c_s is the isothermal sound speed. Length scales are then measured in disk scale height $H \equiv c_s/\Omega$. We impose the shearing periodic boundary condition for x, the periodic boundary condition for y, and the outflow boundary condition for z.

Magnetic diffusivities depend on the number densities of all charge carriers. We calculate the number densities of electrons, ions and charged grains in the disk interior, by considering ionization by cosmic rays (CR), stellar X-rays, and short-lived radionuclides, and their recombination in the gas and on dust grain's surface. The ionization prescriptions are the same as those adopted in Bai (2011), where we adopt CR ionization rate profile described in Sano et al. (2000) which is based on Umebayashi & Nakano (1981), a fitting formula in Bai & Goodman (2009) for X-ray ionization with X-ray luminosity $L_X = 10^{30}$ ergs s^{-1} and X-ray temperature $T_X = 5$ keV. Ionization rate by radionuclides is taken to be constant at 7.6×10^{-19} s^{-1}. For ionization and recombination reactions, we use the same model as used in Mori & Okuzumi (2016). We represent all ion species with a single

species by following Okuzumi (2009). The diffusion coefficients are expressed in terms of the Hall parameters of individual charged species as is commonly done (e.g., Wardle, 2007; Bai, 2011). In regimes of interest (when small dust grains are scarce), the diffusion coefficients $\eta_{\rm O}, \eta_{\rm H}$, and $\eta_{\rm A}$ can be found to be proportional to B^0, B^1, and B^2 respectively, with $f_{\rm dg}(a/1\mu{\rm m})^{-2} < 1$ (Xu & Bai, 2016), where $f_{\rm dg}$ and a are the dust-to-gas mass ratio and radius of small dust grains, respectively. This condition is generally satisfied in PPDs with grain growth, and is marginally satisfied in the simulations presented in this study. A diffusivity table is then obtained by fixing grain size, dust abundance, gas temperature, expressing η_O, $Q_{\rm H} \equiv \eta_H/B$ and $Q_{\rm A} \equiv \eta_A/B^2$, as a function of gas density and ionization rate.

We also take into account the ionization by far-ultraviolet radiation (FUV) in the surface layer, where FUV can substantially enhance the level of ionization (Perez-Becker & Chiang, 2011). Similar to the treatment of Bai & Stone (2013), we impose an ionization fraction of 3×10^{-5} in the FUV layer (from which magnetic diffusivities can be calculated), with a penetration depth of 0.03 g cm^{-2} to the vertical boundary. A smooth transition is the imposed over a few grid cells to join the magnetic diffusivity of the bulk disk.

The importance of non-ideal MHD effects is characterized by Elsasser numbers, which read

$$\Lambda = \frac{v_{\rm A}^2}{\eta_{\rm O}\Omega}\,, \quad \chi = \frac{v_{\rm A}^2}{\eta_{\rm H}\Omega}\,, \quad {\rm Am} = \frac{v_{\rm A}^2}{\eta_{\rm A}\Omega}\,, \tag{3.6}$$

where $v_{\rm A} = B/\sqrt{4\pi\rho}$ is the Alfvén speed. Non-ideal MHD effects are considered strong when the Elsasser numbers are around or below unity.

A mass outflow from vertical boundaries is naturally produced in our simulations that can reduce the total mass in the simulation box. To facilitate our analysis, we add mass to the system at each time step to keep this total mass unchanged to achieve steady state over

Table 3.1 Summary of the parameters

Parameter	Values	Description
r [AU]	[0.2, 0.5, 1*, 2]	Distance from the central star
Σ_0 [g cm^{-2}]	[170, 1700*, 17000]	Surface density at 1 AU
$f_{\rm dg}$	[10^{-3}, 10^{-4}*,10^{-5}]	Dust-to-gas mass ratio
β_0	[10^3, 10^4, 10^5*, 10^6]	Initial gas-to-magnetic pressure ratio at the midplane
sgn (B_z)	[+1*, −1]	Alignment of the initial field with the rotation axis

* Fiducial value

long timescales. This treatment has a negligible effect on the overall dynamics.

Finally, although we aim to study the vertical temperature in disks, we still assume an isothermal equation of state in the simulations for simplicity. This is because ionization-recombination chemistry typically depends weakly on disk temperature, allowing us to reconstruct the temperature profile from the energy dissipation profile in an isothermal simulation, expecting that the dynamics is not to be strongly affected under the updated temperature profiles. In the mean time, we also perform the simulations with different isothermal temperatures in Section 3.5.2 to assess the validity of this approach.

3.2.2 Simulation Setup

Following Bai (2013) and Bai (2014), all our simulations are quasi-1D by using a computational domain size of $(L_x, L_y, L_z) = (0.48H, 0.48H, 16H)$ with a computational grid of $4 \times 4 \times 192$ cells. This is because the flow in the inner regions is expected to be largely laminar.

The initial gas density profile is taken to be a Gaussian $\rho = \rho_0 \exp(-z^2/(2H^2))$, where ρ_0 is the initial gas density at the midplane, with initial perturbations. The amplitudes of the initial density perturbations and velocity perturbations are 1% and 0.4% of the background values, respectively. We set a density floor of $10^{-8}\rho_0$.

The initial magnetic field configuration is given by the sum of a uniform vertical field and sinusoidal components, $\boldsymbol{B}_0 = (0, B_0/\sqrt{2}\sin(\pi z/L_z), B_0)$. The background field strength B_0 is characterized by the midplane plasma beta $\beta_0 = 8\pi\rho_0 c_s^2/B_0^2$ (the ratio of the gas pressure $P_0 = \rho_0 c_s^2$ to the magnetic pressure at the midplane). The sign of this background vertical field can be either positive or negative, whose dynamics will be different due to the Hall effect. The sinusoidal toroidal field is included to help poloidal field grow into a physical field geometry (discussed in Section 3.5.1), where the field lines at upper and lower disk surface are in the opposite directions. We have confirmed that the sinusoidal component does not affect the final state.

In code units, we adopt $H = c_s = \Omega = 1$, and $\rho_0 = 1$. For magnetic field, factors of $\sqrt{4\pi}$ are further absorbed so that magnetic pressure is simply given by $B^2/2$ (as opposed to the equations we have written which are in cgs/Gauss units).

The magnetic diffusivities in the midplane region can become excessively large due to the extremely weak level of ionization, causing excessively small simulation timesteps. To alleviate the issue, we impose a diffusivity cap $\eta_{\rm cap}$ so that when the sum of all diffusivity coefficients exceeds the cap, each of them is reduced by the same factor so that its sum just reaches $\eta_{\rm cap}$. In practice, we choose $\eta_{\rm cap} = 200 c_s H$. Note that this is much larger than the value of $10 c_s H$ that is more commonly adopted (e.g., Bai & Stone, 2013; Gressel et al., 2015). Here, we choose a higher value for $\eta_{\rm cap}$ because we have found that convergence of main diagnostic quantities for our purposes (e.g., work done by shear) converge for $\eta_{\rm cap} \geq 100 c_s H$.

3.2.3 Simulation Parameters

The parameters adopted in our simulations are summarized in Table 3.1. Our fiducial model assumes the minimum-mass solar nebula (MMSN) model (Weidenschilling, 1977;

Hayashi, 1981) at 1 AU containing 0.1 μm-sized dust grains with the dust-to-gas ratio $f_{\rm dg}$ of 10^{-4} and the initial midplane plasma beta β_0 of 10^5. We take the fiducial value of $f_{\rm dg}$ to be lower than the interstellar value ≈ 0.01 considering the situation where most submicron-sized grains have already been incorporated into larger solid particles/bodies. As shown by Ormel & Okuzumi (2013), a reduction of $f_{\rm dg}$ by a factor of 10^2–10^3 from the interstellar value best represents this situation (see also Birnstiel et al., 2011). The surface density profile is given by $\Sigma = 1700(r/\,\mathrm{AU})^{-3/2}$ g cm^{-2}. The temperature profile of the bulk disk is set to $T = 110(r/\,\mathrm{AU})^{-3/7}$ K, following Chiang & Goldreich (1997) corresponding to a disk temperature set by stellar irradiation (the model is described in Section 3.3.2). This fiducial parameter set will produce the accretion rate of $\sim 10^{-8} M_\odot$ yr^{-1} (e.g., Bai, 2014), which corresponds to PPDs around typical T Tauri stars.

The parameter sets represent inner regions (r =0.2–5 AU) of young PPDs with a grain abundance corresponding to some level of grain growth. We vary the initial midplane plasma beta β_0 from 10^3 to 10^6, with the sign of net vertical field taken to be either positive or negative.

3.2.4 Energy Equations

Upon achieving a steady state in our isothermal simulations, we will need to analyze the energy transport in the system. In doing so, we separate total energy density $E_{\rm tot}$ into internal energy density $E_{\rm int}$, and mechanical energy density $E_{\rm mec} = \rho v^2/2 + \rho\Omega^2 z^2/2 + B^2/(8\pi)$. Note that here the velocity v already has Keplerian shear subtracted. As we adopt an isothermal equation of state where $E_{\rm int}$ does not enter self-consistently, we first focus on the equation for mechanical energy to discuss its energy balance and dissipation profiles, and then we discuss how we reconstruct the more realistic temperature profiles from the post-process simulation data.

Dissipation Profiles

In a shearing-box, the equation of mechanical energy conservation is given by (e.g., Balbus & Hawley, 1998; Stone & Gardiner, 2010)

$$\begin{aligned}&\frac{\partial E_{\rm mec}}{\partial t} + v_{\rm K}\frac{\partial E_{\rm mec}}{\partial y} + \nabla\cdot\boldsymbol{F}_{\rm mec}\\ &= -q_{\rm Joule} + P\nabla\cdot\boldsymbol{v} + w_{\rm str}\end{aligned} \tag{3.7}$$

where

$$\boldsymbol{F}_{\rm mec} = \boldsymbol{v}\left(\frac{1}{2}\rho v^2 + P + \frac{1}{2}\rho\Omega^2 z^2\right) + \frac{B^2\boldsymbol{v}}{4\pi} - \frac{(\boldsymbol{v}\cdot\boldsymbol{B})\boldsymbol{B}}{4\pi} + \frac{c}{4\pi}\boldsymbol{E}'\times\boldsymbol{B} \tag{3.8}$$

$$q_{\rm Joule} \equiv \boldsymbol{J}\cdot\boldsymbol{E}'/c\,, \qquad w_{\rm str} \equiv \frac{3}{2}\Omega\left(\rho v_x v_y - \frac{B_x B_y}{4\pi}\right)\,. \tag{3.9}$$

Here, $\boldsymbol{F}_{\rm mec}$ is the energy flux of mechanical energy, which consists of hydrodynamic (first three) and magnetic (last three) terms, respectively. The last term of $\boldsymbol{F}_{\rm mec}$, $(c/4\pi)\boldsymbol{E}'\times\boldsymbol{B} = (\eta_{\rm O}+\eta_{\rm A})\boldsymbol{J}\times\boldsymbol{B} - \eta_{\rm H}B\boldsymbol{J}_\perp$, represents the Poynting flux of non-ideal MHD effects. The term $P\nabla\cdot\boldsymbol{v}$ represents the mechanical work (PdV work) done on the fluid. The term $q_{\rm Joule}$ represents irreversible energy dissipation by Joule heating, with the minus sign before $q_{\rm Joule}$ in Equation (3.8) meaning that this dissipation comes at the cost of mechanical energy. Of the three non-ideal MHD effects, only Ohmic and ambipolar diffusion generate heat, whereas the Hall effect is dissipationless: substituting Equation (3.5) into $q_{\rm Joule}$ gives $q_{\rm Joule} = (4\pi/c^2)(\eta_{\rm O}\boldsymbol{J}^2 + \eta_{\rm A}\boldsymbol{J}_\perp^2)$. The term $w_{\rm str}$ represents the work done by the Reynolds and Maxwell stresses through shear, which injects mechanical energy into the system.

In our simulations, there is energy loss through the vertical boundary through a disk wind. Globally, the energy balance thus involves energy injection by $w_{\rm str}$, which is then consumed by 1). Joule dissipation and 2). energy loss through PdV work and disk out-

flow. We emphasize that in the conventional scenario of viscously-driven accretion, the injected energy $w_{\rm str}$ (i.e., now being the viscous stress) is locally dissipated. However, this no longer holds in the case of wind-driven accretion. A more detailed discussion is presented in Appendix 3.8.

Temperature Profiles

We here use the energy dissipation profile obtained from the simulation to estimate the temperature profile. Hubeny (1990) derived the analytical formula of the temperature profile in the accretion disk with a viscosity profile. We here extend the formula by taking into account of the following points.

First, Hubeny (1990) assumed that the dissipated energy equals to the work done by the viscous stress. However, the rate profiles of the injected and dissipated energy are different, as we have discussed above. Second, heating by stellar irradiation is known to be important in PPDs, with heating rate denoted by $q_{\rm irr}$. Thus, we solve radiative transfer assuming that the net heating rate per unit volume, q, is given by the sum $q \equiv q_{\rm Joule} + q_{\rm irr}$. In addition, the dissipation profile $q_{\rm Joule}$ can be asymmetric about the disk midplane, thus we do not assume reflection symmetry of the q profile about the midplane as used in Hubeny (1990).

The derivation and further discussion are described in Appendix 3.7, and the resulting temperature profile is given by

$$T(z) = \left(\frac{3\mathcal{F}_{+\infty}}{4\sigma}\right)^{1/4} \left(\tau_{\rm eff} + \frac{1}{\sqrt{3}} + \frac{q}{3\rho\kappa_{\rm R}\mathcal{F}_{+\infty}}\right)^{1/4} , \tag{3.10}$$

where

$$\tau_{\rm eff}(z) = \frac{1}{\mathcal{F}_{+\infty}} \int_z^{+\infty} \rho\kappa_{\rm R}\mathcal{F}(z){\rm d}z' = \int_z^{+\infty} \rho\kappa_{\rm R}\left(1 - \frac{1}{\mathcal{F}_{+\infty}}\int_{z'}^{+\infty} q{\rm d}z''\right){\rm d}z' \ , \tag{3.11}$$

$$\mathcal{F}_{+\infty} = \frac{1}{2/\sqrt{3} + \tau_{R,\rm tot}}\left(\frac{\Gamma}{\sqrt{3}} + \int_{-\infty}^{+\infty}\rho\kappa_{\rm R}\left(\int_z^{+\infty} q{\rm d}z'\right){\rm d}z\right) \tag{3.12}$$

$$\tau_{R,\rm tot} = \int_{-\infty}^{+\infty}\rho\kappa_{\rm R}{\rm d}z \tag{3.13}$$

$$\Gamma = \int_{-\infty}^{+\infty} q{\rm d}z \ . \tag{3.14}$$

Here, $\kappa_{\rm R}$ is the Rosseland mean opacity, $\mathcal{F}_{+\infty}$ is the radiative flux at $z = +\infty$, Γ is the total heating energy rate, and σ is the Stefan-Boltzmann constant. We have also assumed that the scattering coefficient is much smaller than the absorption coefficient. The effective optical depth $\tau_{\rm eff}$ represents the radiative-flux-weighted optical depth. Its contribution to disk temperature illustrates how disk temperature is enhanced by heat accumulation in the disk, which is crucial for understanding how accretion heating increases disk temperature.

For simplicity, throughout this work, we assume constant opacity of $\kappa_{\rm R} = 5(f_{\rm dg}/0.01)\,{\rm cm^2\ g^{-1}}$, which is sufficient for the demonstrative purpose on the discussion of disk heating mechanisms.

To compare the temperature profiles from our simulations with those from the conventional models, we consider the two different heating models: an "equivalent" viscous model assuming local energy dissipation, and a conventional constant-α viscous model.

For the equivalent viscous model, the heating profile is given by

$$q_{\rm vis}(z) = -\frac{3\Omega}{2}\frac{B_x B_y}{4\pi} \ . \tag{3.15}$$

Note that only Maxwell stress is included because in a laminar disk wind, the Reynolds (hydrodynamic) stress is generally negligible and is also unrelated with dissipation. This model corresponds to the case where the work done by Maxwell stress is locally dissipated as if the system is turbulent. Comparison with this model will show the importance of heating profile in controlling disk temperature.

For the conventional constant-α model, viscosity is taken to be vertically constant given by $\nu = \alpha c_s H$, with viscous heating rate

$$q_{\rm vis}(z) = \frac{9}{4}\alpha\rho c_s^2\Omega \,. \tag{3.16}$$

The value of α is set by requiring that the resulting steady-state mass accretion rate, $\dot{M} = 3\pi\alpha\Sigma c_s H$, matches the mass accretion rate estimated from the simulations (Bai & Stone, 2013):

$$\dot{M} = \frac{2\pi}{\Omega}\int_{-z_b}^{z_b} T_{xy}{\rm d}z + \frac{8\pi}{\Omega} r \left|T_{zy}\right|_{z_b} \,, \tag{3.17}$$

where $T_{xy} = \rho v_x v_y - B_x B_y/4\pi$ and $T_{zy} = -B_z B_y/4\pi$, corresponding to contributions from radial and vertical (wind) transport of angular momentum. Here, we simply take the height of the base of the wind to be 4 H, z_b (which is close to values obtained more systematically, e.g., Bai, 2014).

3.3 Fiducial Run

We begin by discussing the results of the fiducial run. The outcome of the simulations is very similar to those presented in Bai & Stone (2013) and Bai (2014), where the system relaxes to a laminar state over a few tens of orbits.

We first briefly discuss the overall properties of the gas dynamics and magnetic field profiles in Section 3.3.1, focusing on dissipation by Joule heating. We then discuss the

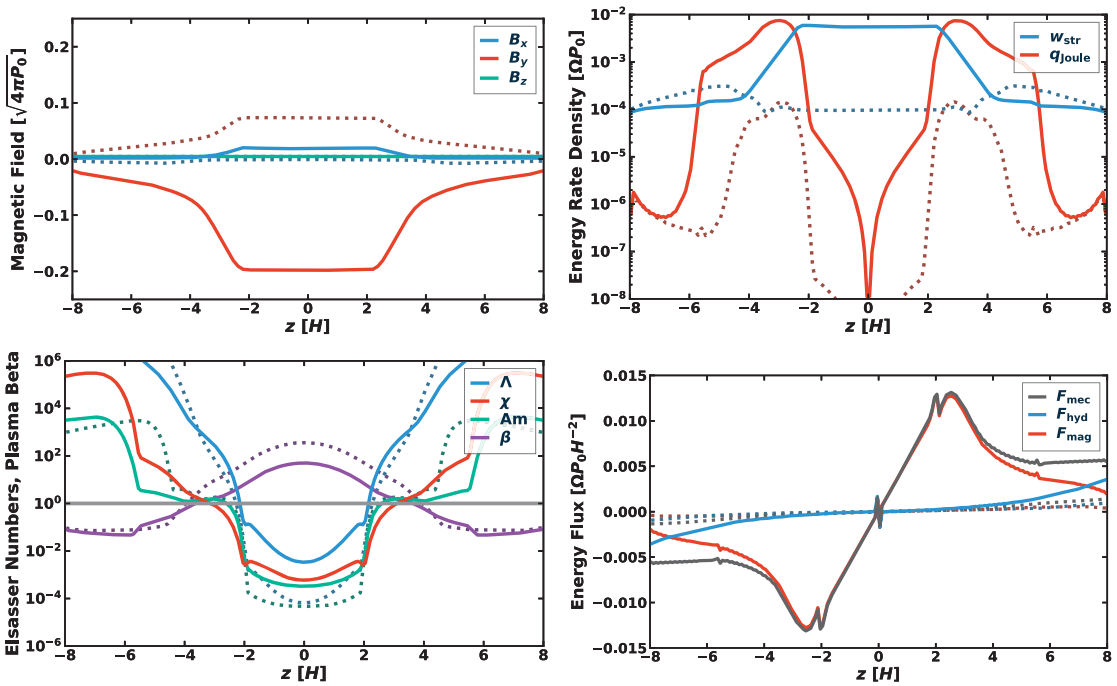

Figure 3.1 Vertical profile of magnetic fields (upper left panel), rates of energy injection and dissipation (upper right panel), the Elsasser numbers and plasma beta (lower left panel), and the energy fluxes (lower right panel). In the lower right panel, $F_{\rm hyd}$ and $F_{\rm mag}$ are the hydrodynamic and magnetic energy fluxes corresponding to the first three and last three terms, respectively, in the right-hand side of Equation (3.8). The solid lines are for the fiducial simulation with all non-ideal MHD effects turned on and with aligned vertical field geometry $B_z > 0$. The dashed lines show results from the run without the Hall effect for comparison.

temperature profiles resulting from Joule heating and irradiation.

3.3.1 Gas Dynamics and Dissipation

Figures 3.1 and 3.2 show the vertical profiles of the magnetic field, the injected and dissipated energy, the Elsasser numbers, and the energy flux, for fiducial simulations with $B_z > 0$ and $B_z < 0$, respectively. The results for the same parameter set but without the Hall effect are also shown for comparison.

The overall dynamics and magnetic field profiles are largely controlled by non-ideal MHD

effects. We see from the Elsasser number profiles in the bottom left panel of Figure 3.1 and 3.2 that all three non-ideal MHD effects are important within about $z = \pm 2H$. This results from the extremely low ionization fraction, which strongly reduces the coupling between gas and magnetic field. The lack of charge carriers also tends to yield a flat magnetic field profile (being unable to sustain current), as seen in the corresponding top left panels. As ionization level increases, non-ideal MHD effects weaken towards the surface. Moreover, as density drops, ambipolar diffusion becomes the sole dominant effect, and remains important up to $z \sim \pm 4.5H$ at the location of FUV ionization front. This is the key to MRI suppression in the disk surface (Bai & Stone, 2013). Beyond the FUV front, the gas behaves close to the ideal MHD regime and a magnetized disk wind is launched.

The Case of $B_z > 0$

We first discuss the $B_z > 0$ case. On the top left panel of Figure 3.1, we see that horizontal components of the magnetic fields around the midplane region are strongly amplified, and is also stronger than that without the Hall effect by a factor of two. This is due to the Hall-shear instability (HSI; Kunz, 2008; Lesur et al., 2014; Bai, 2014). This instability simultaneously amplifies radial and toroidal fields through shear and Hall drift, creating a strong Maxwell stress.

The profile of the magnetic field is determined by non-ideal MHD effects (amplification by HSI within $\pm 2H$ and smoothing by ambipolar diffusion) together with advection by disk winds towards the surface. The outcome is a strong vertical gradient of toroidal field B_y beyond $\pm 2H$. This gradient of B_y is primarily responsible for wind launching (Bai et al., 2016). In the mean time, it produces relatively strong current in the disk upper layers, and leads to the energy dissipation beyond $z \sim \pm 2H$. We see from the top right panel of Figure 3.1 that the energy dissipation rate peaks at $z \sim \pm 3H$. The vertically

integrated dissipation rate (Equation 3.56), in code units, is found to be $\Gamma_{\rm Joule} = 2.4\times10^{-2}$. This is a factor of 65 higher than the Hall-free case, which has less weaker toroidal field and its vertical gradient giving a value of $\Gamma_{\rm Joule} = 3.7\times10^{-4}$. These values for all parameter sets are summarized in Table 3.2.

Energy injection is dominated by the Maxwell stress, concentrated within $z \sim \pm 2H$ (as a result of the HSI) as shown on the upper right panel of Figure 3.1. The vertically integrated energy injection rate (Equation 3.55) reaches $W_{\rm str} = 3.3 \times 10^{-2}$, much higher than the Hall-free case, which gives $W_{\rm str} = 2.5 \times 10^{-3}$. From the bottom right panel of the figure, we further see that this energy is carried to upper layers first by the Poynting flux of ambipolar diffusion, $\eta_{\rm A}\boldsymbol{J}\times\boldsymbol{B}$, and then by advection through disk wind.[1]

The overall conservation of mechanical energy is achieved in the simulations. As discuss in Appendix 3.8, part of the energy injection by Maxwell stress is dissipated into $q_{\rm Joule}$, while the rest is used to drive disk winds. The division of $w_{\rm str}$ into the two parts depends on disk microphysics. Although the Hall effect does not generate the Joule heating, the HSI amplifies the magnetic field and hence enhances the Joule heating. The conversion of the work done by Maxwell stress into Joule heating reaches $\sim 71\%$ for this fiducial run, as opposed to only $\sim 15\%$ in the Hall-free run.

Finally, we comment that in this simulation, the toroidal magnetic field takes the same sign over the entire computational domain. This geometry is, however, unphysical for wind launching in a global disk (Bai & Stone, 2013). This is a main limitation of local simulations where there is no preference of being radially inward or outward. The influence of the unphysical field geometry on the temperature profile is discussed in Section 3.5.1.

[1] There are a few spikes in the energy flux profile. The spikes at the midplane are caused by a numerical error of the gravitational potential, and the ones at $z \sim \pm 2H$ are caused by switching on the diffusivity cap. These spikes are in very limited regions and do not affect the overall results.

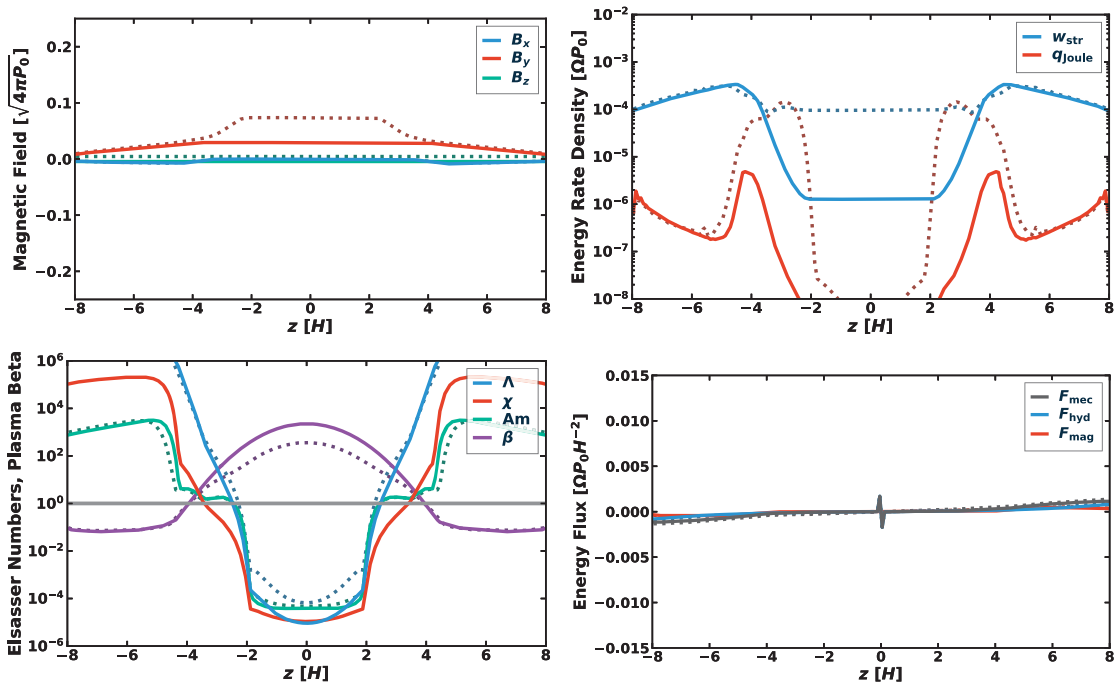

Figure 3.2 Same as Figure 3.1, but for the run with the anti-aligned vertical field geometry, $B_z < 0$.

The Case of $B_z < 0$

While the Hall effect amplifies horizontal magnetic field when $B_z > 0$, it suppresses the growth of the horizontal field when $B_z < 0$ (e.g., Bai, 2014). Figure 3.2 shows the same as Figure 3.1, but for run with $B_z < 0$. We see that horizontal magnetic field strength is maintained at a relatively low level within $\pm 4H$, as compared to the Hall-free case. Consequently, the current generated by the vertical gradient of B_y is weaker, leading to much smaller Joule heating rate even compared with the Hall-free case. As a result, Joule heating is much weaker, and we find $\Gamma_{\rm Joule}$ to be only 9.5×10^{-6}.

The work done by the Maxwell stress is also significantly lower around the midplane region within $z = \pm 2H$ (again consequence of the Hall effect suppressing horizontal field). Towards disk upper layers, as the Hall effect significantly weakens, we see that the magnetic field profiles are almost identical to the Hall-free case, which still yields consider-

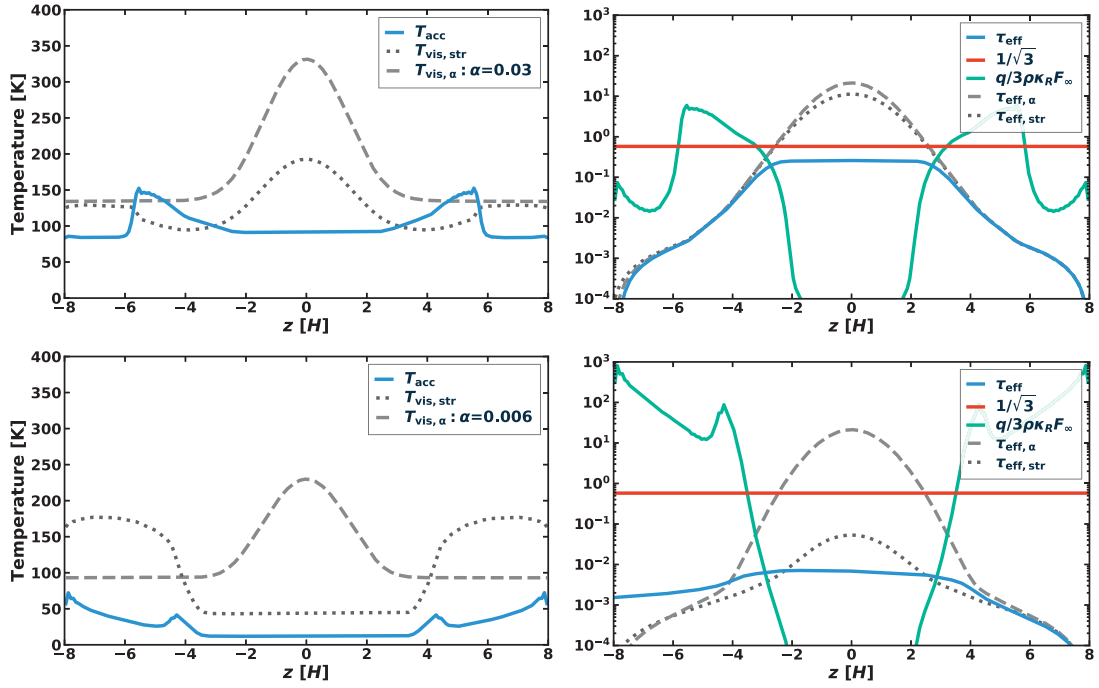

Figure 3.3 Vertical profiles of temperature (left panels) and effective optical depth (right panels) for the runs with $B_z > 0$ (upper panels) and $B_z < 0$ (lower panels). The solid line in the left panels shows the temperature profiles derived by using the Joule dissipation rate from the MHD simulations. The dotted and dashed lines show the temperature profiles derived from the "equivalent" viscous model, $T_{\rm vis,\,str}$, and the 'constant-α" model $T_{{\rm vis},\alpha}$ (see Section 3.2.4), respectively. Irradiation heating is not included. In the right panels, the blue lines are $\tau_{\rm eff}$, while the red and green lines are the second and third terms in the parentheses of Equation (3.10), respectively, which helps compare their relative importance in determining $T(z)$. The dotted and dashed lines in the right panels show the effective optical depth for the equivalent viscous model, $\tau_{\rm eff,\,str}$, and constant-α model, $\tau_{{\rm eff},\alpha}$, respectively.

able Maxwell stress, amounting to $W_{\rm str} = 1.9 \times 10^{-3}$, which is associated with the wind launching process. In other words, most of the Maxwell stress is generated to assist wind launching instead of Joule dissipation.

3.3.2 Temperature Profiles

In this subsection, we reconstruct the vertical temperature profile based on the heating rate obtained earlier.

No irradiation

First, we focus on temperature profiles determined only by the accretion heating. Without considering irradiation, the typical temperatures found in the calculations are smaller or even much smaller than the temperature assumed in our simulations. Here, we mainly focus on the comparison between different heating prescriptions (accretion heating by Joule dissipation, equivalent viscous dissipation, and constant α), and different field geometries.

Figure 3.3 shows that the temperature from the simulation and two viscous heating models for runs with the $B_z > 0$ and $B_z < 0$ cases. We also show the profile of the effective optical depth (see Equation (3.11) and right panels of Figure 3.3), which measures the optical depth above a certain height weighted by the heating profile. The effective optical depth encapsulates the crucial differences among heating profiles. With Joule heating, and for both $B_z > 0$ and $B_z < 0$ cases, since the heating occurs at $z \approx \pm 3H$ and $\pm 4H$, respectively, the effective optical depth no longer increases within a few scale heights. This yields relatively low temperature at the midplane region, and temperature peaks towards disk surface where most heating takes place. Overall, the temperature in the $B_z > 0$ case is much larger than that for $B_z < 0$, which is largely due to the different level of total Joule dissipation controlled by the Hall effect.

In the equivalent viscous model, there is strong ($B_z > 0$ case) and modest ($B_z < 0$ case) energy release in the midplane region, making the effective optical depth peaking in the midplane, together with higher midplane temperatures, especially in the $B_z > 0$ case. Temper-

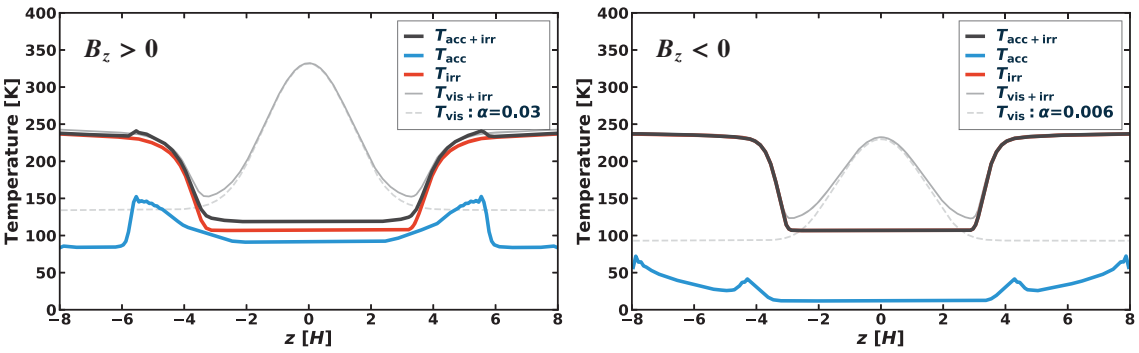

Figure 3.4 Vertical temperature profiles computed taking into account accretion heating only (blue lines), irradiation heating only (red lines), and both contributions (black lines) for the cases of $B_z > 0$ (left panel) and $B_z < 0$ (right panel). For comparison, the temperature profiles from the constant-α model with and without irradiation heating are also shown as gray solid and dashed lines, respectively.

ature increases further in the surface again due to the strong Maxwell stress there.

In the constant-α model, the total heating rate is much higher than other models, with heating profile centrally peaked. This leads to a centrally peaked temperature profile with significantly higher midplane temperature. Note that in the simulations, wind-driven accretion dominates in both $B_z > 0$ and $B_z < 0$ cases with similar total accretion rates. Therefore, in the constant-α model (with α value chosen so that the resulting viscous accretion rate matches that from the simulations), both the effective optical depth and the resulting temperature profiles are similar in the two cases. Interestingly, despite much stronger total heating rate, the constant-α model generally gives surface temperatures lower than the midplane temperature, because local heating at the surface in this model diminishes as density drops.

As constant-α models have been widely used in the literature, the dramatic difference between the resulting temperature profiles and those obtained from our simulation results demonstrate the importance of better understanding the energy dissipation in disks. Hereafter, comparisons will be made only with the constant-α model.

With irradiation

We add heating energy rate $q_{\rm irr}$ of the stellar irradiation flux into $q = q_{\rm Joule} + q_{\rm irr}$, and then calculate the temperature profile determined by both the irradiation and Joule heating in the same way as before. In doing so, we assume that the stellar irradiation and disk thermal radiation are well-separated radiation fields in wavelength, allowing us to solve them separately (Calvet et al., 1991; Guillot, 2010). The stellar irradiation flux is given by (Calvet et al., 1991)

$$\mathcal{F}_{\rm irr}(z) = -E_0\mu_0\left(\exp\left(-\frac{\tau_{\rm vi}(z)}{\mu_0}\right) + \exp\left(-\frac{\tau_{\rm vi}(-\infty) - \tau_{\rm vi}(z)}{\mu_0}\right)\right), \tag{3.18}$$

where

$$\mu_0 = r\frac{\mathrm{d}}{\mathrm{d}r}\left(\frac{H_{\rm p}}{r}\right) \tag{3.19}$$

is cosine of the angle from stellar incident flux to normal of the disk surface, R_* is the stellar radius, $H_{\rm p}$ is the height of the photosphere, E_0 is the incoming energy flux at the disk surface, and

$$\tau_{\rm vi}(z) = \int_z^{+\infty} \rho\kappa_{\rm vi}\mathrm{d}z \tag{3.20}$$

is the optical depth for visible light, where $\kappa_{\rm vi}$ is the opacity for visible light. In this thesis, we assume $\kappa_{\rm vi} = \kappa_{\rm R}$. We take R_* to be the solar radius, and $H_{\rm p}$ to be $4H$. We also take E_0 to be $L_\odot/(8\pi r^2)$, where we assume that stellar irradiation comes from one side of the star and $L_\odot$ is the solar luminosity. The rate profile of heating energy of the stellar irradiation flux is then given by

$$\begin{aligned} q_{\rm irr} &= -\frac{\partial\mathcal{F}_{\rm irr}}{\partial z} \\ &= E_0\rho\kappa_{\rm vi}\left(\exp\left(-\frac{\tau_{\rm vi}(z)}{\mu_0}\right) + \exp\left(-\frac{\tau_{\rm vi}(-\infty) - \tau_{\rm vi}(z)}{\mu_0}\right)\right). \end{aligned} \tag{3.21}$$

Figure 3.4 shows the temperature profiles taking into account the accretion heating (Joule heating), the irradiation heating, and the both. We find that for both $B_z > 0$ and $B_z < 0$ cases, the temperature profile is primarily determined by irradiation. Contribution from Joule heating is much smaller. With $B_z > 0$ where Joule dissipation is stronger, disk midplane temperature is only enhanced by a small fraction, with additional small temperature enhancement at the surface up to about 5 scale heights where Joule dissipation profile peaks. In the case of $B_z < 0$, the Joule heating is so weak that its contribution to the temperature profile is largely negligible. This is in strong contrast with the constant-α model, where the disk midplane temperature is fully dominated by viscous heating, making midplane temperature much higher.

3.4 Parameter Exploration

To further access the role of accretion heating, we conduct a parameter study in this section, where we vary the gas surface density Σ, the initial disk magnetization (characterized by β_0) and the dust-to-gas ratio $f_{\rm dg}$. The results from varying r, distance to the star, is discussed separately in Section 3.4.1. Both signs of B_z are considered in all cases. Compared with the fiducial simulations, we only vary one parameter at a time. The range of parameters are described in Table 3.1, and the results are summarized in Table 3.2.

Figure 3.5 shows how the temperature profiles depend on the gas surface density. Increasing the surface density at fixed plasma β gives higher magnetic field strength, higher mass accretion rate, associated with stronger heating. In the mean time, it gives higher optical depth, leading to more heat accumulation. On the other hand, the ionization level decreases with higher density, which reduces current and Joule dissipation.

For accretion heating from Joule dissipation, we find that while heating and the resulting temperature profile increases with increasing surface density, its overall contribution

Table 3.2 Summary of the results for all parameter sets

r [AU]	Σ [g/cm^2]	β_0	$f_{\rm dg}$	α_r	α_z	$\dot{M}_r$ [M$_\odot$/yr]	$\dot{M}_z$ [M$_\odot$/yr]	$W_{\rm str}$	$\Gamma_{\rm Joule}$	$\Gamma_{\rm acc}$	$T_{\rm acc}$ [K]	$T_{\rm vis}$ [K]	$T_{\rm irr}$ [K]
1	1700	1e5	1e-4	1.1e-2	1.6e-2	5.7e-8	8.0e-8	3.3e-2	2.4e-2	1.5e-1	91	330	105
1	1700	1e5*	1e-4	2.9e-4	7.3e-3	1.4e-9	3.6e-8	2.5e-3	3.7e-4	4.3e-2	32	239	105
1	1700	-1e5	1e-4	5.5e-5	6.4e-3	2.7e-10	3.2e-8	1.9e-3	9.5e-6	3.6e-2	12	229	105
1	17000	1e5	1e-4	4.5e-3	1.2e-2	2.3e-7	5.9e-7	1.4e-2	9.3e-3	9.3e-2	135	911	106
1	17000	-1e5	1e-4	1.2e-6	2.6e-3	6.1e-11	1.3e-7	5.5e-4	3.8e-5	1.5e-2	32	573	105
1	170	1e5	1e-4	1.8e-2	2.4e-2	9.2e-9	1.2e-8	5.4e-2	3.6e-2	2.4e-1	56	124	105
1	170	-1e5	1e-4	7.7e-4	1.2e-2	3.8e-10	6.1e-9	7.0e-3	7.2e-4	7.3e-2	20	92	105
1	17	1e5	1e-4	1.0e-2	5.4e-2	5.0e-10	2.7e-9	3.9e-2	9.9e-3	3.6e-1	23	67	106
1	17	-1e5	1e-4	6.3e-3	3.8e-3	3.2e-10	1.9e-10	6.0e-2	7.4e-3	5.7e-2	20	42	106
2.0	601	1e5	1e-4	1.2e-2	1.4e-2	4.5e-8	5.1e-8	3.5e-2	2.4e-2	1.5e-1	51	140	78
2.0	601	-1e5	1e-4	9.1e-4	2.5e-2	3.4e-9	9.3e-8	1.1e-2	4.2e-3	1.5e-1	33	140	77
0.5	4808	1e5	1e-4	1.0e-2	2.1e-2	6.7e-8	1.4e-7	3.0e-2	2.1e-2	1.7e-1	162	793	146
0.5	4808	-1e5	1e-4	3.8e-5	5.8e-3	2.5e-10	3.9e-8	1.3e-3	2.5e-5	3.3e-2	27	524	146
0.2	19007	1e5	1e-4	7.4e-3	2.9e-2	7.3e-8	2.9e-7	2.3e-2	1.5e-2	2.0e-1	340	2549	235
0.2	19007	-1e5	1e-4	1.6e-6	4.2e-3	1.6e-11	4.2e-8	5.9e-4	5.2e-5	2.4e-2	77	1492	235
1	1700	1e6	1e-4	3.6e-3	3.6e-3	1.8e-8	1.8e-8	1.0e-2	7.5e-3	4.1e-2	68	236	105
1	1700	-1e6	1e-4	5.8e-5	9.0e-4	2.9e-10	4.5e-9	9.6e-4	3.2e-5	5.4e-3	17	142	105
1	1700	1e4	1e-4	3.3e-2	7.6e-2	1.6e-7	3.8e-7	1.0e-1	6.6e-2	6.1e-1	118	465	106
1	1700	-1e4	1e-4	3.3e-4	2.2e-2	1.6e-9	1.1e-7	6.3e-3	3.9e-4	1.3e-1	30	313	105
1	1700	1e3	1e-4	8.8e-2	3.8e-1	4.4e-7	1.9e-6	3.0e-1	1.8e-1	2.6	152	670	106
1	1700	-1e3	1e-4	5.8e-3	9.0e-2	2.9e-8	4.5e-7	3.3e-2	1.7e-2	5.4e-1	77	451	105
1	1700	1e5	1e-3	4.1e-3	1.3e-2	2.0e-8	6.2e-8	1.3e-2	7.2e-3	9.4e-2	81	514	106
1	1700	-1e5	1e-3	5.4e-5	6.4e-3	2.7e-10	3.2e-8	1.9e-3	9.5e-6	3.6e-2	12	405	105
1	1700	1e5	1e-5	1.9e-2	1.8e-2	9.4e-8	9.2e-8	5.4e-2	4.1e-2	2.1e-1	97	213	105
1	1700	-1e5	1e-5	5.3e-5	6.4e-3	2.6e-10	3.2e-8	1.9e-3	9.4e-6	3.6e-2	12	138	105

* Run without Hall effect.

Note – The sign of β_0 express the sign of B_z. The accretion rates $\dot{M}_r$ and $\dot{M}_z$ are calculated by the first and second terms of Equation (3.17), respectively. The alpha value α_r and α_z are the equivalent viscous α values to yield accretion rates of $\dot{M}_r$ and $\dot{M}_z$, respectively. The energy production rate $W_{\rm str}$, $\Gamma_{\rm Joule}$, and $\Gamma_{\rm acc}$ are given by the integration of the work done by the stress $w_{\rm str}$, Joule dissipation rate $q_{\rm Joule}$, and the energy dissipation rate in the constant-α model to yield total accretion rate $\dot{M}_r + \dot{M}_z$. The temperatures $T_{\rm acc}$, $T_{\rm vis}$, and $T_{\rm irr}$ are the midplane temperatures given by the Joule heating, viscous heating of the expected mass accretion rate (from the constant-α model), and irradiation heating, respectively.

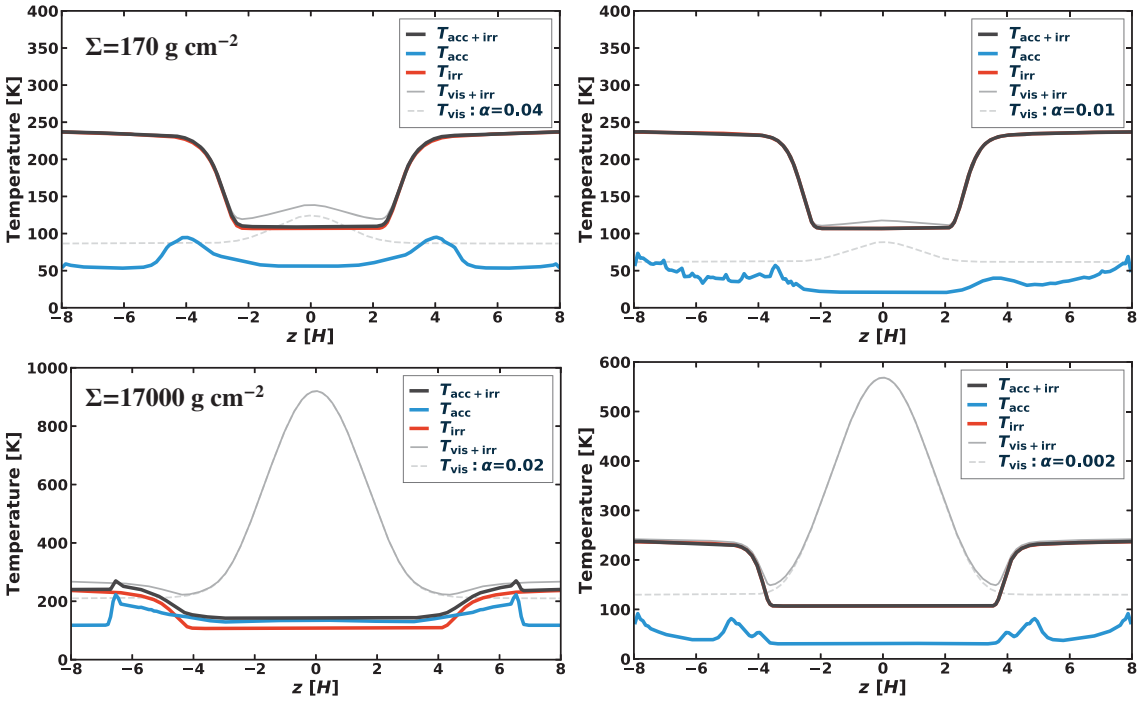

Figure 3.5 Same as Figure 3.4, but for runs with $\Sigma = 170$ (top) and 17000 g cm^{-2} (bottom) and with $B_z > 0$ (left) and $B_z < 0$ (right). Note that the scales in some figures are different.

is still relatively small compared with irradiation unless the surface density is orders of magnitude higher. Also, heating from the $B_z > 0$ case is much stronger than the $B_z < 0$ case, where Joule dissipation is almost always negligible compared to irradiation. For heating from the constant-α viscous model, higher/lower accretion rate and gas surface density (i.e., higher/lower optical depth) both yield an increase/decrease of midplane temperature, leading to large/smaller differences compared with results from the Joule heating case.

In Figure 3.6, we show results with different initial vertical magnetic field strength (characterized by β_0) in a way similar to Figure 3.5. Obviously, stronger/weaker net vertical field gives higher/lower accretion rate (largely wind-driven). We find that the variation of β_0 and does not strongly alter the location of Joule dissipation. Increasing/decreasing the field strength mainly enhances/reduces the total rate of Joule dissipation. The change

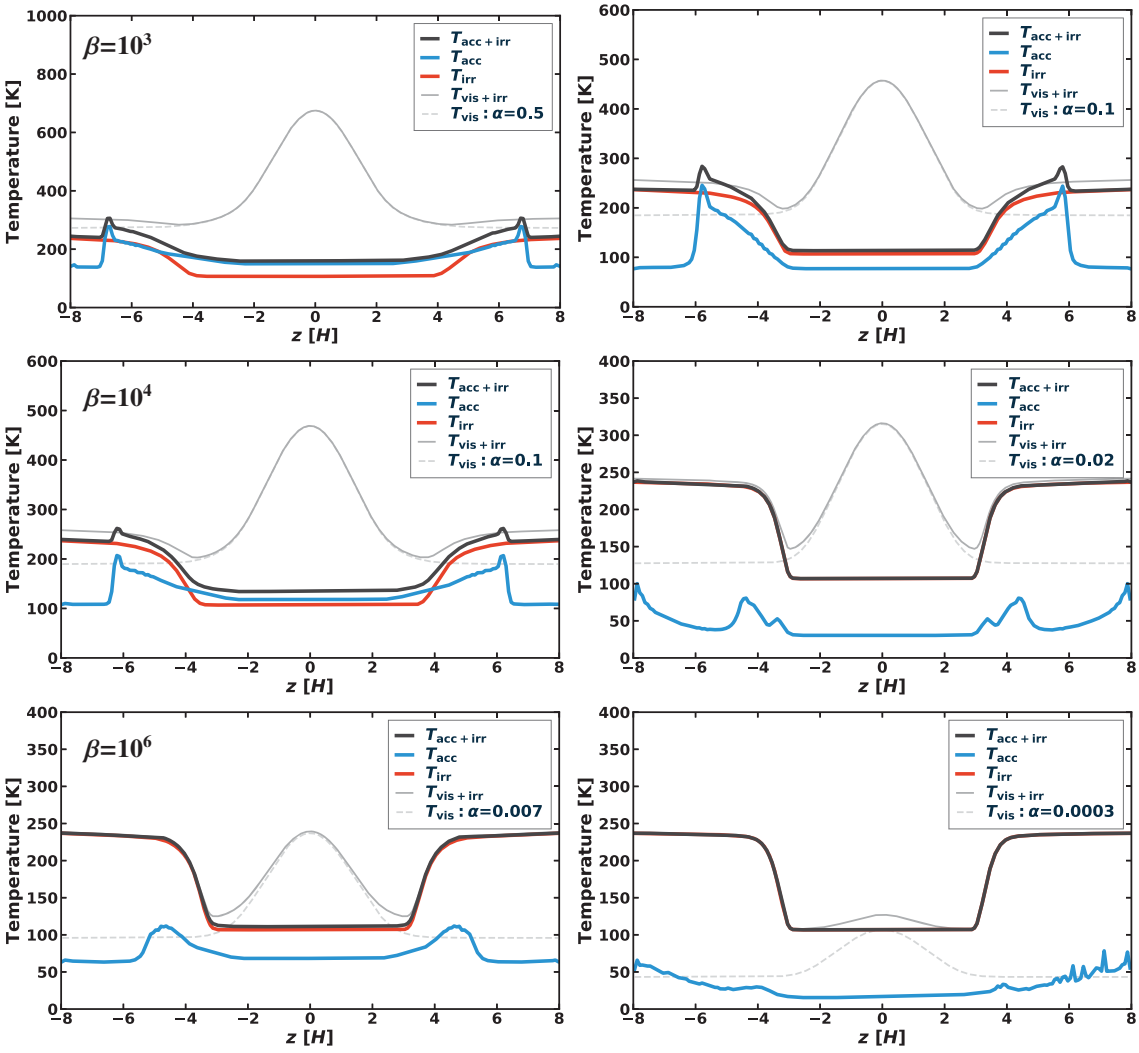

Figure 3.6 Same as Figure 3.5, but for runs with $\beta = 10^3, 10^4$, and 10^6 (from top to bottom).

in dissipation is more significant for the $B_z > 0$ case, causing appreciable changes in midplane and surface temperatures, whereas in the $B_z < 0$ case, disk temperature profile is again almost entirely determined by irradiation. In the constant-α model, again, the midplane temperature is dominated by viscous dissipation and is sensitive to changes in accretion rate.

We then discuss the dependence of dust abundance in Figure 3.7 by varying the dust-to-gas mass ratio of 10^{-3} and 10^{-5}. The dust abundance affects the ionization fraction and

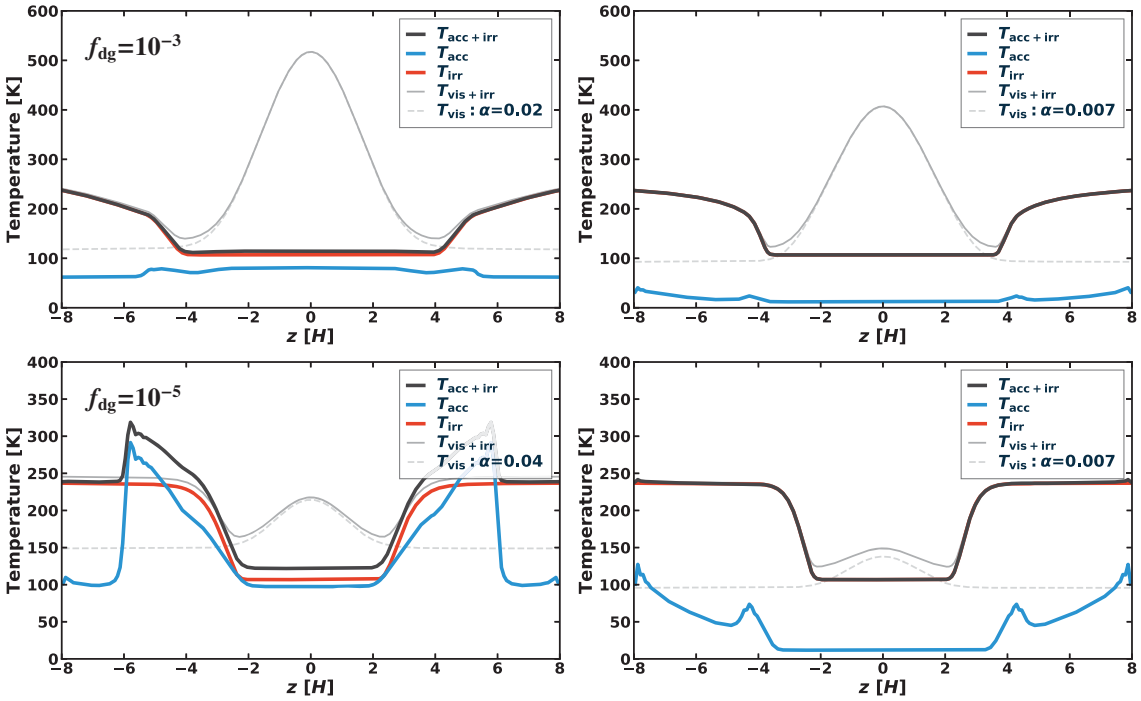

Figure 3.7 Same as Figure 3.5, but for runs with $f_{dg} = 10^{-3}$, and 10^{-5} (from top to bottom).

optical depth. Higher dust abundance leads to higher the optical depth. It makes the optically thick region more extended (as seen in the T_{irr} profile), more heat accumulation, and hence higher midplane temperature. In the mean time, it leads to lower ionization fraction. This acts to suppress field growth, making dissipation take place at higher altitude, and hence reduce the contribution from Joule heating. For lower dust abundance, lower optical depth tends to reduce midplane temperature, whereas the higher ionization fraction enhances Joule dissipation especially towards the surface (the disk remains laminar in our simulation), as well as its overall contribution to disk heating. We thus see prominent temperature bumps at disk surface in the $B_z > 0$ case. For field polarities, lower grain abundance gives higher surface temperature.

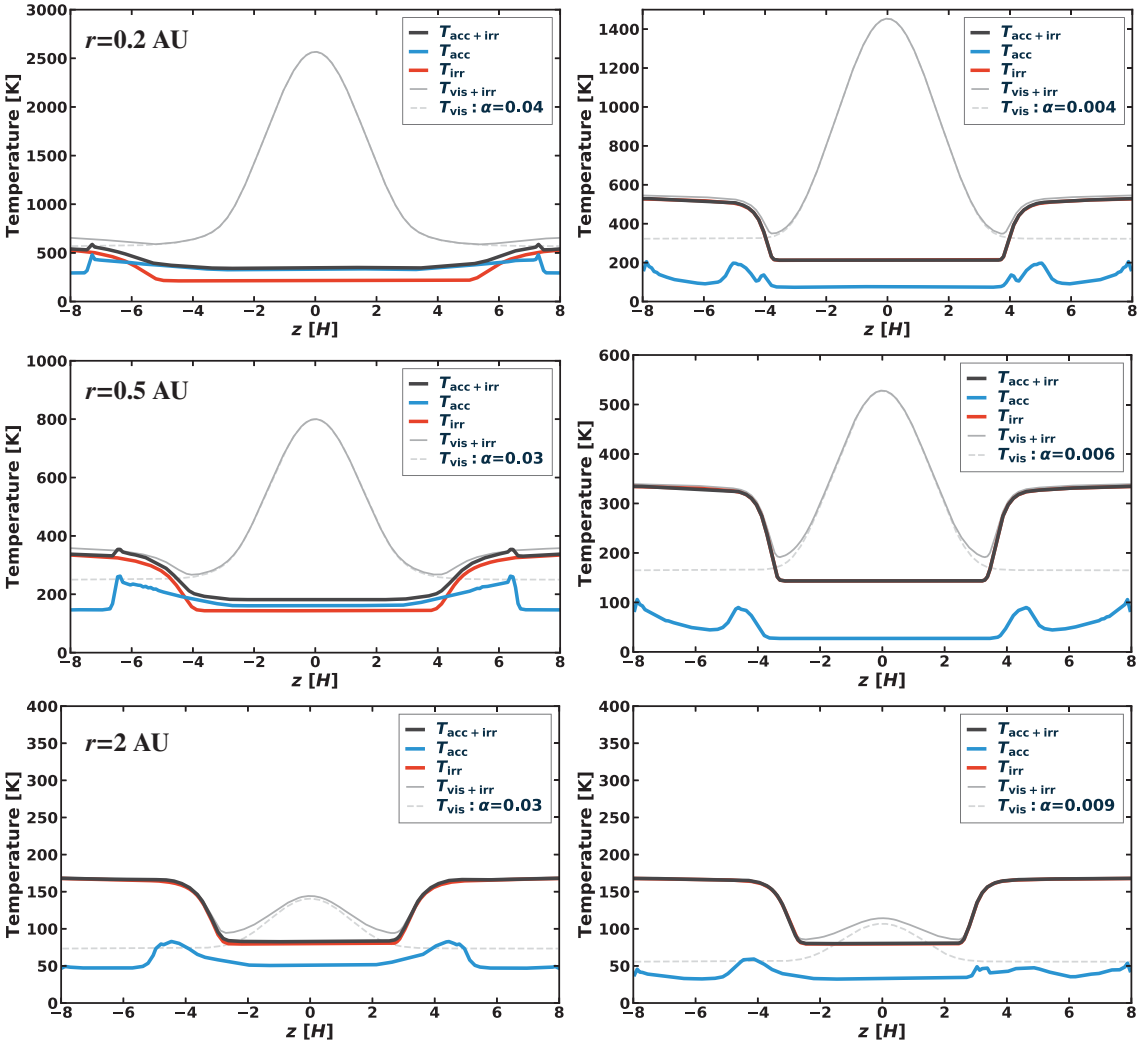

Figure 3.8 Same as Figure 3.5, but for runs with $r = 0.2, 0.5$, and 2 AU (from top to bottom).

3.4.1 Dependence on Radial Distance

In Figure 3.8, we discuss the dependence of accretion heating on the distance from the star, r. We first discuss the scenario from the conventional constant-α viscously-driven accretion model. Towards larger distance, while irradiation gets weaker, it tends to play a more dominant role because viscous heating decreases with distance even faster. This is evident in our calculations assuming viscous heating with constant α parameters. Towards smaller r, we see that within $r \lesssim 0.5$ AU, midplane temperature reaches and exceeds

$\sim$ 800K in the constant-α model, which would trigger thermal ionization of alkali species, and likely make the midplane region MRI active (Desch & Turner, 2015). This implies that MRI turbulence can be self-sustained in this region: viscous dissipation from the MRI maintains high midplane temperature needed for thermal ionization to sustain the MRI.

In the framework of our simulations (where disk temperature is fixed to irradiation temperature), the same trend holds in the case of $B_z > 0$ in the sense that the role of Joule dissipation becomes more important towards smaller distances, and start to dominate over at $r \lesssim 0.5$ AU. For the $B_z < 0$ case, however, even at a close distance of $r = 0.2$ AU, Joule dissipation is still negligible compared with irradiation heating. In both cases, the system temperature never gets close to $\sim$ 800K, the rough threshold for thermal ionization[2], and in the simulations, the systems are well in the laminar state. This means that the laminar states from our simulations are equally valid solutions, in addition to the case self-sustained MRI turbulence discussed earlier. Whether the system can stay in one case or the other then must be determined from global conditions and/or evolution history.

3.5 Discussion

3.5.1 Geometry of Magnetic Field

We have employed local shearing-box simulations to study the vertical distribution of current density. One important issue of this approach is that a horizontal current layer that accompanies a flip of the sign of the horizontal magnetic field (which is necessary for a physical field geometry in a disk wind) tends to be unstable in shearing-box simulations as pointed out by Bai & Stone (2013). They found that the natural geometry of global

[2]Note that thermal ionization of alkali species is not included in our ionization chemistry model, and it is not needed as the results show.

magnetic field in a shearing box is such that the field lines have no flip and the horizontal fields on the top and bottom sides of the box have the same direction. This tendency is also observed in our simulations: even though we start with magnetic field geometry of a flip at the midplane, the flip gradually moves toward high altitude and eventually escapes from the simulation box through the vertical boundary. The instability of the horizontal current layer seems to occur because the field lines straighten out under magnetic tension that is amplified by the Keplerian shear and the Hall effect.

In reality, the magnetic field threading a protoplanetary disk should have global geometry such that the field lines are directing outward on both side of the disk, and hence the horizontal field should have a flip at some height within the disk. Depending on its height, the current layer accompanied by this flip could contribute to the heating of the disk interior, but this cannot be evaluated in our local simulations.

Recent global simulations by Bai (2017) that include all three non-ideal MHD effects found that the flip occur naturally in global simulations. In particular, in their fiducial model with parameters similar to ours, thanks to the Hall effect, the flip occurs at very high altitude (about 4-5H above the midplane) on one side of the disk in the inner disk (a few AU). The location of the flip roughly coincides with the location of the FUV front. Because of such high altitude, magnetic field profiles in the bulk disk below the location of the flip are in fact similar to the profiles obtained in shearing-box. Therefore, on the one hand, our calculations miss additional heating resulting from the strong current layer due to the flip. On the other hand, this single-sided heating at very high altitude likely only causes very localized heating near the disk atmosphere (see Figure 3.10 in Appendix 3.7 for an example), and has very limited impact to the disk midplane temperature. Meanwhile, we plan to address this issue further with global simulations in future works.

3.5.2 Dependence on the Prior Temperature

The approach we have taken to study disk heating is not self-consistent: although the temperature profiles obtained using Equation (3.10) properly take into account Joule heating and irradiation heating, the Joule heating rates are obtained from isothermal MHD simulations. For this reason, the "posterior" temperature obtained from Equation (3.10) differs from the "prior" temperature given in the MHD simulations. Although self-consistent modeling will be the subject of our future work, it is important to clarify within the current approach how much a variation of the prior temperature can influence the resulting heating rate and posterior temperature.

For this purpose, we repeated the fiducial run but with a prior temperature of $T = 280$ K, which is approximately twice the fiducial value. This choice is motivated by the fact that for passively irradiated disks, the temperature in the optically thin surface region is about two times higher than that in the optically thick disk interior (e.g., Chiang & Goldreich, 1997). Figure 3.9 compares the vertical profiles of the stress and accretion heating rates from the fiducial runs with the two different prescribed temperatures.[3] It shows that in normalized units, the heating rate in this case reduced by a factor of two. This difference mainly comes from the temperature dependence on the diffusivities. Since the posterior temperature given by Equation (3.10) scales with the heating rate as weakly as $q^{1/4}$, a variation of the prior temperature only weakly affects the posterior temperature.

[3] In this simulation run, the signs of the horizontal fields B_x and B_y are opposite to those in the original fiducial run. However, this has no physical significance because the equations governing the local shearing box are invariant under the transformation $(x, y) \to (-x, -y)$. The polarity of the horizontal field in the saturation state is randomly determined depending on the initial perturbations.

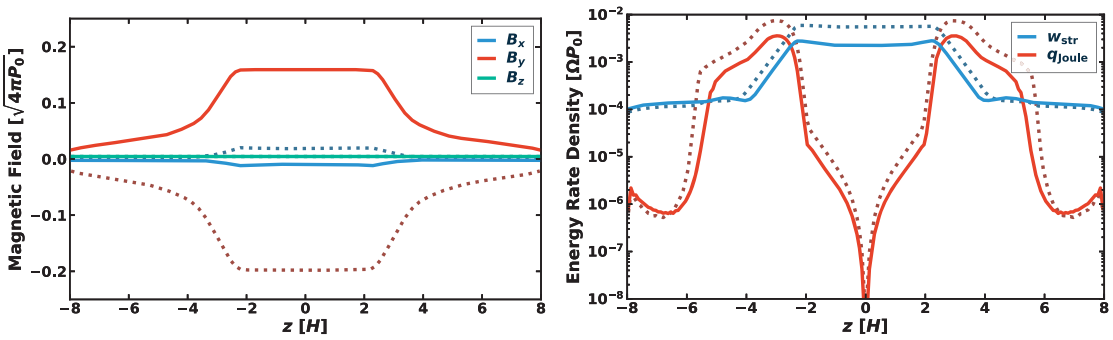

Figure 3.9 Same as the top panels of Figure 3.1, but for the run with $T = 280$ K. Dotted lines show the results of the fiducial run for comparison.

3.5.3 Impacts of Inefficient Accretion Heating on Planet Formation

Conventionally, the temperature profiles of PPDs in planet formation studies are obtained by adopting a simple viscous accretion disk model, similar to our constant-α model. In the more realistic situation of wind-driven accretion with a largely laminar disk, our results indicate that accretion heating of the disk interior is much less efficient, and viscous heating models could overestimate the temperature near the midplane, where planet formation mainly proceeds. These results could have a number of implications for planet formation.

For example, one important constraint can be derived on the formation history of the solar-system rocky planets including the Earth (Oka et al., 2011; Sato et al., 2016; Morbidelli et al., 2016). The fact that the water content of the solar-system terrestrial planets is tiny implies that they formed interior to the snow line. Constant-α disk models infer that the inner region of the solar nebula where the terrestrial planet formed retained a temperature above the sublimation point of water ice as long as the nebular accretion rate is comparable to or above the median accretion rate of classical T-Tauri stars, $10^{-8}\ M_\odot\ \mathrm{yr}^{-1}$ (Davis, 2005; Oka et al., 2011; Bitsch et al., 2015). However, in the absence of viscous heating, the nebular temperature at heliocentric radii of ≈ 1 au must have fallen below the ice sublimation point as the young Sun's luminosity decreased to the present-day

solar luminosity (Kusaka et al., 1970; Chiang & Goldreich, 1997; Turner et al., 2012) , which likely occurred in ≈ 1 Myr after Sun's formation (Turner et al., 2012; Bitsch et al., 2015). This would imply that the solar-system rocky planets either formed very early ($\lesssim 1$ Myr), or had formed closer to the sun and subsequently migrated outward to arrive at their present-day positions. The latter scenario is consistent with a recent model of rocky planet formation invoking nebular gas dispersal due to disk winds (Ogihara et al., 2017).

Another important implication is related to the fact that the inner disk region $R \lesssim 0.5$ AU may possess either a cold laminar state without thermal-ionization driven by disk winds, or a hot MRI-turbulent state with thermal ionization (see our earlier discussions on Figure 3.8). This fact suggests that the dynamics of such innermost disk regions are complex and may exhibit state transitions depending on the history of evolution. Such complex behaviors are already hinted from MHD simulations that include different levels of thermodynamics/radiative transfer and Ohmic resistivity (Faure et al., 2014, 2015; Flock et al., 2017), and may have profound implications to planet formation (e.g., Chatterjee & Tan, 2014). In addition, the rate and direction of type-I planet migration are known to sensitively depend on the thermodynamic structure of PPDs (Tanaka et al., 2002; Bitsch et al., 2015), again requiring reliable understanding of the disk heating mechanisms that we have studied.

3.5.4 On Plasma Heating by Strong Electric Fields

We have neglected change of the ionization fraction due to strong electric fields (Inutsuka & Sano, 2005; Okuzumi & Inutsuka, 2015). In the case of MRI turbulence, the electric field may heat up electrons, enhance its adsorption onto grains, reduce the ionization fraction, and in turn further damp the MRI (Okuzumi & Inutsuka, 2015; Mori & Okuzumi,

2016; Mori et al., 2017). Much stronger electric field, on the other hand, may trigger electric discharge (known as lightning), and thereby increase of the ionization level that promotes the MRI (Inutsuka & Sano, 2005; Muranushi & Inutsuka, 2009). While our simulations are laminar, the layer especially where horizontal magnetic field flips may possess substantial current density, that might make the system enter this regime of non-linear Ohm's law. This effect will be addressed in future publications.

3.5.5 Difference from Previous Study

We here stress the difference of this study from the previous study, Hirose & Turner (2011). Their simulation including Ohmic diffusion have already shown that, in the Ohmic dead zone, the viscous heating is much inefficient than the conventional viscous heating model. Our study confirms that their conclusion is valid even with the nonideal MHD effects other than Ohmic diffusion. This results seems to be natural considering that the heating in the upper layers is due to low ionization fraction of the disk interior. However, there is no necessary to do so for any parameter sets. As seen in Figure 9 in Bai (2015), the simulations including Hall effect may produce the current layer of the midplane. Also, the perturbations from the upper turbulent layer may release energy into the disk interior (Hirose & Turner, 2011).

In our simulations, ambipolar diffusion quenches the upper turbulent layer, and thereby the total heating rate is significantly less than Hirose & Turner (2011). This effect hinders the energy dissipation of turbulence around the midplane. Also, the current layers at the midplane are observed only for lower surface density case in our simulations. Furthermore, although the Hall effect amplifies the Joule heating rate for the $B_z > 0$ case, the energy eventually releases at high altitude. Thus, our simulations have also shown that the accretion heating is inefficient than the conventional model.

More importantly, we have newly shown this conclusion has a weak dependence on the disk parameters, which allow us to model the thermal structure of the disks. Furthermore, the disk wind is expected to remove significant accretion energy.

3.6 Summary and Conclusion

In this work, we have investigated the temperature profiles in the inner region of PPDs, where recent studies have suggested that the weakly ionized disks are largely laminar with accretion primarily driven by magnetized disk winds. Correspondingly, accretion heating mostly takes the form of Joule dissipation instead of viscous dissipation. To this end, we have performed quasi-1D shearing-box non-ideal MHD simulations to quantify the Joule dissipation profiles, based on which disk vertical temperature profiles are calculated. We start from analyzing accretion heating with fiducial parameters, followed by a parameter exploration. The results are summarized as follows.

- The energy dissipation due to Joule heating in PPDs is the strongest at relatively high altitudes ($z \sim 3H$), as a result of poor conductivity at disk midplane. This leads to little heat accumulation in the midplane region, and hence reduced midplane temperature.

- The Joule heating profile depends on the polarity of net vertical magnetic fields threading the disk (even though the wind stress does not), due to the Hall effect. It is enhanced in the aligned ($\boldsymbol{B}_0 \cdot \boldsymbol{\Omega} > 0$) case due to the Hall-shear instability, and is strongly reduced in the anti-aligned case.

- At a given accretion rate, Joule heating is much less efficient than viscous heating, yielding much smaller midplane temperatures especially in the inner disk regions. Varying disk surface density, radial location, magnetization and dust abundances

only weakly affect the conclusions above.

- As long as the disk remains largely laminar, Joule dissipation only plays a minor-to-modest (aligned) or even negligible (anti-aligned) role compared to stellar irradiation in determining disk temperature profiles, in standard disk models. However, an MRI-turbulent state can also be sustained in the very inner disk ($\lesssim 0.5$ AU) where viscous dissipation raises disk temperature to trigger thermal ionization.

This study shows that accretion heating in the wind-driven accretion PPDs is much weaker than commonly assumed. It also highlights the importance of stellar irradiation rather than the accretion heating in determining PPD temperatures even in the early stages of disk evolutional. More self-consistent simulations in full three dimensions are needed to better address the coupling between radiative processes and gas dynamics, which requires coupling non-ideal MHD with radiative transfer as well as non-thermal and thermal ionization physics. Meanwhile, consequences of these results to planet formation remains to be explored.

3.7 Appendix A: Temperature Structure of Reflection-Asymmetric Dissipation Profile in Disks

We here derive the analytic expressions of the temperature profile with a general dissipation profile by solving the radiative transfer equation of thermal radiation.

We extend the derivation of Hubeny (1990) by taking into account the following two effects. Hubeny (1990) assumed that the work done by the viscous stress is locally dissipated in a Keplerian disk. However, this is no longer true in the wind-driven scenario, as we see in Figure 3.1, which we now take into account. In addition, the stellar irradiation offers another heating source. Here, we use the rate profile $q(z)$, being the sum of

dissipation and irradiation heating, as the energy source term

$$q = q_{\rm Joule} + q_{\rm irr} \ . \tag{3.22}$$

We assume that the incoming radiation from irradiation and outgoing radiation by dust thermal emission are in visible and infrared, respectively. This approach allows us to separately solve the radiation fields (Calvet et al., 1991), and here we only consider radiative transfer of radiation reemitted by dust. The second assumption in Hubeny (1990) is that energy source term has reflection symmetry across the midplane. However, this no longer holds when energy dissipation occurs at one side of the disk, since the flip of the toroidal magnetic field generally occurs at one side of the disk, as seen in global non-ideal MHD simulations (e.g., Bai, 2017). Some of our simulations also show similar asymmetric structures.

We solve the radiative transfer equations of zeroth, first, and second moments of specific intensity $I(z, \mu, \nu)$ of the cosine of the incident angle μ. We define these moments as

$$\begin{pmatrix} J_\nu \\ H_\nu \\ K_\nu \end{pmatrix} \equiv \frac{1}{2} \int_{-1}^{1} I(z, \mu, \nu) \begin{pmatrix} 1 \\ \mu \\ \mu^2 \end{pmatrix} {\rm d}\mu \ . \tag{3.23}$$

In addition, we also define the frequency-integrated moments with its frequency ν in the thermal wavelength, respectively:

$$\begin{pmatrix} J_{\rm th} \\ H_{\rm th} \\ K_{\rm th} \end{pmatrix} \equiv \int_{\rm thermal} \begin{pmatrix} J_\nu \\ H_\nu \\ K_\nu \end{pmatrix} {\rm d}\nu \ . \tag{3.24}$$

The zeroth and first moments of the radiative transfer equation integrated over thermal

wavelength are written as, respectively,

$$\frac{\partial H_{\rm th}}{\partial z} = \rho\kappa_{B\rm pth}B_{\rm P} - \rho\kappa_{J\rm th}J_{\rm th} \ , \tag{3.25}$$

$$\frac{\partial K_{\rm th}}{\partial z} = -\rho\kappa_{H\rm th}H_{\rm th} \ , \tag{3.26}$$

where $\kappa_{J\rm th}$, $\kappa_{B\rm th}$, and $\kappa_{H\rm th}$ are the absorption mean opacity, Planck mean opacity, and flux mean effective opacity, respectively (Mihalas, 1978):

$$\kappa_{J\rm th} = J_{\rm th}^{-1}\int_{\rm thermal}\frac{\alpha_\nu}{\rho}J_\nu {\rm d}\nu \ , \tag{3.27}$$

$$\kappa_{B\rm th} = B_{\rm P}^{-1}\int_{\rm thermal}\frac{\alpha_\nu}{\rho}B_\nu {\rm d}\nu \ , \tag{3.28}$$

$$\kappa_{H\rm th} = H_{\rm th}^{-1}\int_{\rm thermal}\frac{\alpha_\nu+\sigma_\nu}{\rho}H_\nu {\rm d}\nu \ , \tag{3.29}$$

where α_ν and σ_ν are the coefficients of true absorption and scattering respectively, and $B_{\rm P} = \sigma T^4/\pi$ is the frequency-integrated Planck function. Here, we assume that $\kappa_{J\rm th} = \kappa_{B\rm th}$, and both of them are equal to the Rosseland mean opacity $\kappa_{\rm R}$.

The second basic equation is the energy balance between the energy absorption and the thermal radiation. The vertical gradient of the energy flux $\mathcal{F} = 4\pi H_{\rm th}$ of radiative transport is equal to the energy dissipation rate per unit volume. We also neglect the energy transport due to gas motion (e.g., advection and convection) for simplicity, which holds when such timescales are long compared to the timescale to establish thermodynamic equilibrium. Energy conservation is then expressed as

$$4\pi\frac{\partial H_{\rm th}}{\partial z} = q \ . \tag{3.30}$$

To close the radiative transfer equations, we adopt the Eddington approximation, which assumes isotropic radiation field (e.g., Mihalas, 1978; Rybicki & Lightman, 1979), and it

gives the relation

$$\frac{K_{\rm th}(z)}{J_{\rm th}(z)} = \frac{1}{3} \,. \tag{3.31}$$

In addition, for outgoing boundary conditions, we adopt the two stream approximation, where the outgoing radiation is characterized by

$$\frac{K_{\rm th}(+\infty)}{J_{\rm th}(+\infty)} = \frac{K_{\rm th}(-\infty)}{J_{\rm th}(-\infty)} = \frac{1}{3} \,, \tag{3.32}$$

$$\frac{H_{\rm th}(+\infty)}{J_{\rm th}(+\infty)} = -\frac{H_{\rm th}(-\infty)}{J_{\rm th}(-\infty)} = \frac{1}{\sqrt{3}} \,, \tag{3.33}$$

which are valid for the optically thick regions.

Using above assumptions, we integrate Equations (3.30) and (3.26) from z to $+\infty$ to obtain

$$H_{\rm th}(z) = H_{\rm th}(+\infty) - \int_z^{+\infty} \frac{q}{4\pi} {\rm d}z' \,, \tag{3.34}$$

$$K_{\rm th}(z) = K_{\rm th}(+\infty) + \int_z^{+\infty} \rho \kappa_{H{\rm th}} H_{\rm th} {\rm d}z' \,. \tag{3.35}$$

From these equations and the boundary conditions, we can calculate $H_{\rm th}(z)$ and $K_{\rm th}(z)$. Using Equations (3.31), (3.32), and (3.35), we obtain

$$J_{\rm th}(z) = J_{\rm th}(+\infty) + 3 \int_z^{+\infty} \rho \kappa_{H{\rm th}} H_{\rm th} {\rm d}z' \,. \tag{3.36}$$

Using Equations (3.25), (3.30), and (3.36), the temperature profile is expressed as

$$\frac{\sigma T^4(z)}{\pi} = \left(3 \int_z^{+\infty} \rho \kappa_{H{\rm th}} H_{\rm th} {\rm d}z' + J_{\rm th}(+\infty) \right) + \frac{1}{\rho \kappa_{\rm R}} \frac{q}{4\pi} \,, \tag{3.37}$$

where we have used $B = \sigma T^4/\pi$. Using Equation Equation (3.33), the temperature profile

is further expressed as

$$T(z) = \left(\frac{4\pi H_{\rm th}(+\infty)}{\sigma}\right)^{1/4} \left(\frac{3}{4H_{\rm th}(+\infty)} \int_z^{+\infty} \rho\kappa_{H\rm th} H_{\rm th} {\rm d}z' + \frac{\sqrt{3}}{4} + \frac{1}{4H_{\rm th}(+\infty)\rho\kappa_{\rm R}} \frac{q}{4\pi}\right)^{1/4} \quad (3.38)$$

If $H_{\rm th}(+\infty)$ is known, with $H_{\rm th}$ given by Equation (3.34), the temperature profile can be directly obtained by Equation (3.38). Using Equation (3.34), we see

$$H_{\rm th}(+\infty) - H_{\rm th}(-\infty) = \frac{\Gamma}{4\pi} , \quad (3.39)$$

where

$$\Gamma = \int_{-\infty}^{+\infty} q {\rm d}z \quad (3.40)$$

is the total heating (dissipation and irradiation) rate. When the dissipation profile is symmetric, we have $H_{\rm th}(+\infty) = -H_{\rm th}(-\infty) = \Gamma/8\pi$ and the derivation is complete. However, this does not necessarily hold without the reflection symmetry. In the general case, we substitute Equation (3.34) into Equation (3.35), and $K_{\rm th}(z)$ can be written as

$$K_{\rm th}(z) = K_{\rm th}(+\infty) + H_{\rm th}(+\infty) \int_z^{+\infty} \rho\kappa_{H\rm th} {\rm d}z' - \int_z^{+\infty} \rho\kappa_{H\rm th} \left(\int_{z'}^{+\infty} \frac{q}{4\pi} {\rm d}z''\right) {\rm d}z' . \quad (3.41)$$

Taking $z = -\infty$ in Equation (3.41), we find $H(+\infty)$ to be

$$H_{\rm th}(+\infty) = \frac{1}{\tau_{H,\rm tot}} \left(-\Delta K_{+\infty} + \int_{-\infty}^{+\infty} \rho\kappa_{H\rm th} \left(\int_{z'}^{+\infty} \frac{q}{4\pi} {\rm d}z''\right) {\rm d}z'\right) , \quad (3.42)$$

where

$$\Delta K_\infty = K_{\rm th}(+\infty) - K_{\rm th}(-\infty) , \quad (3.43)$$

$$\tau_{H,\rm tot} = \int_{-\infty}^{+\infty} \rho\kappa_{H\rm th} {\rm d}z . \quad (3.44)$$

If $\Delta K_{+\infty}$ is given, we can then obtain $H_{\rm th}(+\infty)$. Using Equations (3.32) and (3.33), the

sum of $H(+\infty)$ and $H(-\infty)$ is expressed as,

$$H_{\rm th}(+\infty) + H_{\rm th}(-\infty) = \sqrt{3}\Delta K_{\infty} \, . \tag{3.45}$$

Combining Equations (3.45) and (3.39), we eliminate $H_{\rm th}(-\infty)$ and obtain

$$\Delta K_{\infty} = \frac{1}{\sqrt{3}} \left(2H_{\rm th}(+\infty) - \frac{\Gamma}{4\pi} \right) . \tag{3.46}$$

Substituting Equation (3.46) into Equation (3.42), we obtain

$$H_{\rm th}(+\infty) = \frac{1}{\tau_{H,\rm tot} + 2/\sqrt{3}} \left(\frac{\Gamma}{4\sqrt{3}\pi} + \int_{-\infty}^{+\infty} \rho\kappa_{H\rm th} \left(\int_{z}^{+\infty} \frac{q}{4\pi} {\rm d}z' \right) {\rm d}z \right) . \tag{3.47}$$

This is the general expression for $H(+\infty)$ that allows for asymmetric heating profiles.

Knowing $H(+\infty)$, we finally derive the temperature profile. Using Equations (3.38) and (3.47), the temperature profile is derived as

$$T(z) = T_{\rm eff} \left(\frac{3}{4}\tau_{\rm eff}(z) + \frac{\sqrt{3}}{4} + \frac{q}{4\rho\kappa_{\rm R}\mathcal{F}_{+\infty}} \right)^{1/4} , \tag{3.48}$$

where we use the radiative flux at the upper surface $\mathcal{F}_{+\infty} = 4\pi H_{\rm th}(+\infty)$, and $T_{\rm eff} = (\mathcal{F}_{+\infty}/\sigma)^{1/4}$ is the effective temperature observed from the upper side, and

$$\tau_{\rm eff}(z) = \int_{z}^{+\infty} \rho\kappa_{\rm R} \left(1 - \frac{1}{\mathcal{F}_{+\infty}} \int_{z'}^{+\infty} q {\rm d}z'' \right) {\rm d}z' \, , \tag{3.49}$$

is the effective optical depth. Here, we further take $\kappa_{H\rm th} = \kappa_{B\rm th} = \kappa_R$ by assuming that the scattering coefficient is much smaller than the absorption coefficient, $\sigma_\nu/\alpha_\nu \ll 1$. The first term in Equation (3.48) expresses the effect that heat accumulation increases disk temperature. When the dissipation profile is reflection symmetric, the temperature profile reduces to that described in Hubeny (1990).

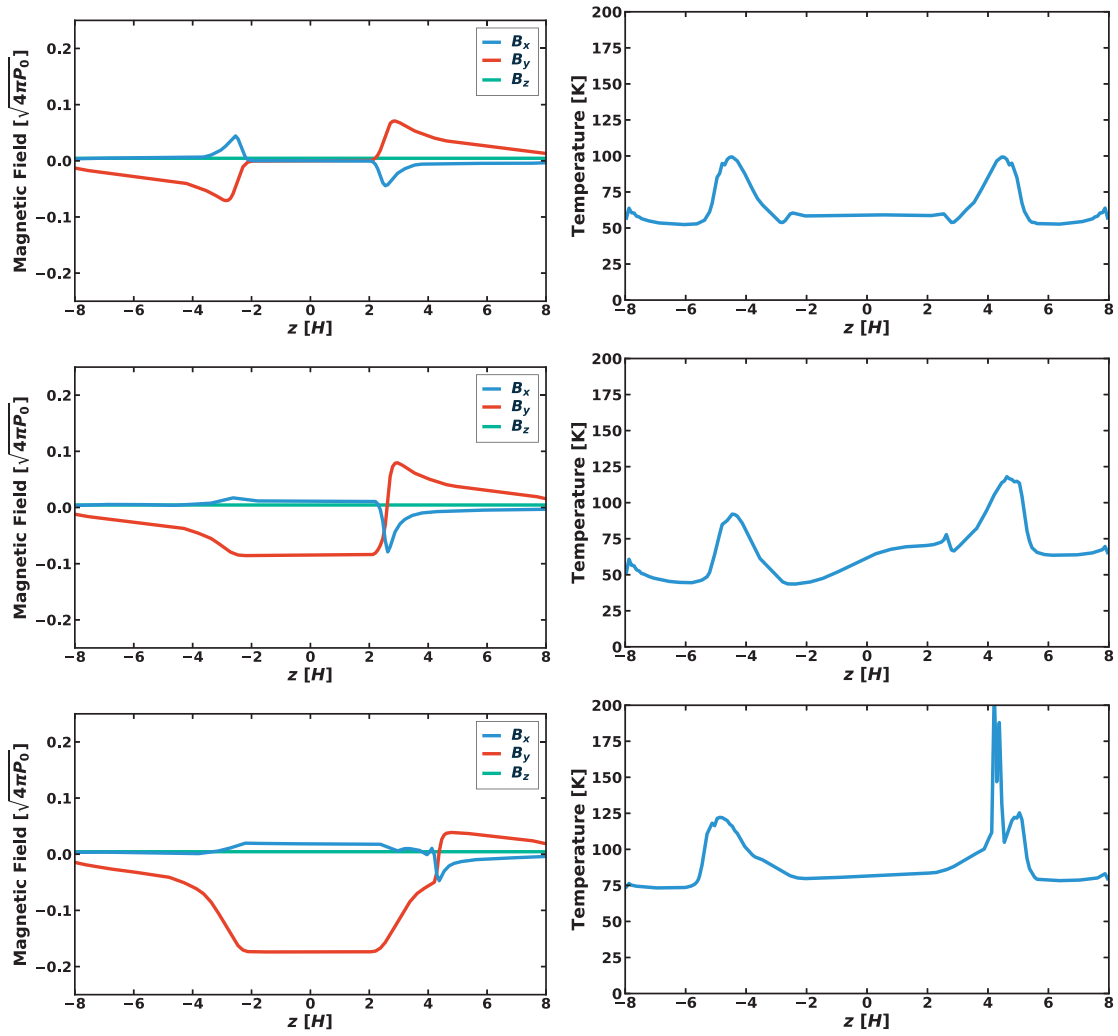

Figure 3.10 Snapshots of vertical profile of magnetic field (left) and temperature determined only by Joule heating (right) for the fiducial run at relatively early time of 4.9, 12.7, 13.9 orbits. The physical magnetic field geometry is sustained until $\sim$ 12 orbits. This field geometry is not preserved at later time as horizontal field flips to become symmetric about the midplane (due to limitation of local simulations).

We note that the definition of effective optical depth, tracking back to its original expression in Equation (3.38), represents a radiative-flux-weighted optical depth

$$\tau_{\rm eff}(z) = \frac{1}{\mathcal{F}_{+\infty}} \int_z^{+\infty} \rho \kappa_{\rm R} \mathcal{F}(z) {\rm d}z' \ . \tag{3.50}$$

To better understand its physical meaning, we consider two extreme cases. When the

all accretion energy is released at the midplane, above the midplane the radiative flux is equal to the outgoing flux $\mathcal{F}_{+\infty}$, and hence this value is equal to the standard optical depth $\tau_{R,\mathrm{tot}}/2$. In the second case, assume all accretion energy is released at a height $z = \pm z_{\mathrm{heat}}$. In the region between the heating positions above and below the midplane, the radiative flux is zero because the flux from the upper and lower sides cancels out. Correspondingly, $\tau_{\mathrm{eff}}(z)$ becomes

$$\tau_{\mathrm{eff}}(z) = \begin{cases} \tau_{\mathrm{col}}(z) & , (|z| \geqq z_{\mathrm{heat}}), \\ \tau_{\mathrm{col}}(z_{\mathrm{heat}}) & , (0 \leqq |z| < z_{\mathrm{heat}}), \end{cases} \tag{3.51}$$

where

$$\tau_{\mathrm{col}}(z) = \int_{z}^{+\infty} \rho \kappa_{\mathrm{R}} \mathrm{d}z \,. \tag{3.52}$$

Especially, the effective optical depth $\tau_{\mathrm{eff}}(z = 0)$ at the midplane is simply the optical depth at z_{heat}, which can be much smaller than the actual midplane optical depth due to the weighting. Also note that the effective optical depth can even become negative at the midplane if large energy dissipation occurs at high altitude.

Finally, we consider an example with asymmetric heating profile. In doing so, we show in Figure 3.10 snapshots of the magnetic field profiles and the temperature profile resulting from only accretion heating together for the fiducial run with $B_z > 0$ at an early evolution time of 5, 12.7, and 13.9 orbits. In this case, horizontal magnetic field flips at one side leaving a current sheet with strong dissipation.[4] We see that higher temperatures at the lower side than at the upper side, with a spike at the current sheet, with additional temperature peaks at the disk surface where vertical gradient of B_y is strong.

[4]Similar to the case discussed in Bai (2015), the system first evolves into an asymmetric profile with horizontal field flipping at a height offset from the midplane by several scale heights. This asymmetry is not long-lived owing to the limitation of local simulation, whereas it can be preserved in global simulations (Bai, 2017, see their Figure 7, and further discussions in Section 5.1).

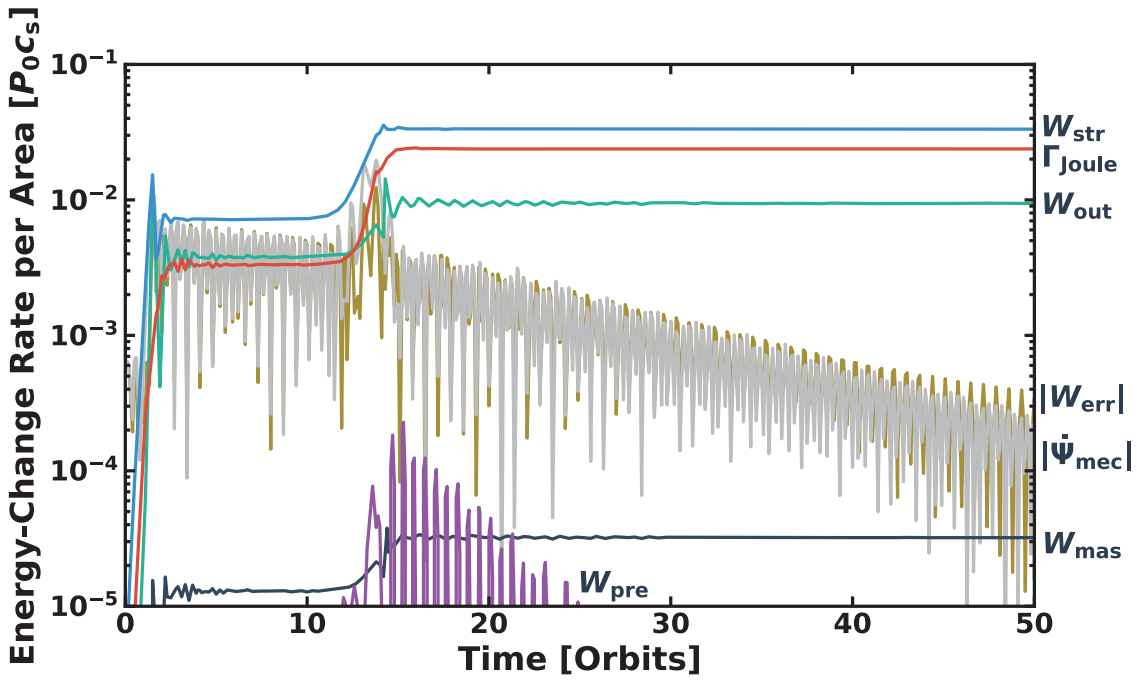

Figure 3.11 Result from the fiducial run with $B_z > 0$. Shown are the time variation of the time derivative of the total energy $\dot{\Psi}_{\rm mec}$, the rate of work done by the Reynolds and Maxwell stress $W_{\rm str}$, the rate of energy dissipation due to resistivity $\Gamma_{\rm Joule}$, the rate of energy outflow thorough vertical boundary $W_{\rm out}$, the rate of work done on the fluid by pressure $W_{\rm pre}$, the rate of additional energy due to the mass conservation $W_{\rm mas}$, and the rest of the energy rates $W_{\rm err}$ in the simulation domain, which are described in Equations (3.53)–(3.57).

3.8 Appendix B: Conservation of Mechanical Energy in the Simulations

To demonstrate energy conservation in our simulations, we first integrate Equation (3.7) over the computational domain to obtain the rate of change in the total mechanical energy per area as

$$\dot{\Psi}_{\rm mec} = \frac{1}{L_x L_y}\frac{\partial}{\partial t}\int E_{\rm mec} {\rm d}V = W_{\rm str} - W_{\rm out} - \Gamma_{\rm Joule} + W_{\rm pre}, \tag{3.53}$$

where

$$W_{\rm out} = \frac{1}{L_x L_y}\left(\int_{z=L_z/2} - \int_{z=-L_z/2}\right) F_{\rm mec} {\rm d}x{\rm d}y \tag{3.54}$$

is the rate of energy loss through the vertical boundary (by disk winds),

$$W_{\rm str} = \frac{3\Omega}{2L_y}\int_{x=L_x/2}\left(\rho v_x \delta v_y - \frac{B_x B_y}{4\pi}\right){\rm d}y{\rm d}z \tag{3.55}$$

is the rate of energy injection through the Reynolds and Maxwell stresses,

$$\Gamma_{\rm Joule} = \frac{1}{L_x L_y}\frac{1}{c}\int \boldsymbol{J}\cdot\boldsymbol{E}'{\rm d}V \tag{3.56}$$

is the rate of energy dissipation due to Joule heating, and

$$W_{\rm pre} = \frac{1}{L_x L_y}\int P\nabla\cdot\boldsymbol{v}{\rm d}V \tag{3.57}$$

is the work done on the fluid by pressure per unit time. The integrate of the second term in the left-hand-side of Equation (3.7) is eliminated because the term is a periodic quantity in the y-direction. In addition to these energy rates, we consider the other energy rates. The energy rate due to mass added for mass conservation is described by $W_{\rm mas}$. We also define the rest of the energy rates as $W_{\rm err} = \dot{\Psi}_{\rm mec} - (W_{\rm str} - W_{\rm out} - \Gamma_{\rm Joule} + W_{\rm pre} + W_{\rm mas})$.

Taking the simulation with $B_z > 0$, we show in Figure 3.11 the time evolution of each term in the equation for the mechanical energy Equation (3.53). We see that despite small oscillations (presumably due to breathing mode that is leftover from initial evolution), $W_{\rm err}$ and $\dot{\Psi}_{\rm mec}$ diminishes in time, and the system converges into a steady state which is fully laminar. It also implies time average should be performed at late times, which we choose to be between 40 and 50 orbits. Over this period, we find that about 71.4% and 28.3% of $W_{\rm str}$ is used for the energy dissipation of Joule heating and the energy outflow by the disk wind, respectively, indicating excellent level of mechanical energy conservation (note that while Athena conserves *total energy*, there can be small truncation errors in mechanical energy conservation).

Chapter 4

Discussion and Summary

In this Chapter, we summarize the updated structure of the protoplanetary disks based on the above studies in Section 4.1, and discuss the implication for the planet formation.

4.1 Expected Structures of Protoplanetary Disks

Here we summarize the progress in the structures of protoplanetary disks by our results.

4.1.1 Expected Turbulent Structure

In Chapter 2, we have seen that electron heating suppresses the MRI turbulence. From the simulation results, we have derived the analytical formula reproducing the magnetic stress. Here, we estimate the turbulence strength distribution.

The turbulence strength depends on the current density. The current density is expected to saturate at around critical diffusivity where all waves are stabilized (Equation (2.20)). Figure 4.1 (upper panel) shows the saturated current density to the current in fully developed

MRI turbulence, using a method used in Mori et al. (2017). Here, we use a minimum-mass solar nebula model, that contains 0.1 μm-sized dust with the dust-to-gas ratio of 10^{-2} and with gas-to-magnetic pressure of 10^4. For the calculation, we calculate the ionization equilibrium and the current at the critical electric fields at each radius (see Mori et al. (2017) for details). When the ratio is below $\sim 10^{-2}$, the flow becomes laminar (see Figure 2.11). In this disk model, the laminar region is small compared to the electron heating zone from 20 to 90 AU. The expected Maxwell stress is shown in lower panel of Figure 4.1. Even though the laminar region is small, the Maxwell stress is suppressed by around second order of the magnitude. Thus, we can expect that the turbulence is suppressed in the electron-heating region. Note that the electron-heating region and Maxwell stress depend on the total dust surface area per unit volume, which corresponds to the phase of the disk evolution (e.g., grain growth, and depletion of gas/dust density). In addition, the saturated current density has uncertainty, which requires further studies.

Considering the effect of the electron heating, we picture a schematic illustration of the expected turbulent structure of the disks in Figure 4.2. In the inner disk region, the MRI is suppressed by Ohmic and ambipolar diffusion, and the Hall effects amplify or decay magnetic stress in the laminar disks. Beyond and above the Ohmic dead zone, the electron heating enhances Ohmic diffusion, and hence the flow is laminar or weak turbulence. This region extends to the outer disk region. In further low-density regions, the MRI is damped by ambipolar diffusion. For the outer region of the e-heating zone, the effect suppressing MRI turbulence is similar to or weaker than ambipolar diffusion. Thus, in the region, turbulence would still exist.

Electron Heating with Non-Ideal MHD Effects

In the Chapter 2, we have considered electron heating in MRI turbulence by neglecting ambipolar diffusion and Hall effect. When we consider the ambipolar diffusion and Hall

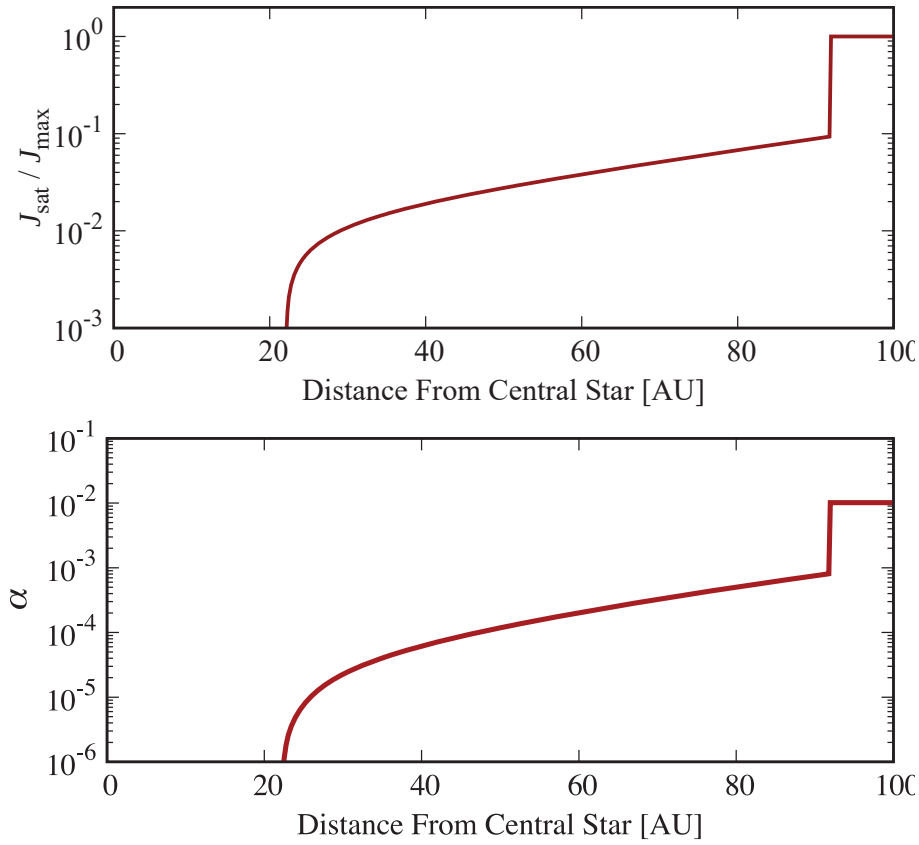

Figure 4.1 Saturated current density due to electron heating normalized by that in fully-developed MRI turbulence (upper panel) and expected Maxwell stress (lower panel), as a function of r. We use a minimum-mass-solar-nebula model, the grain size of 0.1 μm, the dust-to-gas ratio of 10^{-2}, and gas-to-magnetic pressure ratio of 10^4.

effect, the expected structure will be different. When the ambipolar diffusion suppresses the MRI turbulence, electron heating unlikely occurs in the MRI turbulence. However, instead of MRI turbulence, the Hall shear instability may cause the electron heating in the inner disk region. The Hall shear instability amplifies the toroidal magnetic fields which generate strong current. Okuzumi et al. (in prep.) studied the effects of plasma heating on all nonideal MHD effects, expanding Okuzumi & Inutsuka (2015). They suggested that the current generated by Hall shear instability may cause the electron heating inside $r \sim 1$ AU. If the electron heating occurs, it reduces electron abundance and may enhance the all nonideal MHD effects. In addition, electron heating potentially causes electrical

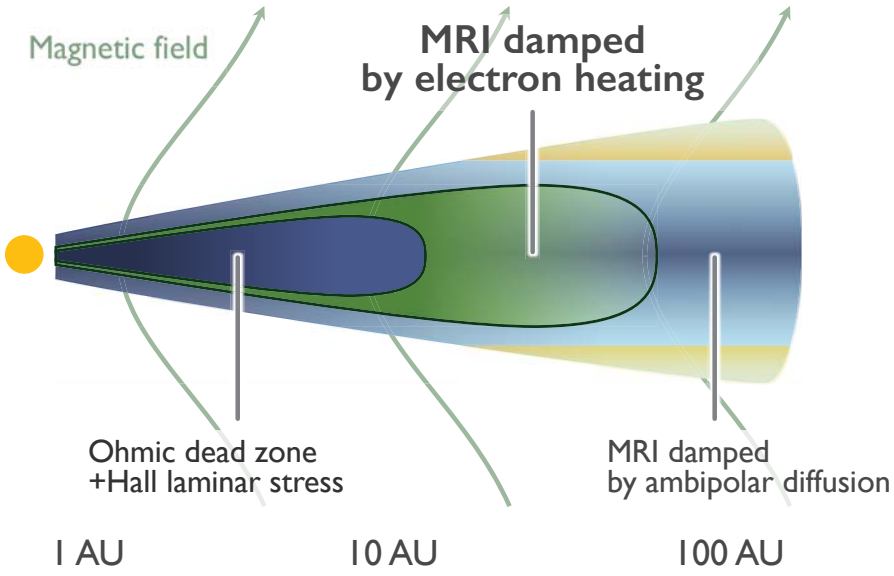

Figure 4.2 Schematic illustration of the expected turbulent structure of protoplanetary disks.

breakdown (Inutsuka & Sano, 2005; Muranushi et al., 2012). This may lead to chondrule formation by flash heating by the lightning current (Whipple, 1966; Desch & Cuzzi, 2000; Muranushi, 2010), which is important for understanding the solar system formation.

4.1.2 Expected Thermal Structure

Modeling of Thermal Structure

In Chapter 3, we have shown that the thermal structure of our model is largely different from the conventional model. To see this, we here model the temperature structure based on our simulation results. From our results, the following effects on the temperature structure are suggested.

- The accretion heating occurs on the disk surface with Joule dissipation. The heat accumulation around the midplane is unimportant. We neglect the heat accumulation of the accretion heating, in which the temperature profile is given by Equation

(1.9),

- Disk accretion occurs by the magnetic stress of the internal stress and wind stress. Disk wind flows out the energy from the surface by the magnetic stress. A part of the energy generated by the internal stress is used for heating. In order to express how much the energy is used for heating, we introduce a parameter $f_{\rm heat}$, the ratio of the heating to the accretion energy, and assume to be 0.2 from the typical value of the simulations for the $B_z > 0$ case (see Table 3.2).

- In the inner region, the viscous heating can increase the sufficient temperature for thermal ionization which requires gas to be $\gtrsim$ 800 K (Desch & Turner, 2015). In this *thermally-ionized region*, once MRI turbulence develops, the turbulence in the thermally ionized region would be sustained by itself. We ignore the above two effects and give the temperature by the viscous heating when the temperature due to viscous heating exceeds 800 K.

Therefore, the radial temperature profile T is given by

$$T = (T_{\rm acc}^4 + T_{\rm irr}^4)^{1/4}, \tag{4.1}$$

where $T_{\rm irr}$ is given by Equation (1.7),

$$T_{\rm acc} = \begin{cases} 57\left(\frac{f_{\rm heat}}{0.2}\right)^{1/4}\left(\frac{\dot{M}}{10^{-8}M_\odot/\,{\rm yr}}\right)^{1/4}\left(\frac{M}{M_\odot}\right)^{1/4}\left(\frac{r}{1\,{\rm AU}}\right)^{-3/4}\,{\rm K} & (T_{\rm vis} < 800K) \\ 326\left(\frac{f_{\rm heat}}{1}\right)^{1/4}\left(\frac{\dot{M}}{10^{-8}M_\odot/\,{\rm yr}}\right)^{2/5}\left(\frac{M}{M_\odot}\right)^{3/10}\left(\frac{\kappa}{5\,{\rm g\,cm^{-2}}}\right)^{1/5}\left(\frac{\alpha}{10^{-2}}\right)^{-1/5}\left(\frac{r}{1\,{\rm AU}}\right)^{-9/10}\,{\rm K} & (T_{\rm vis} \geq 800K) \end{cases} \tag{4}$$

and $T_{\rm vis}$ is given by the lower case of Equation (4.2).

Figure 4.3 shows the temperature distribution given by Equation (4.1). In the calculation, we use a steady state accretion disk orbiting around a solar-like star (solar mass and luminosity) with the accretion rate of $10^{-7}M_\odot/\,{\rm yr}$, α of 0.01, and the 0.1 μm-sized dust

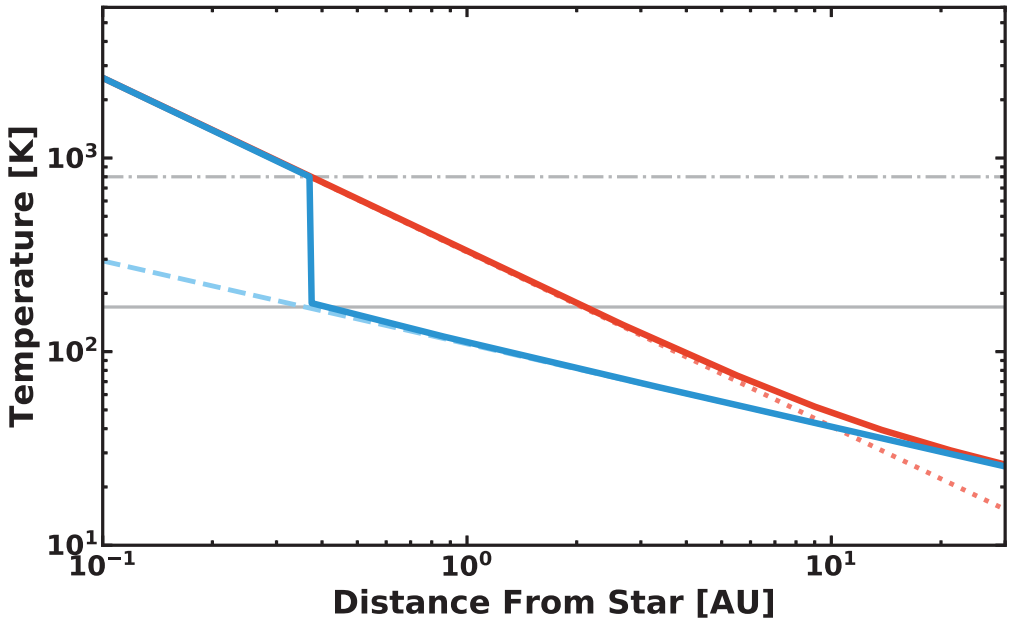

Figure 4.3 Radial temperature profile using Equation (4.1) (blue) and the conventional model (red; Equations 1.10 and 1.7). The blue dashed line and red dotted line show the temperature determined only by stellar irradiation and viscous heating, respectively. The horizontal gray solid and dash-dotted lines are equivalent to temperatures where water sublimates (T = 170 K) and where thermal ionization sets in (T = 800 K), respectively.

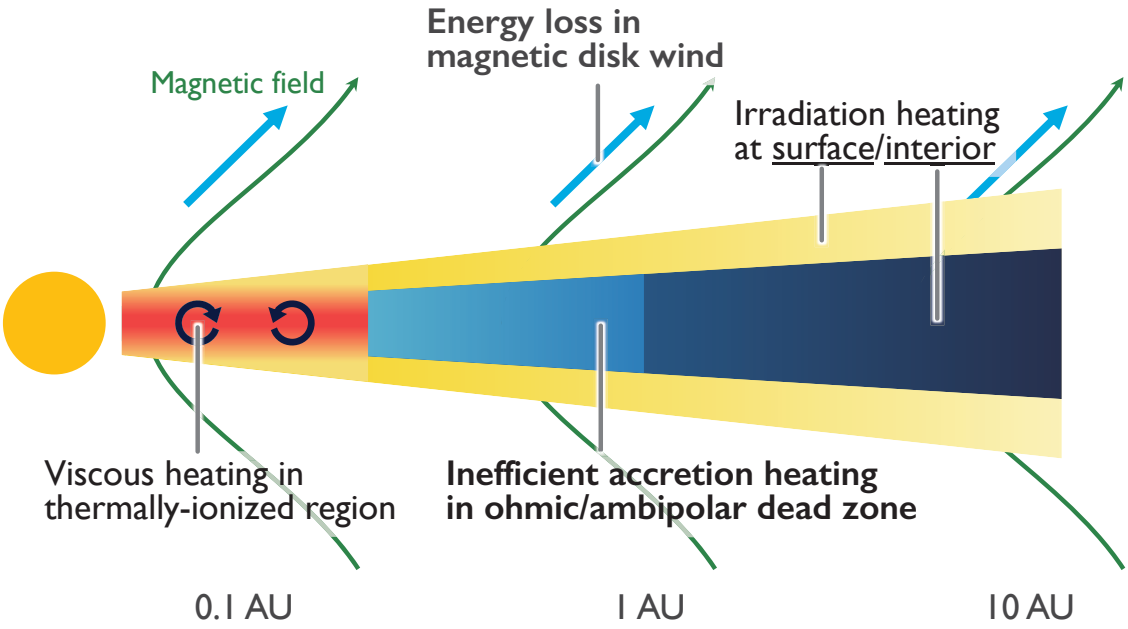

Figure 4.4 Schematic illustration of expected thermal structure of protoplanetary disks.

to gas ratio of 0.01. We take α to be 0.01 by considering that the disk accretion will be determined by the wind stress, and that the typical range of equivalent α value for the $B_z > 0$ case is $\sim$ 0.003–0.3 (see Table 3.2). For the conventional model, viscous heating is effective within 10 AU, which makes the steep radial temperature gradient of -9/10 (see Equation (1.10)). Beyond r = 10 AU, the temperature is determined by the stellar irradiation. For our model, the stellar irradiation determines the temperature beyond 0.4 AU Also, at 0.3 AU, the temperature jumps because of the self-sustaining MRI turbulence in the thermally ionized region.

We summarize the expected thermal structure with an illustration in Figure 4.4. In the model, the temperature around $r \sim 0.1$ –10 is updated from the conventional model.

Disk Structure around Thermally-Ionized Region

We here simply discuss a realistic gap structure at a location where thermal ionization sets in. We have assumed that MRI turbulence is sustained by thermal ionization once the temperature due to viscous heating exceeds the typical temperature for thermal ionization. However, if turbulence triggering the thermal ionization is absent, MHD at the region is dominated by non-ideal MHD effects. Thus, in the region where the viscous heating can maintain the thermal ionization, the thermal structure has two stable phases, which depend on the thermal history. For our assumption, supposing that the initially hot disk changes into cooler disk, we have chosen the hotter phase sustained by viscous heating.

If the outer edge of the thermally-ionized region is constantly cooled, the region shrinks with time. Conversely, the hot inner region may also activate MRI in the colder region. Thus, to understand the static structure, radial energy transport is essential.

Latter & Balbus (2012) calculated a quasi-static state of the gas structure by solving radial turbulence transport. They showed in the static state the gap lies at 65 percent of

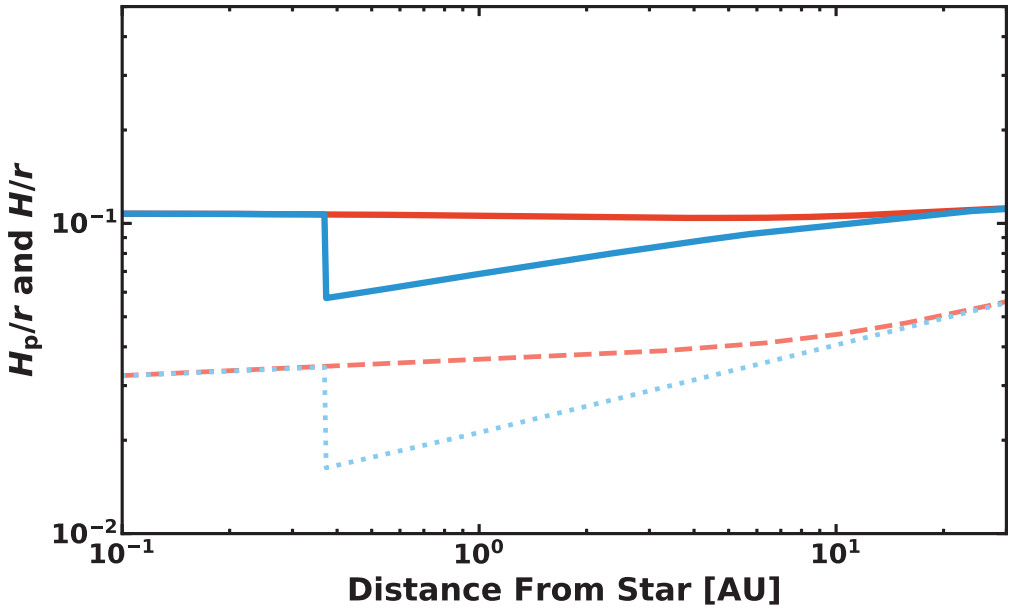

Figure 4.5 Ratio of the height H_p of the disk surface to the radius r as a function of r, for our model (blue) and conventional model (red). Lower lines show H/r for reference. The light from the star has a constant z/r. In this case, a shadow will forms from 0.4 AU to ~10 AU.

a critical radius at which the viscous heating marginally sustains the temperature larger than the thermal ionization temperature. For example, in the case of Figure 4.3, the gap shown at 0.4 AU will move to 0.26 AU because of the turbulence transport. The lack of energy is transported by turbulent diffusion and thereby increases the temperature to some extent.

Radial energy transport by radiation is also important to determine a realistic structure. The effect will be explained by the analogy of the turbulence transport, as both transport energy outward.

Shadow due to Innermost Region

Finally, to see if the inner thermally-ionized region cast a shadow on the outer region, we calculate the height H_p where the vertically-integrated optical depth is unity in Figure

4.5. Although the height is not accurately same as the surface absorbing light from the star, $H_{\rm p}$ agrees well with the absorbing surface when the surface is determined by local absorption of light. Since a light path from the central star has a constant z/r, Figure 4.5 shows that the star does not illuminate the region from the thermal gap to ~10 AU. The shadow reduces the temperature determined by irradiation, and thereby the disk will become colder than expected.

4.2 Time Evolution of Background Magnetic Fields

We here discuss the origin and time evolution of background magnetic fields. The background-magnetic-field strength affects the magnetic turbulent strength (see Figure 2.12). In addition, the direction of the magnetic fields determines the behavior of Hall effect (see Figure 3.4). Therefore, understanding of the evolution of disk magnetic fields is essential to understand the role of the magnetic field in planet formation.

The disk magnetic fields are originated from the molecular clouds. The magnetic fields in the clouds comove with the cloud gas because the cloud density is enough small to be ionized (e.g., Stahler & Palla, 2005). When molecular clouds collapse and form star and disk, magnetic fields comoving with the gas are dragged toward the center.

The magnetic field taken into the disk concentrates inward due to drag by the disk accretion or diffuses outward due to magnetic diffusion (Lubow et al., 1994; Okuzumi et al., 2014; Guilet & Ogilvie, 2014; Takeuchi & Okuzumi, 2014). This process largely depends on the accretion and magnetic-diffusivity structures. When the timescale of inward advection of the magnetic flux is faster than the diffusion timescale and disk lifetime, the field quickly goes a steady state described in Okuzumi et al. (2014) (Takeuchi & Okuzumi, 2014). When the diffusion timescale dominates over the other timescales, the magnetic flux diffuses outward.

Finally, we discuss polarity of background magnetic fields, which is the alignment of the magnetic field in the poloidal plane. The polarity of the background field conserves during the disk evolution since the field must connect external magnetic fields, though local magnetic fields may vary (e.g., due to magnetic turbulence).

The behavior of Hall effect, which is amplification or depletion of magnetic fields, should be basically consistent for a protoplanetary disk. This discussion provides a constraint that the Hall effect only amplifies or decays of magnetic fields through a planetary formation. Moreover, because the magnetic fields in the clouds scale do not correlate with the rotation axes of the clouds (Hull et al., 2014), the polarity of the disk magnetic field is determined randomly. This suggests that planetary systems may be divided into two groups half-and-half: amplified field system and damped field system. The role of Hall effect on planet formation should be studied further for a planet formation scenario consistent with the polarity of the background magnetic field.

4.3 Implication for Planetesimal Formation in Electron-Heating Zones

We here discuss the dust growth in electron-heating zones. In the electron-heating zone, the turbulence stress is reduced by two orders of the magnitude. In such weak turbulent disks, the dust sedimentation occurs more effectively.

The dust scale height for large grains is evaluated by $\sim H(\alpha/\mathrm{St})^{1/2}$ (Dubrulle et al., 1995), where St is Stokes number. At the outer region of the disk ($r \sim 30$ AU), the cm-sized dust grains ($\mathrm{St} \sim 1$) form a dust layer, where the density is 10 times higher than that in the fully developed MRI turbulence ($\alpha \sim 10^{-2}$). For $\alpha \approx 10^{-4}$, the midplane dust density to the gas density can be around unity. The local dust-to-gas ratio of unity is a crite-

rion for streaming instability which creating the dust clump and planetesimals (Youdin & Goodman, 2005).

In addition, a self-gravitational instability with radial perturbation is known as a secular gravitational instability (Youdin, 2011; Takahashi & Inutsuka, 2014, 2016). This instability gradually grows and enhances ring-like dust perturbations. The secular gravitational instability is expected to eventually produce planetesimals from the rings. The secular gravitational instability also requires weakly turbulent or laminar disks ($\alpha \lesssim 10^{-4}$) with high dust-to-gas mass ratio ($f_{\rm dg} \gtrsim 0.1$). Thus, the electron-heating zone might be the feasible region for creating planetesimals.

We have to note that the magnetic turbulence strength sensitively depends on the total dust surface area per unit volume, which determines how much dust grains absorb electrons. The dust sedimentation depletes the dust density above and below the midplane, and then MRI turbulence may revive. This process is expected to settle on an equilibrium state where the dust stirring by the sedimentation-driven MRI turbulence balances with dust sedimentation. Coevolution of dust dynamics and magnetic turbulence with electron heating is necessary to understand the steady state.

4.4 Implication for Snowline Problem

Our findings are that accretion heating is ineffective than the conventional model. This affects the evolution of the snow line, which in turn affects the rocky planet formation. In order to sustain the low water content, the formation time probably constrained from the snow line evolution. Especially in the case of the Earth, the water content is well studied and constrained. We see the snow line evolution expected from our simulations and discuss how much it impacts the Earth formation.

4.4.1 Introduction

The Earth is characterized by its low water content. The mass of the Earth's ocean is only 0.023 wt%. Even if we consider the water in the core, the water content is 1 wt% at most (Nomura et al., 2014). On the other hand, the icy dust in the outer solar system has large water contents of $\sim$ 50 wt% (Lodders, 2003). If such water-rich dust accretes onto the protoplanets of rocky planets, the planet would hold a large amount of water. After the water is taken into the protoplanet, the water hardly escapes from Earth-like planets even by stellar irradiation (Machida & Abe, 2010) or giant impacts (Genda & Abe, 2005). Therefore, it is surprising that the Earth's water is suppressed into an exquisite amount that makes the ocean and allows the presence of the land.

For the rocky planet formation, two important constraints come from the inward migration of the snow line. In the early phase, the temperature decreases with time, as the accretion rate decreases (Oka et al., 2011). The snow line moves inward and comes inside 1 AU eventually. In order for the protoplanets to form from the rocky dust, the protoplanet should form until the snow line lies outside 1 AU. Also, for the protoplanets to sustain to be dry, the accretion of the icy dust should be avoided.

One might think that because the snow line lies at 2.7 AU after disk dissipation, the Earth would form at the late stage. However, at the late stage ($\dot{M} \lesssim 10^{-10} \mathrm{M}_\odot/\mathrm{yr}$), the dust surface density at 1 AU is much smaller than the Earth mass. Also, dry planets need to form from water-depleted protoplanets, and so the Earth formation after the disk dissipation is not feasible.

We have shown the accretion heating is much less efficient than the conventional model in Chapter 3, and model the temperature profile in Section 4.1.2. Hereafter, we discuss how our results affect the evolution of snow line, and mention the plausible way for the rocky planet formation.

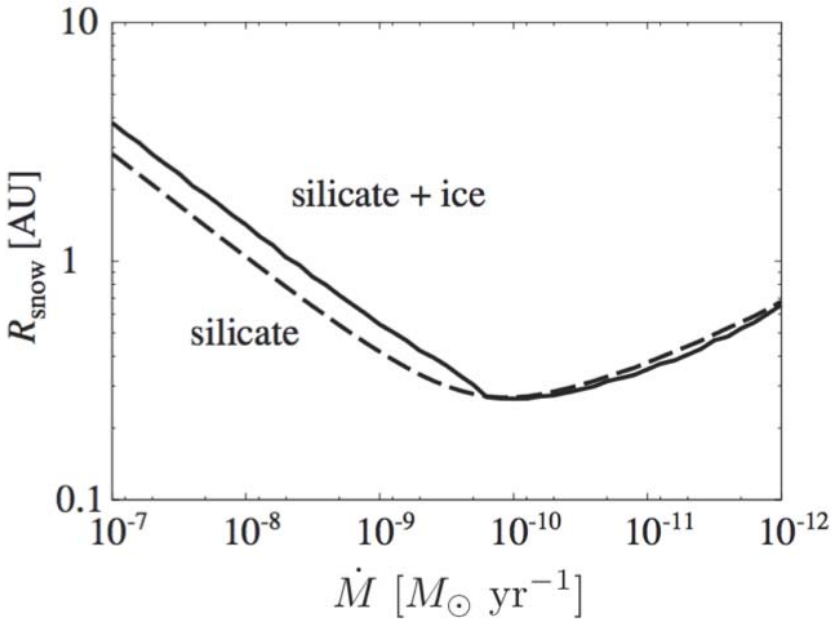

Figure 4.6 Position of the snow line as a function of the mass accretion rate with opacities for silicate dust (dashed line) and silicate + ice dust(solid line). This Figure is from Oka et al. (2011).

4.4.2 Evolution of Snowline

The snow line evolves with the temperature profile. In the early stages of the disk evolution, the accretion heating has been considered to be important for determining the temperature. Figure 4.6 shows the evolution of the snow line with the accretion rate. When the accretion rate is high (early phase), the temperature of the inner region is determined by the accretion heating ($\dot{M} \gtrsim 10^{-9} M_\odot$/yr). As the accretion rate decreases, the disk temperature decreases and then the snow line moves inward. When the accretion heating is sufficiently weak, the irradiation heating determines the position of the snow line ($\dot{M} \lesssim 10^{-9} M_\odot$/yr). As the accretion rate decreases and the disk becomes optically thin, the stellar irradiation becomes to illuminate the midplane, and thereby the snow line moves outward. The inward migration of the snow line means that location of r =1 AU must be outside the snow line.

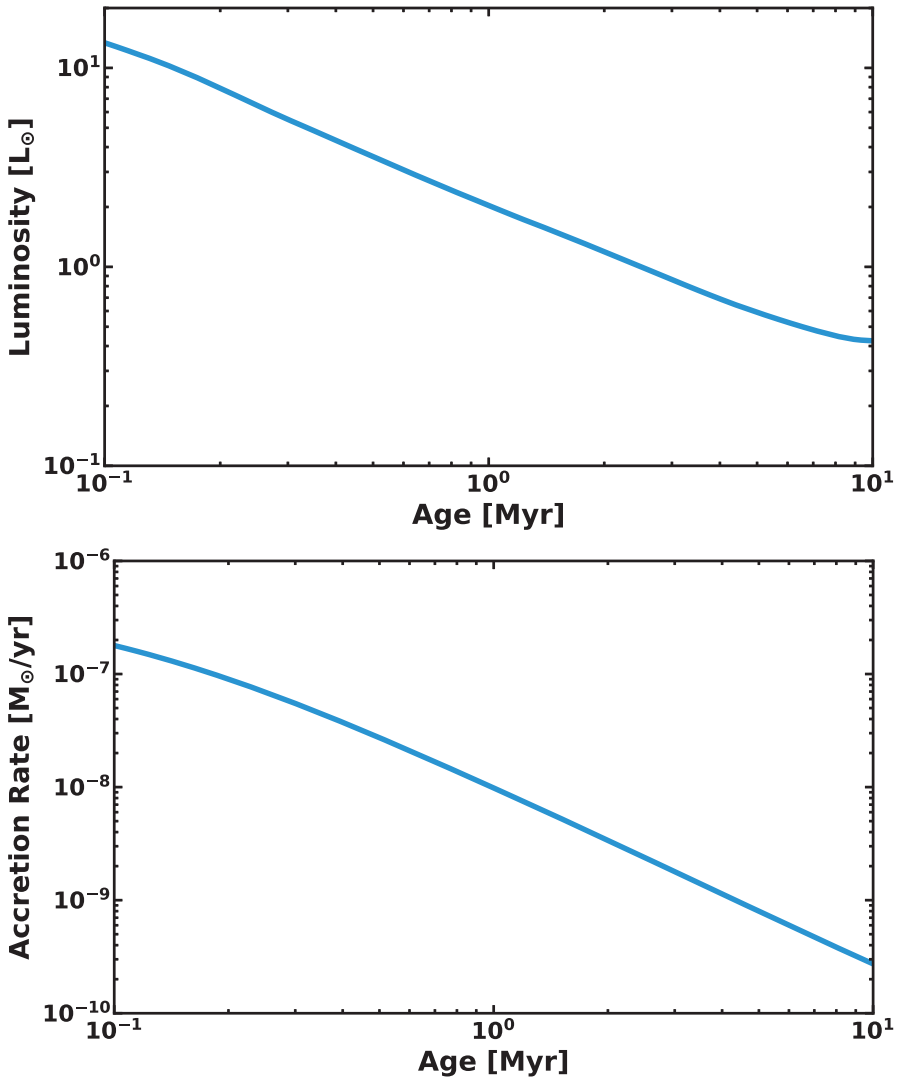

Figure 4.7 Stellar luminosity (upper panel) and the mass accretion rate (lower panel) used in our calculation, which are based on D'Antona & Mazzitelli (1994) and Hartmann et al. (1998), respectively.

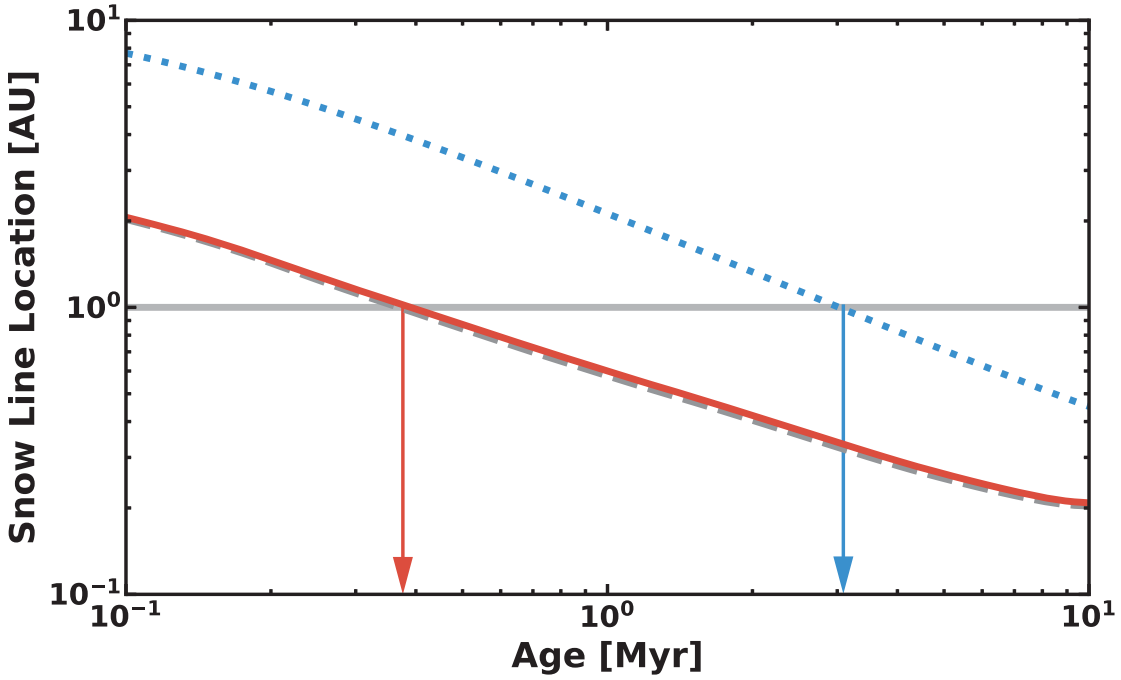

Figure 4.8 Location of the snow line as a function of the mass accretion rate using our temperature profile (red; Equation (4.1)) and conventional model (blue; Equation (1.10)). The arrows indicate the star age when the snow lines pass 1 AU for each model.

To understand the time evolution of the snow line in our model, we compute it by using the temperature model of Equation (4.1). We give the time evolutions of the mass accretion rate and stellar luminosity, as shown in Figure 4.7. The accretion rate is calculated with an analytic model described in Hartmann et al. (1998), and the luminosity evolution is given from a model of D'Antona & Mazzitelli (1994) used in Turner et al. (2012). Figure 4.8 shows the position of the snow line as a function of the time from the star formation. For the conventional model, the snow line passes 1 AU when age $t = 3$ Myr. In contrast, our model shows the passage time at 1 AU is when $t = 0.4$ Myr. This result suggests that the proto-Earth should form in the early phase of disk evolutionary stage. Furthermore, interestingly, our temperature model for $T < 800$ K does not depend on opacity which has huge uncertainty. If this model is true, we can predict the temperature profile and the resulting snow line robustly.

Note that this location of snow line comes from the irradiation. If the innermost region casts a shadow around 1 AU, the snow line pass 1 AU much earlier. In the case, the other heating mechanism is feasible to determine the snow line location.

4.4.3 Other Effects on Snowline

There are some other effects contribute to increasing disk temperature. We here discuss the possibility that other effects affect the position of the snow line.

Hydrodynamic Turbulence

Hydrodynamic instabilities may develop and cause the turbulence even though MRI turbulence is suppressed due to nonideal MHD effects. If the hydrodynamic turbulence converts part of accretion energy into heat in the disk interior, the heat might increases the disk temperature by the heat accumulation. For instance, in Figure 4.9, we add turbulent viscous heating to the accretion heating for fiducial calculation in Chapter 3. In this case, the turbulence with $\alpha \gtrsim 3 \times 10^{-3}$ contribute to increasing the midplane temperature, and thereby the snow line lies at 1 AU. Thus, the growth of hydrodynamic instabilities and the turbulence strength are important for the hydrodynamic turbulence to increase the disk temperature.

Vertical convective instability known as convection occurs when the vertical entropy gradient is positive. The hydrodynamic simulations show that the instability has a potential to generate the turbulence of $\alpha \sim 10^{-2}$ (Cabot, 1996; Klahr et al., 1999; Klahr & Bodenheimer, 2003; Käpylä et al., 2010). However, in order for this instability to grow, the vertical temperature gradient needs to be negative, as in the disk heated by the viscous heating. For our temperature model, the temperature around the midplane is isothermal, and therefore the vertical convective instability is unlikely to occur.

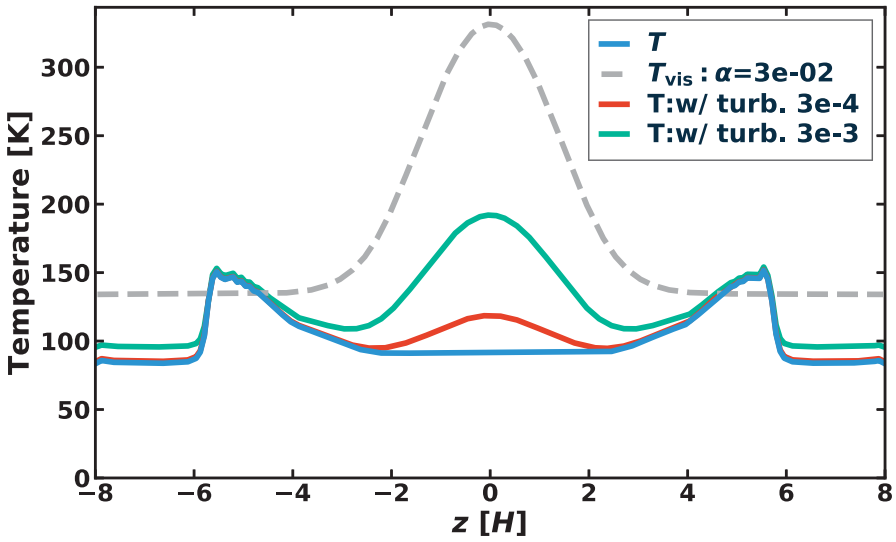

Figure 4.9 Same as Figure 3.3, but including homogeneous turbulence of $\alpha = 3 \times 10^{-3}$ (green) and 3×10^{-4} (red).

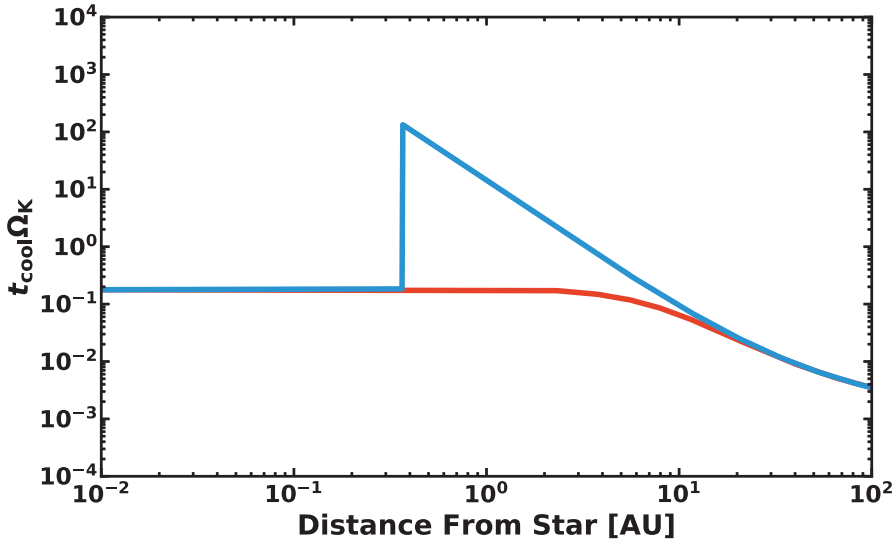

Figure 4.10 Cooling timescale $t_{\rm cool}$ at the midplane normalized by the dynamical timescale Ω^{-1} at $t = 1$ Myr, for our model (blue) and the conventional model (red). The calculation is done by Equation (107) in Lyra & Umurhan (2018). Following Lyra & Umurhan (2018), the length scale of interest is 0.1 H. For our model, due to low temperature, the radiative energy flux for cooling is delayed compared to the conventional model.

Vertical shear instability occurs even when the vertical convective instability does not grow (Nelson et al., 2013; Lin & Youdin, 2015). The growth of this instability needs conditions that the azimuthal velocity has a negative vertical gradient and that the cooling timescale is much faster than dynamical timescale Ω^{-1} to prevent a stabilizing force. The turbulence strength seen in the simulations is around $\alpha = 10^{-4} - 10^{-3}$ (Nelson et al., 2013; Stoll & Kley, 2014; Manger & Klahr, 2018), and thus potentially heats the disk. However, as we see in Figure 4.10, the cooling timescale $t_{\rm cool}$ in the inner region of our model at t = 1 Myr is around 10–100 Ω^{-1} (calculated by using Equation (107) in Lyra & Umurhan (2018)), whereas the conventional model shows $t_{\rm cool} \approx 0.1\Omega^{-1}$. Thus, this instability is also unlikely to occur around the midplane in the early phase.

Finally, convective over-stability is caused by an epicyclic motion enhanced by radial buoyancy force (Klahr & Hubbard, 2014). The feasible cooling timescale is comparable to around Kepler time (Klahr & Hubbard, 2014). Hydrodynamic simulations suggest that the turbulence strength α is around 10^{-3} (Lyra, 2014). However, the criterion of this instability that radial entropy gradient is negative is not fulfilled for our model.

Note that these instabilities potentially grow at upper layers and drive the whole disk into a turbulent state as shown in numerical simulations (Nelson et al., 2013; Klahr & Hubbard, 2014). Also, note that once any turbulence changes the thermal structure, the turbulence can be sustained by its self-heating. Understanding practical criteria for heating around the midplane needs further studies.

FU Ori Bursts

A burst phenomenon of young stars called FU Ori bursts would also heat the disk further. However, because the duration of the burst events is very short ($\lesssim$ a few years; Audard et al., 2014), the heated gas will be quickly cooled. Therefore, it seems hard that the FU

Ori bursts maintain the snow line outside 1 AU.

Gravitational Instability

A gravitational instability occurs in such young disks. The growth of the gravitational instability is evaluated by a Toomre's Q parameter (Toomre, 1964). When $Q \lesssim 1$, the gravitational spiral waves are woken. The gravitational waves cause compressional and shock heating around the midplane (Hirose & Shi, 2017). When $\dot{M} \gtrsim 10^{-6}\mathrm{M}_{\odot}/\mathrm{yr}$, the Q value is less than unity even at 1 AU. Thus, at this stage, the snow line will be pushed outside 1 AU, even though the planet formation in such violent disks need to be studied.

Summary

The summary of this section is the following.

- The passage time of the snow line at 1 AU constrains until when the Earth must have formed. From our model, the snow line passes 1 AU at $t \approx 0.4$ Myr.
- Hydrodynamic turbulence might be a heating mechanism when accretion is driven by MHD winds. Inefficient accretion heating tends to stabilize hydrodynamic instabilities around the midplane in the inner regions. The turbulence generated from unstable regions might be important for heating the disk.
- The gravitational instability can heat disk when $\dot{M} \sim 10^{-6}$ ($t \ll 0.1$ Myr).

In the next section, assuming the snow line moves to inside 1 AU at $t \approx 0.4$ Myr, we discuss the plausible mechanisms for the formation of rocky planets.

4.4.4 Constraints for Earth Formation

Here we discuss how the water content of the earth is sustained to be low. Specifically, the lower limit of the water contents is the ocean mass (0.023 wt%). The upper limit is 1 wt% which comes from the density deficit of the Earth's outer core (Nomura et al., 2014).

In Situ Formation

First of all, it is doubtful that the proto-Earth complete the formation from the dust. The formation of rocky planetesimals has berried, as seen in Section 1.2.4. One of the plausible mechanism to create rocky planetesimals is a streaming instability (Johansen et al., 2009). This instability creates dust clumps where the rocky planetesimals form. According to the simulations of Yang et al. (2016), the growth timescale is about 10^3 years. This timescale satisfies the time constraints of $\lesssim 0.1$ Myr.

For the growth from planetesimals to a protoplanet, the growth timescale is around 0.1 Myr for the classical planet formation (Kokubo & Ida, 2000). This timescale is comparable to our time constraint, and so the timescale of the proto-Earth formation might be a problem.

Hereafter, assuming the proto-Earth complete its formation until the snow line crosses 1 AU, we discuss how much water is supplied to the proto-Earth. Even if the Earth can form earlier inside the snow line, there are still problems. First, after the proto-Earth passes the snow line, the water vapor to the proto-earth condenses into the proto-Earth. In addition, the accretion of icy dust at the place also increases the water content of the proto-Earth. We estimate how much water can be taken into the proto-Earth. The water surface density

can be written as

$$\Sigma_{\rm ice} = \Sigma f_{\rm H_2O} \ , \tag{4.3}$$

where Σ is the gas surface density, and $f_{\rm H_2O}$ is the water mass fraction to the gas. Mass $\Delta M_{\rm H_2O}$ of water supplied to a protoplanet with $M_{\rm p} = 0.1 M_\oplus$ is

$$\begin{aligned} \Delta M_{\rm H_2O} &= 2\pi r \Delta r \Sigma_{\rm ice} \\ &= 0.016 M_{\rm p} \left(\frac{r}{1\ {\rm AU}}\right)^2 \left(\frac{\Delta r}{r_{\rm H}}\right) \left(\frac{M_{\rm p}}{0.1 M_\oplus}\right)^{-2/3} \left(\frac{M_*}{M_\odot}\right)^{-1/3} \left(\frac{\Sigma}{100\ {\rm g\ cm^{-2}}}\right) \left(\frac{f_{\rm H_2O}}{0.005}\right) , \end{aligned} \tag{4.4}$$

where water within a with Δr accretes into the protoplanet, and $r_{\rm H} = r(M_p/M_*)^{1/3}$ is a Hill radius. Here, the water mass fraction $f_{\rm H_2O}$ takes into account water vapor and ice dust, which is typically 0.005. According to this, in the early phase of the disk evolution ($\dot{M} > 10^{-7} {\rm M}_\odot/{\rm yr}$), the gas surface density is larger than $\approx$ 1000 g cm^{-2} (see Equation (1.6)). Therefore, this process might provide a large amount of water to the proto-Earth.

However, water vapor is not condensed onto the proto-Earth if the accretion velocity is faster than the migration timescale of the snow line (Morbidelli et al., 2016). In that case, the water vapor inside the snow line does not pass the snow line outward and therefore is not condensed.

For the accretion of the icy dust, the dust abundance at the place is important. If we assume the solar composition, the typical dust abundance is 0.01 (Lodders, 2003). Thus, the dust abundance needs to be reduced by some mechanisms. For this point, by dust growing into pebbles, the ice in the inner region may accrete to the star. However, icy pebbles will drift from the outer region to the inner region, and thereby this enhances ice abundance.

Accretion of icy pebbles supplies a large amount of water to the proto-Earth (Sato et al.,

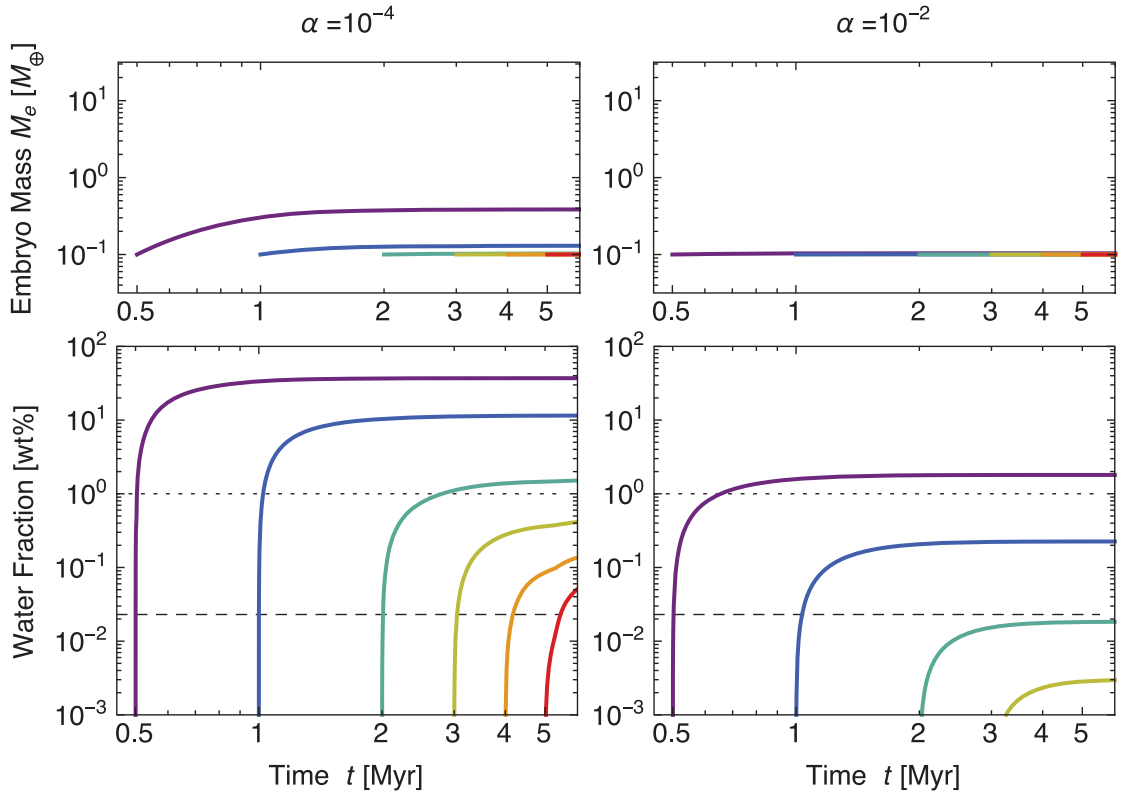

Figure 4.11 Time evolution of the mass M_e and water fraction $f_{\mathrm{H_2O}}$ of an embryo (protoplanet) placed at 1 AU with initial mass = $10^{-1} M_\oplus$, for the weak (left panels) and strong turbulence (right panels). The different lines show results for different time that the snow line passes 1 AU, t_{start} = 0.5, 1, 2, 3, 4, and 5 Myr (from left to right). This figure is from Sato et al. (2016).

2016). In the outer disk region, after the icy dust grows into pebbles, they radially drift toward the star and accrete onto the proto-Earth. Sato et al. (2016) investigated how much water is supplied to the proto-Earth by this mechanism. They concluded that the snow line needs to go inward across 1 AU after $t \approx 0.5$–2 Myr, so that the upper limit of the water content is fulfilled (Figure 4.11). In our temperature model, the snow line passes 1 AU at $t \approx 0.4$ Myr. Therefore, in our model, the evolution of the snow line produce the problem.

The growth timescale of pebbles is determined by the disk turbulence because turbulence determines the relative velocity. Thus, the final water fraction can be reduced if

the turbulence strength is strong. However, our turbulent model suggests that turbulence is suppressed. Therefore, we conclude that the ice pebble accretion must be avoided for sustaining the Earth to be dry.

One of the solutions for the icy pebble accretion is suggested by Morbidelli et al. (2016): if a gap is created by the Jupiter, the icy pebbles stops the radial drift at the outer edge of the gap. However, this scenario produces a constraint that the proto-Jupiter must form the gap earlier than the proto-Earth passes the snow line. For a protoplanet to create a gap, the core mass needs to be $\sim$10 $M_\oplus$. The pebble accretion model is expected to form Jupiter quickly (Lambrechts & Johansen, 2012; Kretke & Levison, 2014; Lambrechts & Johansen, 2014). Nevertheless, the current studies showed that the formation of 10 $M_\oplus$ core takes $\sim 10^6$ years (Lambrechts & Johansen, 2014; Levison et al., 2015). Thus, this scenario seems to require any mechanism to heat the inner regions further. Alternatively, there might be narrow parameter space fulfilling the both conditions.

Outward migration

So far, although we have assumed the in situ formation, if the Earth can form inside the snow line determined by the irradiation ($r \approx 0.4$AU), the time constraint of the protoplanet formation is unnecessary. In addition, the protoplanet can avoid obtaining ice while it is in the inner region.

A protoplanet gravitationally interacting with the disk has the potential to moves outward (Bitsch et al., 2013). The planets with sufficient mass move inward or outward in the disk because the planets gravitationally interact with the disk gas. The direction of the migration depends on the disk temperature structure (Bitsch et al., 2013, 2014a,b, 2015). When the temperature profile is described by a simple power law, the direction of the migration is inward (e.g., Tanaka et al., 2002). On the other hand, Bitsch et al. (2015) showed that

the steeper temperature gradient by the viscous heating results in the outward migration of the planets. In our model, since the temperature gradient is basically determined by stellar irradiation, this outward migration probably does not occur.

As another mechanism, the surface density structure having a positive gradient might cause outward migration (Ogihara et al., 2015). Such surface density can be created by the strong disk wind in the inner region (Suzuki et al., 2010). To understand if this mechanism works, the further studies on modeling the MHD disk wind are required.

4.5 Summary and Conclusion

In this thesis, we have investigated the role of magnetohydrodynamics on the turbulent and thermal structures of protoplanetary disks with numerical magnetohydrodynamic (MHD) simulations. Clarifying the influence of the magnetic field on the disk structure allows us to construct the planet formation theory in a realistic protoplanetary disk. Especially, turbulence strength is one of the most important parameters for the disk structure and planet formation. The turbulence drives the disk accretion and causes the dissipation of the accretion energy which increases the disk temperature. The turbulence is thought to be generated by a magnetorotational instability, but the MRI greatly depends on the ionization fraction. The ionization fraction determines the strength of nonideal magnetohydrodynamic effects, i.e., Ohmic diffusion, Hall effect, and ambipolar diffusion. The Ohmic and ambipolar diffusion diffuses magnetic fields, and the Hall effect amplifies or decays magnetic fields. Therefore, understanding the ionization fraction is necessary to understand turbulent strength correctly and for further discussion for the thermal structure.

In Chapter 2, we have investigated the turbulence strength of MRI by focusing on the effect of electron heating on the ionization fraction and MRI turbulence. The electron

heating is a phenomenon that strong electric fields accelerate and heat electrons. By the increase of the thermal velocity of electrons, electrons become to stick to dust grains frequently, and hence the electron abundance decreases. Therefore, the electron heating enhances non-ideal MHD effects. We have performed MHD simulations with Ohmic diffusion enhanced by the electron heating. We have first confirmed that the electron heating suppresses the MRI turbulence. Also, we have found a clear correlation between magnetic stress and its current density: the magnetic stress is proportional to the squared current density. We give an analytical description of the laminar state by using a solution of linear perturbation equations with resistivity. We also propose a formula that successfully predicts the accretion stress in the presence of the electron heating.

In Chapter 3, next, we have focused on the thermal structure of protoplanetary disks in the laminar disks. The disk temperature is quite important because it determines the position of the water snow line which constraints the rocky planet formation. In the inner disk region, the accretion heating is expected to determine the temperature profile. The conventional accretion heating model assumes the presence of turbulence and that its viscosity drives the disk accretion and accretion heating. However, the disk turbulence is suppressed by Ohmic diffusion. In addition, the ambipolar diffusion also suppresses MRI at disk surfaces, which leads to laminar disks. Furthermore, even in such laminar disks, the magnetic disk wind is expected to develop and flow out the accretion energy. In this Chapter, considering these recent works, we have investigated how efficiently the accretion heating heat the disk. Our simulations have confirmed that, around the midplane, Ohmic and ambipolar diffusion strongly suppress the magnetic turbulence releasing the heat. As a result, the heating takes place at several scale height of disk surface which leads to efficient radiative cooling. Furthermore, removal of accretion energy by disk wind reduce the total energy which used for heating. Therefore, we have concluded that the accretion heating is much inefficient than the conventional model. A previous study

Hirose & Turner (2011) have already shown that, in the Ohmic dead zone, the viscous heating become much inefficient than the conventional viscous heating model. This study confirms that their conclusion is valid even with the nonideal MHD effects other than Ohmic diffusion. In addition, we have newly shown the conclusion has a weak dependence on the disk parameters, which allow us to model the thermal structure of the disks. Furthermore, the disk wind is expected to remove significant accretion energy.

In Chapter 4, we have modeled the turbulent and thermal structures of the disk with basis on our results, and summarized the renewed picture of the disks. We also discus the evolution of the snow line using the temperature model given by our results. The inefficient accretion heating further suggests the necessity for the proto-Earth to complete its formation in the early phase of the disk evolution ($\lesssim$0.4 Myr). This work highlights necessity of further understanding other heating mechanisms (e.g., hydrodynamic turbulence) and/or formation scenario that Jupiter can form earlier, for the Earth to be a dry planet.

Acknowledgement

First, I would like to express my deepest gratitude to my great supervisor, Dr. Satoshi Okuzumi, for his constant encouragement and forbearing support. Discussions with him have always been constructive. I am really glad that I have learned a lot from him. Dr. Shu-Ichiro Inutsuka in the Nagoya University have strongly encouraged my research and injected his infinite energy into me. In addition, I deeply thank all of the referees, Dr. Shigeru Ida, Dr. Taishi Nakamoto, Dr. Hideko Nomura, Dr. Hideo Tsunakawa and Dr. Shigenobu Hirose for carefully reviewing and giving comments improving the thesis. In particular, Dr. Hirose in JAMSTEC (Japan Agency for Marine-Earth Science and Technology) kindly accepted an external referee. I would like to express my deep sense of gratitude for that. I also thank my reliable colleagues, Takahiro Ueda and Yuhito Shibaike. We have encouraged each other for the completion of our theses, which really helped me a lot.

References

Adachi, I., Hayashi, C., & Nakazawa, K. 1976, Progress of Theoretical Physics, 56, 1756

A'Hearn, M. F., Belton, M. J. S., Delamere, W. A., et al. 2011, Science, 332, 1396

ALMA Partnership, Brogan, C. L., Pérez, L. M., et al. 2015, ApJ, 808, L3

Andrews, S. M., Wilner, D. J., Espaillat, C., et al. 2011, ApJ, 732, 42

Audard, M., Ábrahám, P., Dunham, M. M., et al. 2014, Protostars and Planets VI, 387

Bai, X.-N. 2011, ApJ, 739, 50

—. 2013, ApJ, 772, 96

—. 2014, ApJ, 791, 137

—. 2015, ApJ, 798, 84

—. 2017, ApJ, 845, 75

Bai, X.-N., & Goodman, J. 2009, ApJ, 701, 737

Bai, X.-N., & Stone, J. M. 2010, ApJ, 722, 1437

—. 2011, ApJ, 736, 144

—. 2013, ApJ, 769, 76

—. 2017, ApJ, 836, 46

Bai, X.-N., Ye, J., Goodman, J., & Yuan, F. 2016, ApJ, 818, 152

Balbus, S. A., & Hawley, J. F. 1991, ApJ, 376, 214

—. 1998, Reviews of Modern Physics, 70, 1

Balbus, S. A., & Terquem, C. 2001, ApJ, 552, 235

Béthune, W., Lesur, G., & Ferreira, J. 2016, A&A, 589, A87

Birnstiel, T., Ormel, C. W., & Dullemond, C. P. 2011, A&A, 525, A11

Bitsch, B., Crida, A., Morbidelli, A., Kley, W., & Dobbs-Dixon, I. 2013, A&A, 549, A124

Bitsch, B., Johansen, A., Lambrechts, M., & Morbidelli, A. 2015, A&A, 575, A28

Bitsch, B., Morbidelli, A., Lega, E., & Crida, A. 2014a, A&A, 564, A135

Bitsch, B., Morbidelli, A., Lega, E., Kretke, K., & Crida, A. 2014b, A&A, 570, A75

Blandford, R. D., & Payne, D. G. 1982, MNRAS, 199, 883

Blum, J., & Wurm, G. 2000, Icarus, 143, 138

—. 2008, ARA&A, 46, 21

Cabot, W. 1996, ApJ, 465, 874

Calvet, N., Patino, A., Magris, G. C., & D'Alessio, P. 1991, ApJ, 380, 617

Carballido, A., Cuzzi, J. N., & Hogan, R. C. 2010, MNRAS, 405, 2339

Carballido, A., Stone, J. M., & Pringle, J. E. 2005, MNRAS, 358, 1055

Carrera, D., Johansen, A., & Davies, M. B. 2015, A&A, 579, A43

Charette, M. A., & Smith, W. H. 2010, Oceanography, 23, 112

Chatterjee, S., & Tan, J. C. 2014, ApJ, 780, 53

Chiang, E. I., & Goldreich, P. 1997, ApJ, 490, 368

Chokshi, A., Tielens, A. G. G. M., & Hollenbach, D. 1993, ApJ, 407, 806

Cieza, L. A., Casassus, S., Tobin, J., et al. 2016, Nature, 535, 258

D'Antona, F., & Mazzitelli, I. 1994, ApJS, 90, 467

Davis, S. S. 2005, ApJ, 620, 994

Desch, S. J. 2004, ApJ, 608, 509

Desch, S. J., & Cuzzi, J. N. 2000, Icarus, 143, 87

Desch, S. J., & Turner, N. J. 2015, ApJ, 811, 156

Dominik, C., & Tielens, A. G. G. M. 1997, ApJ, 480, 647

Dorn, C., Mosegaard, K., Grimm, S. L., & Alibert, Y. 2018, ArXiv e-prints, arXiv:1808.01803

Dressing, C. D., Charbonneau, D., Dumusque, X., et al. 2015, ApJ, 800, 135

Dubrulle, B., Morfill, G., & Sterzik, M. 1995, Icarus, 114, 237

Dzyurkevich, N., Turner, N. J., Henning, T., & Kley, W. 2013, The Astrophysical Journal, 765, 114

Elsasser, H., & Staude, H. J. 1978, A&A, 70, L3

Faure, J., Fromang, S., & Latter, H. 2014, A&A, 564, A22

Faure, J., Fromang, S., Latter, H., & Meheut, H. 2015, A&A, 573, A132

Flaherty, K. M., Hughes, A. M., Rosenfeld, K. A., et al. 2015, ApJ, 813, 99

Flaherty, K. M., Hughes, A. M., Rose, S. C., et al. 2017, ApJ, 843, 150

Flaig, M., Kley, W., & Kissmann, R. 2010, MNRAS, 409, 1297

Fleming, T., & Stone, J. M. 2003, ApJ, 585, 908

Fleming, T. P., Stone, J. M., & Hawley, J. F. 2000, ApJ, 530, 464

Flock, M., Dzyurkevich, N., Klahr, H., Turner, N. J., & Henning, T. 2011, ApJ, 735, 122

Flock, M., Fromang, S., Turner, N. J., & Benisty, M. 2017, ApJ, 835, 230

Fromang, S., & Nelson, R. P. 2006, A&A, 457, 343

—. 2009, A&A, 496, 597

Fromang, S., & Papaloizou, J. 2006, A&A, 452, 751

Fukagawa, M., Tamura, M., Itoh, Y., et al. 2006, ApJ, 636, L153

Gammie, C. F. 1996, ApJ, 457, 355

Garaud, P., & Lin, D. N. C. 2007, ApJ, 654, 606

Genda, H., & Abe, Y. 2005, Nature, 433, 842

Gillon, M., Triaud, A. H. M. J., Demory, B.-O., et al. 2017, Nature, 542, 456

Glassgold, A. E., Najita, J., & Igea, J. 1997, ApJ, 480, 344

Goldreich, P., & Lynden-Bell, D. 1965, MNRAS, 130, 97

Goldreich, P., & Ward, W. R. 1973, ApJ, 183, 1051

Grady, C. A., Muto, T., Hashimoto, J., et al. 2013, ApJ, 762, 48

Gressel, O., Turner, N. J., Nelson, R. P., & McNally, C. P. 2015, ApJ, 801, 84

Grimm, S. L., Demory, B.-O., Gillon, M., et al. 2018, A&A, 613, A68

Guilet, J., & Ogilvie, G. I. 2014, MNRAS, 441, 852

Guillot, T. 2010, A&A, 520, A27

Güttler, C., Blum, J., Zsom, A., Ormel, C. W., & Dullemond, C. P. 2010, A&A, 513, A56

Haisch, Jr., K. E., Lada, E. A., & Lada, C. J. 2001, ApJ, 553, L153

Hartmann, L., Calvet, N., Gullbring, E., & D'Alessio, P. 1998, ApJ, 495, 385

Hawley, J. F., Gammie, C. F., & Balbus, S. A. 1995, ApJ, 440, 742

Hayashi, C. 1981, Progress of Theoretical Physics Supplement, 70, 35

Hirose, S., Krolik, J. H., & Stone, J. M. 2006, ApJ, 640, 901

Hirose, S., & Shi, J.-M. 2017, MNRAS, 469, 561

Hirose, S., & Turner, N. J. 2011, ApJ, 732, L30

Hubeny, I. 1990, ApJ, 351, 632

Hull, C. L. H., Plambeck, R. L., Kwon, W., et al. 2014, ApJS, 213, 13

Inutsuka, S., & Sano, T. 2005, ApJ, 628, L155

Isella, A., Guidi, G., Testi, L., et al. 2016, Physical Review Letters, 117, 251101

Jin, L. 1996, ApJ, 457, 798

Johansen, A., & Youdin, A. 2007, ApJ, 662, 627

Johansen, A., Youdin, A., & Mac Low, M.-M. 2009, ApJ, 704, L75

Johnson, K. L. 1987, Contact Mechanics (Cambridge University Press), 464

Johnson, K. L., Kendall, K., & Roberts, A. D. 1971, Proceedings of the Royal Society of London Series A, 324, 301

Käpylä, P. J., Brandenburg, A., Korpi, M. J., Snellman, J. E., & Narayan, R. 2010, ApJ, 719, 67

Kataoka, A., Tanaka, H., Okuzumi, S., & Wada, K. 2013, A&A, 557, L4

Klahr, H., & Hubbard, A. 2014, ApJ, 788, 21

Klahr, H. H., & Bodenheimer, P. 2003, ApJ, 582, 869

Klahr, H. H., Henning, T., & Kley, W. 1999, ApJ, 514, 325

Kokubo, E., & Ida, S. 1996, Icarus, 123, 180

—. 1998, Icarus, 131, 171

—. 2000, Icarus, 143, 15

Kokubo, E., Ida, S., & Makino, J. 2000, Icarus, 148, 419

Kraus, S., Kreplin, A., Fukugawa, M., et al. 2017, ApJ, 848, L11

Kretke, K. A., & Levison, H. F. 2014, AJ, 148, 109

Kunz, M. W. 2008, MNRAS, 385, 1494

Kunz, M. W., & Balbus, S. A. 2004, MNRAS, 348, 355

Kunz, M. W., & Lesur, G. 2013, MNRAS, 434, 2295

Kusaka, T., Nakano, T., & Hayashi, C. 1970, Progress of Theoretical Physics, 44, 1580

Lambrechts, M., & Johansen, A. 2012, A&A, 544, A32

—. 2014, A&A, 572, A107

Latter, H. N., & Balbus, S. 2012, MNRAS, 424, 1977

Lesur, G., Kunz, M. W., & Fromang, S. 2014, A&A, 566, A56

Levison, H. F., Kretke, K. A., Walsh, K. J., & Bottke, W. F. 2015, Proceedings of the National Academy of Science, 112, 14180

Lin, D. N. C., & Papaloizou, J. 1986, ApJ, 309, 846

Lin, M.-K., & Youdin, A. N. 2015, ApJ, 811, 17

Lodders, K. 2003, ApJ, 591, 1220

Lubow, S. H., Papaloizou, J. C. B., & Pringle, J. E. 1994, MNRAS, 267, 235

Luhman, K. L., Allen, P. R., Espaillat, C., Hartmann, L., & Calvet, N. 2010, ApJS, 186, 111

Lynden-Bell, D., & Pringle, J. E. 1974, MNRAS, 168, 603

Lyra, W. 2014, ApJ, 789, 77

Lyra, W., & Umurhan, O. 2018, arXiv:1808.08681v1

Machida, R., & Abe, Y. 2010, ApJ, 716, 1252

Manger, N., & Klahr, H. 2018, MNRAS, 480, 2125

Masset, F. 2000, A&AS, 141, 165

Mayor, M., & Queloz, D. 1995, Nature, 378, 355

Mihalas, D. 1978, Stellar atmospheres /2nd edition/ (Oxford University Press)

Morbidelli, A., Bitsch, B., Crida, A., et al. 2016, Icarus, 267, 368

Mori, S., Bai, X.-N., & Okuzumi, S. 2019, The Astrophysical Journal, 872, 98

Mori, S., Muranushi, T., Okuzumi, S., & Inutsuka, S.-i. 2017, ApJ, 849, 86

Mori, S., & Okuzumi, S. 2016, ApJ, 817, 52

Muranushi, T. 2010, MNRAS, 401, 2641

Muranushi, T., & Inutsuka, S.-i. 2009, ApJ, 691, L24

Muranushi, T., Okuzumi, S., & Inutsuka, S. 2012, ApJ, 760, 56

Muto, T., Grady, C. A., Hashimoto, J., et al. 2012, ApJ, 748, L22

Nakagawa, Y., Sekiya, M., & Hayashi, C. 1986, Icarus, 67, 375

Nelson, R. P., Gressel, O., & Umurhan, O. M. 2013, MNRAS, 435, 2610

Noble, S. C., Krolik, J. H., & Hawley, J. F. 2010, ApJ, 711, 959

Nomura, R., Hirose, K., Uesugi, K., et al. 2014, Science, 343, 522

Ogihara, M., Kobayashi, H., Inutsuka, S.-i., & Suzuki, T. K. 2015, A&A, 579, A65

Ogihara, M., Kokubo, E., Suzuki, T. K., Morbidelli, A., & Crida, A. 2017, A&A, 608, A74

Ogilvie, G. I., & Lubow, S. H. 2002, MNRAS, 330, 950

Oka, A., Nakamoto, T., & Ida, S. 2011, ApJ, 738, 141

Okuzumi, S. 2009, ApJ, 698, 1122

Okuzumi, S., & Inutsuka, S.-i. 2015, ApJ, 800, 47

Okuzumi, S., Takeuchi, T., & Muto, T. 2014, ApJ, 785, 127

Okuzumi, S., Tanaka, H., Kobayashi, H., & Wada, K. 2012, ApJ, 752, 106

Ormel, C. W., & Okuzumi, S. 2013, ApJ, 771, 44

Pérez, L. M., Carpenter, J. M., Andrews, S. M., et al. 2016, Science, 353, 1519

Perez-Becker, D., & Chiang, E. 2011, ApJ, 735, 8

Pinte, C., Dent, W. R. F., Ménard, F., et al. 2016, ApJ, 816, 25

Rybicki, G. B., & Lightman, A. P. 1979, Radiative processes in astrophysics (Wiley)

Safronov, V. S. 1969, Evoliutsiia doplanetnogo oblaka. (Nauka)

—. 1972, Evolution of the protoplanetary cloud and formation of the earth and planets. (Keter Publishing House)

Sano, T., Inutsuka, S., Turner, N. J., & Stone, J. M. 2004, ApJ, 605, 321

Sano, T., & Miyama, S. M. 1999, ApJ, 515, 776

Sano, T., Miyama, S. M., Umebayashi, T., & Nakano, T. 2000, ApJ, 543, 486

Sano, T., & Stone, J. M. 2002a, ApJ, 570, 314

—. 2002b, ApJ, 577, 534

Sato, T., Okuzumi, S., & Ida, S. 2016, A&A, 589, A15

Shakura, N. I., & Sunyaev, R. A. 1973, A&A, 24, 337

Shu, F. H. 1977, ApJ, 214, 488

Simon, J. B., Hawley, J. F., & Beckwith, K. 2009, ApJ, 690, 974

Simon, J. B., Lesur, G., Kunz, M. W., & Armitage, P. J. 2015, MNRAS, 454, 1117

Spruit, H. C. 1996, ArXiv Astrophysics e-prints, astro-ph/9602022

Stahler, S. W., & Palla, F. 2005, The Formation of Stars, 865

Stoll, M. H. R., & Kley, W. 2014, A&A, 572, A77

Stone, J. M., & Gardiner, T. A. 2010, ApJS, 189, 142

Stone, J. M., Gardiner, T. A., Teuben, P., Hawley, J. F., & Simon, J. B. 2008, ApJS, 178, 137

Suzuki, T. K., & Inutsuka, S. 2009, ApJ, 691, L49

Suzuki, T. K., Muto, T., & Inutsuka, S. 2010, ApJ, 718, 1289

Takahashi, S. Z., & Inutsuka, S. 2014, ApJ, 794, 55

—. 2016, AJ, 152, 184

Takeuchi, T., & Okuzumi, S. 2014, ApJ, 797, 132

Tanaka, H., Takeuchi, T., & Ward, W. R. 2002, ApJ, 565, 1257

Tominaga, R. K., Inutsuka, S., & Takahashi, S. Z. 2017, submitted to ApJ

Toomre, A. 1964, ApJ, 139, 1217

Tsukamoto, Y., Iwasaki, K., Okuzumi, S., Machida, M. N., & Inutsuka, S. 2015, ApJ, 810, L26

Turner, N. J., Carballido, A., & Sano, T. 2010, ApJ, 708, 188

Turner, N. J., Choukroun, M., Castillo-Rogez, J., & Bryden, G. 2012, ApJ, 748, 92

Umebayashi, T. 1983, Progress of Theoretical Physics, 69, 480

Umebayashi, T., & Nakano, T. 1981, PASJ, 33, 617

van der Marel, N., van Dishoeck, E. F., Bruderer, S., et al. 2013, Science, 340, 1199

Velikhov, E. P. 1959, JETP

Wada, K., Tanaka, H., Okuzumi, S., et al. 2013, A&A, 559, A62

Wada, K., Tanaka, H., Suyama, T., Kimura, H., & Yamamoto, T. 2007, ApJ, 661, 320

—. 2008, ApJ, 677, 1296

—. 2009, ApJ, 702, 1490

—. 2011, ApJ, 737, 36

Wardle, M. 1999, MNRAS, 307, 849

—. 2007, Ap&SS, 311, 35

Wardle, M., & Salmeron, R. 2012, MNRAS, 422, 2737

Weidenschilling, S. J. 1977, MNRAS, 180, 57

Weidenschilling, S. J., & Cuzzi, J. N. 1993, in Protostars and Planets III, ed. E. H. Levy & J. I. Lunine, 1031–1060

Whipple, F. L. 1966, Science, 153, 54

Xu, R., & Bai, X.-N. 2016, ApJ, 819, 68

Yang, C.-C., Johansen, A., & Carrera, D. 2016, ArXiv e-prints, arXiv:1611.07014

Youdin, A. N. 2011, ApJ, 731, 99

Youdin, A. N., & Goodman, J. 2005, ApJ, 620, 459

Zhu, Z., Stone, J. M., & Bai, X.-N. 2015, ApJ, 801, 81

Zsom, A., Ormel, C. W., Güttler, C., Blum, J., & Dullemond, C. P. 2010, A&A, 513, A57